UNIVERSIDADE DE BRASÍLIA - UNB
INSTITUTO DE GEOCIÊNCIAS – IG
PROGRAMA DE PÓS-GRADUAÇÃO EM GEOLOGIA

A lateritização no terreno granito-greenstone Almas-Dianópolis, SE do Tocantins: uma abordagem gamaespectrométrica e espectroradiométrica

Sanclever Freire Peixoto

Tese de Doutorado nº 183

Área de concentração: Geologia Regional

Brasília, 03 de dezembro de 2021.

UNIVERSIDADE DE BRASÍLIA - UNB
INSTITUTO DE GEOCIÊNCIAS – IG
PROGRAMA DE PÓS-GRADUAÇÃO EM GEOLOGIA

A lateritização no terreno granito-greenstone Almas-Dianópolis, SE do Tocantins: uma abordagem gamaespectrométrica e espectroradiométrica

Discente

Sanclever Freire Peixoto

Banca Examinadora:

Dra. Adriana Maria Coimbra Horbe (orientadora/IG-UnB)

Dr. Alvaro Penteado Crósta (IG-UNICAMP)

Dr. Vinicius Hector Abud Louro (IGc-USP)

Dra. Roberta Mary Vidotti (IG-UnB)

ÀREA DE CONCENTRAÇÃO

Geologia Regional

Brasília, 03 de dezembro de 2021.

Ficha catalográfica elaborada automaticamente,
com os dados fornecidos pelo(a) autor(a)

PP3791

Peixoto, Sanclever Freire
A lateritização no terreno granito-greenstone Almas Dianópolis, SE do Tocantins: uma abordagem gamaespectrométrica e espectroradiométrica / Sanclever Freire Peixoto; orientador Adriana Maria Coimbra Horbe. -- Brasília, 2021.
105 p.

Tese (Doutorado - Doutorado em Geologia) -- Universidade de Brasília, 2021.

1. Crosta laterítica. 2. Operadores lógicos Booleano e difuso. 3. Regressão linear multivariada. 4. Razões de bandas. 5. Análise de componentes principais. I. Horbe, Adriana Maria Coimbra, orient. II. Título.

UNIVERSIDADE DE BRASÍLIA - UNB
INSTITUTO DE GEOCIÊNCIAS – IG
PROGRAMA DE PÓS-GRADUAÇÃO EM GEOLOGIA

Sanclever Freire Peixoto

Tese apresentada ao Programa de Pós-Graduação em Geologia do Instituto de Geociências da Universidade de Brasília, como requisito parcial para a obtenção do título de Doutor em Geologia, área de concentração Geologia Regional

Banca Examinadora:

_____

Dra. Adriana Maria Coimbra Horbe (orientadora/IG-UnB)

_____

Dr. Alvaro Penteado Crósta (IG-UNICAMP)

_____

Dr. Vinicius Hector Abud Louro (IGc-USP)

_____

Dra. Roberta Mary Vidotti (IG-UnB)

Brasília, 03 de dezembro de 2021.

Em lugar de um prefácio

Uma vez cheguei a refletir sobre as diferentes ocupações a que os homens se entregam nesta vida e fiz a tentativa de selecionar as melhores delas. Mas não é necessário contar aqui a que pensamentos cheguei a respeito: basta dizer que, pela parte que me toca, nada me pareceu melhor do que me manter estritamente em meu propósito, ou seja, empregar todo o tempo da vida para desenvolver minha razão e seguir, da maneira que me havia proposto, na pista da verdade.

Pois os frutos, que já havia saboreado seguindo esses caminhos, eram de tal ordem que, em minha opinião, nada mais agradável, mais inocente, se pode encontrar nesta vida: além disso, desde que recorri a essa forma de observar, cada dia me levou a descobrir algo de novo, que tinha sempre uma certa importância e que de modo algum era do conhecimento geral. Finalmente, minha alma ficou tão repleta de alegria que todas as outras coisas já nada podiam lhe fazer.

Extraído de texto latino de Descartes

DEDICATÓRIA

Dedico esta tese à minha mãe Sandra Freire Peixoto e meu pai Manuel Peixoto de Araújo por todo amor, incentivo, proteção e muito sacrifício para que eu e meus irmãos estudássemos.

Agradecimentos

Agradeço especialmente a minha orientadora Profª Adriana Horbe por sua paciência, generosidade e amizade.

Aos filhotes Débora, Sandy e Leônidas e neto Bernardo por todo amor e compreensão de minha ausência necessária para elaborar este trabalho. À minha querida irmã Sirrame por todo carinho, ajuda e incentivo diário, e ao meu irmão Sandro pela amizade. Amo vocês.

O presente trabalho foi realizado com o apoio da Coordenação de Aperfeiçoamento de Pessoal de Nível Superior – Brasil (CAPES) – Código de Financiamento 001.

Eu expresso o meu grato agradecimento pela gentileza e amizade demonstrada pelos colegas do laboratório de difratometria de raios-x da Universidade de Brasília: Adriana Horbe, Márcio Albuquerque, Rodrigo Tokuta, Caroline Freitas, Gustavo Rosas, Gabriel Domingues, Rafael Brasil e Bárbara Costa. Ao Darby Lima, Francisco Campos (UFMT), Túlio Soares e Endel Sousa pela ajuda com os softwares. Aos colegas do TF 2016 que mapearam a área debaixo de muito sol e ao prof. Eloi Campos que gentilmente cedeu os dados. Ao Rafael Felício que me deu suporte em informática nos momentos desesperadores.

À Universidade de Brasília pelo suporte físico e técnico. Aos professores do Programa de Pós-Graduação em Geologia pela oportunidade e conhecimento transmitido.

À banca examinadora pela honra em tê-los como avaliadores, e por suas críticas e sugestões.

À minha amiga e irmã Maíra Paiva pela amizade preciosíssima e constante incentivo. Às tias Marion Freire e Waldeliz Peixoto (in memorian), professoras e fontes de admiração. Ao meu tio Valmir Pereira (in memorian) pela amizade eterna.

Meus agradecimentos especiais ao amigo Jorge Kleber Neiva Brito pelo esforço no deferimento de minha licença do NATURATINS para aperfeiçoamento profissional. Agradecimento que se estende ao então pres. Hebert Barros e governador Marcelo Miranda.

Ao Ibrahim Oliveira e sua esposa Bruna pela amizade e todo suporte no Tocantins enquanto estive em Brasília. Ao Nonato, Larissa e Cristina que sempre me acolheram muito bem na colina/UnB. Ao Luciano Freire, Luana e Raíssa por me receberem em Brasília. Aos amigos Max Domingos, D. Amélia Martins e Ricardo Lopes pelo incentivo. Ao Diones e Sóstenes pela acomodação durante trabalho de campo em Almas e a todos que de alguma forma contribuíram para esta tese.

À Deus de Spinoza por proteger a mim e minha família.

Resumo

No Brasil Central, onde extensas faixas granito-greenstone que hospedam importantes depósitos minerais, há ampla distribuição de crostas lateríticas. Nesse estudo foram usados dados geofísicos, imagens Landsat-8 e modelos digitais de elevação para desenvolver estratégias de mapeamento do regolito em Almas, sudeste do Tocantins, Brasil. Mapas que mostram a distribuição de unidades do regolito no relevo fornecem informações relevantes desses terrenos, ajudam a direcionar a exploração mineral. Os dados foram manipulados em ambiente GIS usando álgebra de mapas em modelagem supervisionada e um robusto conjunto de dados de campo.

Com o objetivo de mapear o regolito, dois procedimentos matemáticos foram utilizados em dados de gamaespectrometria aérea em software GIS: 1. gamaespectrometria aérea e dados altimétricos integrados em lógica Booleana e fuzzy permitiram segregar as áreas com crostas lateríticas residuais ferruginosas e manganesíferas de superfície erosional com rocha e saprólito e 2. gamaespectrometria aérea e dados altimétricos integrados com estágios de intemperismo em regressão linear multivariada (estatística básica) ajudaram a estabelecer o índice regional de intensidade de intemperismo.

Razão e combinações de bandas, além de análise de componentes principais foram calculadas a partir de dados multiespectrais Landsat-8 OLI. O processamento dos dados para a região de estudo permitiu identificar áreas onde afloram rocha, saprólito e crosta laterítica (incluindo horizonte mosqueado e solo), as quais estão relacionadas a diferentes estágios de intemperismo.

Os mapas preditivos Booleano (acurácia = 91%; $\kappa = 0,69$), difuso (acurácia = 90%; $\kappa = 0,66$) e do índice de intensidade do intemperismo - WII (acurácia = 88%; $\kappa = 0,58$) foram mais eficientes no mapeamento do regolito para a área de estudo comparados aos mapas preditivos de razões de bandas (acurácia = 71%; $\kappa = 0,37$) e de componentes principais (acurácia = 61%; $\kappa = 0,32$). Esses resultados sugerem que a gamaespectrometria aérea é mais apropriada que o sensoriamento remoto óptico para mapear o regolito da região de Almas.

Embora os algoritmos desenvolvidos a partir dos dados multiespectrais Landsat-8 tenham sido menos acurados que de gamaespectrometria aérea, ambos são apropriados para mapear o regolito e devem ser usados conforme a disponibilidade dos dados para a região de interesse. Assim, a análise conjunta de dados digitais (gamaespectrometria aérea, imagens multiespectrais e modelos digitais de elevação), geológicos, mineralógicos e geoquímicos,

com devidas adaptações, podem ser aplicadas com sucesso no mapeamento das unidades do regolito e ajudar na prospecção mineral em terrenos similares de outras regiões.

Palavras-chave: crosta laterítica; operadores lógicos Booleano e difuso; regressão linear multivariada; razões de bandas; análise de componentes principais.

Abstract

In Central Brazil, where extensive granite-greenstone belts that host important mineral deposits, there is a wide distribution of lateritic duricrusts. In this study, geophysical data, Landsat-8 images and digital elevation models were used to develop regolith mapping strategies in Almas, southeastern Tocantins, Brazil. Maps showing the distribution of regolith units in the relief provide relevant information on these terrains, help direct the mineral exploration. The data sets were manipulated in a GIS environment using map algebra in supervised modeling and a robust field data set.

With the goal to easily map the regolith, two mathematical procedures were used on airborne gamma-ray spectrometry data in GIS software: 1. airborne gamma-ray spectrometry and altimetric data integrated in Boolean and fuzzy logic allowed segregating the areas with ferruginous and manganese residual lateritic duricrusts from erosional surface with rocks and saprolite and 2. airborne gamma-ray spectrometry and altimetric data integrated with weathering stages in multivariate linear regression (basic statistic) helped establish the regional weathering intensity index.

Ratios and band combinations, as well as principal component analysis were calculated from Landsat-8 OLI multispectral data. Data processing for the study region allowed the identification of areas where rock, saprolite and lateritic duricrust (including mottled horizon and soil) outcrop, which are related to different weathering stages.

The predictive maps Boolean (accuracy = 91%; $\kappa = 0.69$), $fuzzy_{FAPO}$ (accuracy = 90%; $\kappa = 0.66$) and weathering intensity index - WII (accuracy = 88%; $\kappa = 0.58$) were more efficient on mapping the regolith relative to predictive maps of band ratios (accuracy = 71%; $\kappa = 0.37$) and of principal components (accuracy = 61%; $\kappa = 0.32$). These results suggest that airborne gamma-ray spectrometry is more appropriate than optical remote sensing to the regolith map in the Almas region.

Although the algorithms developed from Landsat-8 multispectral data have been less accurate than from airborne gamma-ray spectrometry, both are suitable for mapping the regolith and should be used depending on the availability of data for the interest region. Thus, integrated analysis of digital data (airborne gamma-ray spectrometry, multispectral images e digital elevation models), geology, mineralogy, and geochemistry with appropriate adaptations can be successfully applied in the mapping of regolith units and help in mineral prospecting in similar terrains from other regions.

Keywords: lateritic duricrust; Boolean and fuzzy logic operators; multivariate linear regression; band ratios; principal component analysis.

Lista de Figuras

Lista de Tabelas

SUMÁRIO

CAPÍTULO 1

CAPÍTULO 2

CAPITULO 3

CAPÍTULO 4

ESTRUTURA DA TESE

A tese foi estruturada na forma de artigos e está organizada em quatro capítulos. O capitulo 1 compreende a introdução, estado da arte, objetivos e área de estudo. O capítulo 2 aborda aplicação de dados gamaespectrométricos e altimétricos em algoritmos de classificação para gerar mapas preditivos de crostas lateríticas. Este capítulo corresponde ao artigo 1: Boolean and fuzzy logic operators and multivariate linear regression applied to airborne gamma-ray spectrometry data for regolith mapping in granite-greenstone terrain in Midwest Brazil. O capítulo 3 aborda técnicas de processamento de dados espaciais (razão de bandas e análise de componentes principais) do Landsat-8 para obter mapas preditivos de minerais de alteração e rochas. Este capítulo corresponde ao artigo 2: Regolith mapping using band ratios and component principal analysis technics from Landsat-8 data in granite-greenstone terrain in Midwest Brazil. No capítulo 4 é apresentada uma comparação entre as eficiências dos modelos de mapeamento usados nos artigos 1 e 2.

A LATERITIZAÇÃO NO TERRENO GRANITO-GREENSTONE ALMAS-DIANÓPOLIS, TOCANTINS: UMA ABORDAGEM GAMAESPECTROMÉTRICA E ESPECTRORADIOMÉTRICA

CAPÍTULO 1

1. INTRODUÇÃO

Regolitos bem desenvolvidos e espessos ocorrem principalmente na zona intertropical moderna entre as latitudes 35° N e 35° S. Nesta zona o forte intemperismo químico favorece a transformação da rocha-mãe em produtos estáveis em ambiente superficial. Os principais exemplos estão distribuídos na Austrália, Índia, África e Brasil, onde as condições necessárias para sua formação devem existir pelo menos desde o Terciário (Costa, 1997; Tardy e Roquin, 1998; Anand e Paine, 2002; Freyssinet et al., 2005; Yang et al., 2009). O regolito pode ser definido como toda a cobertura não consolidada e secundariamente recimentada que se sobrepõe à rocha mais coerente, que foi formada por intemperismo, erosão, transporte e/ou deposição de material mais antigo. O regolito inclui rochas-mãe fraturadas e desgastadas, saprólitos, solos, acumulações orgânicas, depósitos glaciais, colúvio, aluvião, sedimentos evaporíticos e depósitos eólicos (Anand and Paine, 2002). Estudos recentes têm mostrado que o regolito é muito mais complexo do que apenas um manto de produtos de intemperismo. A interpretação acerca da natureza alóctone, autóctone, ou derivação mista alóctone-autóctone de um perfil regolítico, por exemplo, representa uma dessas complexidades (Aleva, 1994).

As características estruturais, texturais, mineralógicas e químicas de perfis lateríticos são relativamente bem estudadas na Amazônia (Angélica e Costa, 1993; Kotschoubey et al., 1997; Boulangé e Carvalho, 1997; Costa, 1997; Horbe e Costa, 1999; Peixoto e Horbe, 2008; Costa et al., 2014; Albuquerque e Horbe, 2015; Castro et al., 2016; Albuquerque et al., 2017; Horbe et al., 2021). Por outro lado pouco se conhece os efeitos da lateritização na região central do Brasil, onde os estudos são pontuais (Oliveira et al., 1992; Colin et al., 1990; Martins, 1991, 2000; Lima, 2002; CPRM, 2008; Oliveira et al., 2009, 2011), o mapeamento é escasso e os afloramentos descritos apenas de forma genérica (CPRM, 1998, 2014; SEPLAN, 1999).

Mapas preditivos para exploração do regolito podem ser elaborados usando álgebra de mapas. Esta técnica é baseada na transformação de dados numéricos para destacar objetos de interesse no terreno. Dados em camadas podem ser manipuladas para facilitar a sua interpretação por meio de uma simples sobreposição de camadas ou modelos mais elaborados (Carranza et al., 1999; Raines et al., 2010; Tomlin, 1994).

Diversas possibilidades de combinações entre os canais K, eTh e eU de dados de gamaespectrometria aérea para mapear o regolito têm sido propostas (Dickson e Scott, 1997; Wilford et al., 1997; Carrino et al, 2011; Iza et al., 2016; Albuquerque et al., 2020). As sequências das combinações formam os algoritmos. Esses algoritmos podem ser usados para mapear o regolito, com superfícies residuais de erosão e de deposição. Esta informação permite desenvolver estratégias para melhor compreender a paisagem do regolito e melhorar a interpretação da geomorfologia. Além disso, os mapas preditivos obtidos a partir de algoritmos ajudam a identificar alvos de exploração mineral para depósitos de minério primário (rocha ou saprólito) ou secundário (hospedados em crosta laterítica). Nessa mesma perspectiva, dados de sensoriamento remoto óptico têm sido amplamente usados no estudo das propriedades dos materiais da superfície da Terra (van der Werff e van der Meer, 2016). Sistemas de satélite multiespectral tais como OLI/Landsat-8, ASTER/Earth Observation (EO) (Takodjou Wambo et al., 2020; Traore et al., 2020) e sensores hiperespectrais como Hyperion (Ducart et al., 2016; Souza et al., 2021) representam os avanços no campo das ciências baseadas em análise espacial e as imagens geradas têm contribuído para refinar os mapas do regolito, tornando sua exploração mais eficiente.

Reconhecido o intemperismo como uma parte integrante do ciclo geológico, esta tese analisa o potencial uso de dados de gamaespectrometria aérea, altimetria e sensoriamento remoto multiespectral associados a técnicas matemáticas, estatísticas e de análise espacial para mapeamento do regolito na região de Almas-Dianópolis, sudeste do Tocantins.

2. ESTADO DA ARTE

Lógicas Booleana, difusa e regressão linear multivariada foram usadas na análise dos dados de gamaespectrometria aérea e altimetria. Razões de bandas espectrais e análise de componentes principais foram usadas na análise dos dados multiespectrais Landsat-8 OLI/TIRS. A análise desses dados foi complementada por dados geoquímicos e mineralógicos de amostras de crosta laterítica e rocha.

2.1. Características macroscópicas dos horizontes dos perfis lateríticos

Um perfil laterítico típico é composto, da base para o topo, pela rocha-mãe, saprólito, horizonte mosqueado, crosta laterítica, horizonte desmantelado e solo. A rocha-mãe é sotoposta ao saprólito e pode ser de qualquer natureza.

O saprólito representa o primeiro estágio de alteração da rocha-mãe e pode ser dividido em saprólito grosso e saprólito fino (ou lithomarge; Figura 1.1). Imediatamente acima da rocha-mãe está o saprólito grosso com abundantes fragmentos da rocha não-intemperizada e minerais primários preservados como litorelíctos (Figura 1.1). Sob certas circunstâncias, o saprólito grosso pode ser espesso (como freqüentemente observado em rochas graníticas), ou muito delgado (como geralmente em rochas básicas) (Trescases, 1992; Tardy, 1993). Acima do saprólito grosso está o saprólito fino no qual as estruturas da rocha-mãe e o volume original ainda estão preservadas.

O horizonte mosqueado é a parte do perfil de intemperismo que tem segregações macroscópicas de cor avermelhada que difere da matriz circundante (Tardy, 1992). Nesse horizonte, o Fe que compõe os óxi-hidróxidos é reduzido e passa para solução como Fe^{2+}, que por sua vez é remobilizado provocando manchas esbranquiçadas no perfil. Processo conhecido como desferrificação. O horizonte mosqueado evidencia a oscilação do lençol freático, o que pode provocar o isolamento de porções do material ferruginoso e resultar no endurecimento e formação de nódulos e pisólitos. O enriquecimento relativo do ferro no horizonte mosqueado pode evoluir e formar a crosta.

Crosta laterítica, *duricrust*, ferricrete, couraça, dentre outros, são termos utilizados na literatura para designar a porção endurecida superior do perfil laterítico, composta predominantemente por minerais óxi-hidróxidos de ferro (hematita, goethita, maghemita), minerais hidróxidos de alumínio (gibbsita, boehmita) e caulinita, que se desenvolveu essencialmente por processos residuais e que, portanto, tem uma ampla relação genética e composicional com o substrato (Anand e Paine, 2002). A crosta laterítica pode ter textura maciça ou, mais comumente, apresentar várias segregações secundárias tais como nódulos, pisólitos ou oólitos, além de vazios e canais.

Quando exposta a crosta laterítica fragmenta-se e forma o horizonte desmantelado, onde os nódulos, pisólitos e fragmentos de forma variada estão envolvidos pela matriz argilosa. Quando a proporção de fragmentos é maior que a de argila é dito de arcabouço fechado, quando ocorre o inverso, arcabouço aberto. Sobre esse horizonte desenvolve-se o

solo na zona de maior atividade biológica e acúmulo de detritos orgânicos. Forma-se em qualquer latitude, mas tende a ser mais espesso na zona intertropical, os quais são classificados em Latossolo, Argissolo, Espodossolo, dentre outras classes (Anand e Paine, 2002; WRB, 2015).

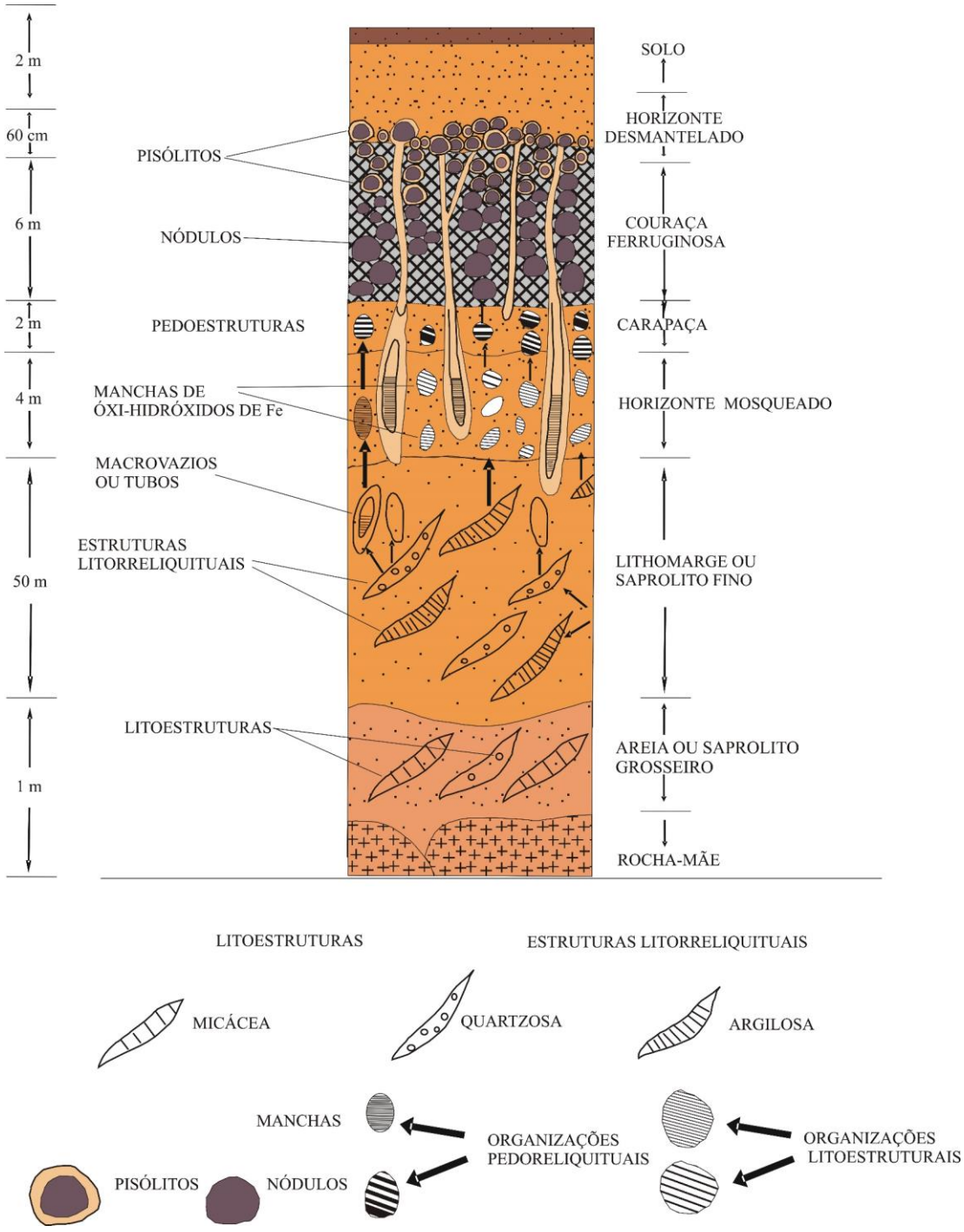

Figura 1.1 – Representação esquemática de um perfil laterítico. Da base para o topo podem ser reconhecidos os seguintes horizontes: rocha-mãe, saprólito (grosso e fino), mosqueado,

crosta laterítica (couraça ferruginosa), horizonte desmantelado e solo. Modificado de Tardy (1993).

2.2. Lateritos no contexto da cartografia e exploração mineral

Entender a história de intemperismo, a paisagem e a evolução climática, bem como as variações mineralógicas e químicas do regolito em terrenos profundamente intemperizados são importantes para uma exploração mineral eficiente. Os fatores responsáveis pelo desenvolvimento de regolitos intensamente intemperizados incluem: (a) rochas expostas aos agentes intempéricos por longo tempo com taxa de erosão menor que de acumulação; (b) rocha constituída de minerais facilmente intemperizáveis e (c) condições favoráveis de clima e biota que promovam rápidas taxas de intemperismo (Anand and Paine, 2002; Wilford, 2012). Os mecanismos envolvidos nestes fatores constituem os processos que modelam o regolito e conduzem à formação de importantes depósitos lateríticos de Al, Fe, Ni, Co, Cu e Au, dentre outros (Costa, 1997; Anand and Paine, 2002; Freyssinet et al., 2005; Yang et al., 2009).

O mapeamento do regolito é amplamente aplicado na Austrália para auxiliar na exploração geoquímica (Craig, 2001). Ouro supergênico foi encontrado em crostas lateríticas e horizontes mosqueados na maioria dos depósitos nos ambientes de savana da África, Índia e Brasil (Freyssinet et al., 1989; Santosh et al., 1990; Bowell et al., 1996; Porto e Hale, 1996; Larizatti et al., 2008). Para uma exploração mineral *greenfield* eficaz o mapeamento do regolito integrando dados mineralógicos, geoquímicos e de sensoriamento é necessário (Davy e El-Ansary, 1986; Craig, 2001; Anand e Paine, 2002; Barnes et al., 2014; Iza et al., 2018). A integração desses dados é importante especialmente em terreno profundamente intemperizado, onde a cobertura (in situ e/ou transportada) mascara as paleosuperfícies residuais e a redistribuição geoquímica devido ao intemperismo formam extensas anomalias geoquímicas maiores do que o próprio depósito de minério (Anand, 2005). Mapas mostrando as unidades do regolito e as formas de relevo fornecem relevantes informações destes terrenos, ajudam na interpretação de anomalias geoquímicas no solo, seleção de alvos e identificação de mineralização supergênica.

2.3. Geotecnologias aplicadas ao mapeamento do regolito

A aumento na capacidade de processamento tem possibilitado a integração e manipulação de um grande número de dados em pouco tempo e baixo custo. Há no mercado diversos softwares GIS que permitem ao usuário analisar dados geológicos, geofísicos, geoquímicos, altimétricos, dentre outros, de forma espacialmente integradas. Um breve referencial teórico sobre as características dos dados usados neste estudo e a forma como esses dados vêm sendo aplicados ao mapeamento preditivo do regolito, é apresentado a seguir.

2.3.1. Gamaespectrometria aérea

A gamaespectrometria refere-se a medição da radiação gama natural emitida da superfície da Terra. O instrumento usado na investigação pode atravessar a área a ser pesquisada no terreno, no ar ou dentro de um furo de sondagem. Em geral, as medições por detectores feitas de uma aeronave voando baixo são mais econômicas do que medições em campo para pesquisas de grandes áreas ou que envolvam grande número de leituras (Dentith e Mudge, 2014). Existem mais de 50 elementos radioativos que ocorrem naturalmente, mas a radiação terrestre é dominada pelos produtos da emissão de apenas três elementos: potássio (K), tório (Th) e urânio (U). Portanto, a gamaespectrometria aérea mede a abundância relativa ou concentração destes radioelementos nas rochas e materiais intemperizados. A medição de K corresponde diretamente ao pico de decaimento do ^{40}K. ^{40}K emite raios-gama quando decai para ^{40}Ar. As medições das concentrações de Th e U são mais complexas, uma vez que ^{323}Th e ^{238}U decaem ao longo de uma série de nuclídeos filhos até atingirem isótopos de Pb estáveis. Picos de emissões associados a ^{208}Tl e ^{214}Bi são usados para calcular a abundância de Th e U, respectivamente. Por isso, Th e U são geralmente expressos em partes equivalentes por milhão (eTh e eU), enquanto K é normalmente expresso em porcentagem (K%) (Minty, 1997; Wilford et al., 1997).

O K ocorre principalmente em minerais formadores de rocha primária, como K-feldspato e micas. Este elemento está presente em altas concentrações em rochas félsicas (granitos, etc.) e em baixas concentrações em rochas máficas. O Th e U são encontrados como traços em minerais formadores de rocha primária (por exemplo, feldspatos), mas são comuns em minerais acessórios e resistatos (zircões, monazita e xenotima). Ambos elementos estão presente em altas concentrações em granitos (O'Reilly et al., 1988; Dickson e Scott, 1997). A resposta gama reflete a mineralogia e geoquímica da rocha-mãe e produtos

do intemperismo, incluindo crostas lateríticas, horizontes mosqueados, argila residual e transportada, areia e cascalho (Wilford et al., 1997).

Inicialmente a gamaespectrometria aérea foi usada para detectar anomalias geoquímicas (Darnley e Ford, 1989). Técnicas semelhantes já vinham sendo aplicadas para estimar a variação espacial no teor de umidade da superfície do solo (Carroll, 1981). Wilford (1992) foi uns dos primeiros a interpretar imagens de gamaespectrometria aérea integradas a Landsat para mapeamento do regolito no norte da Austrália (Cape York Peninsula). A capacidade aparente da técnica em descrever a variação dos materiais em superfície fez com que uma sucessão de artigos sobre aplicações da gamaespectrometria aérea no estudo do regolito fossem publicados. Dentre estes artigos destacam-se Cook et al. (1996) que correlacionaram a gamaespectrometria aérea com a distribuição de materiais formadores do solo no sudoeste da Austrália; Dickson et al. (1996) e Dickson e Scott (1997) que relacionaram concentrações de K, eTh e eU à composição geoquímica de rochas e solos; Dickson and Scott (1997) e Wilford e Minty (2007) que resumiram as respostas de radioelementos de rochas e solos em termos de componentes geoquímicos e processos pedogênicos e geomórficos.

A gamaespectrometria aérea aliada a tratamento de imagens LANDSAT e SRTM, têm sido usados na identificação de padrões geofísicos e altimétricos que permitem mapear com qualidade e rapidez o regolito (Dauth, 1997; Carrino et al., 2011; Dent et al., 2013; Wilford, 2012; Grimaud et al., 2015; Arhin et al., 2015; Herrera et al., 2016; Iza et al., 2016 e 2018; Metelka et al., 2018; Albuquerque et al., 2020). Esse sucesso é basicamente devido a capacidade das crostas lateríticas desenvolvidas pelo intemperismo em clima tropical e que sustentam o relevo (Tardy e Roquin, 1998), concentrarem Th e U nos óxi-hidróxidos de Fe e nos minerais residuais (zircão e monazita) em detrimento de K (Wilford, 1995; Wilford et al. 1997; Dickson e Scott, 1997). Contudo, nem todos os valores de baixo K ou alto eTh e eU na imagem da gamaespectrometria estão associados a substratos altamente intemperizados, porque diferentes tipos de substratos podem dar respostas semelhantes (Wilford, 1997). Interpretar o grau de intemperismo e inferir taxas de processo a partir de respostas de raios gama requer o conhecimento das características do K, Th e U no substrato e no material intemperizado. Portanto, deve-se tomar cuidado com tais associações, porque para outras regiões podem ser diferentes, dependendo do tipo de rocha e do histórico de intemperismo.

2.3.2. Sensoriamento remoto óptico

O sensoriamento remoto é a ciência da aquisição, processamento e interpretação de imagens e dados coletados de aeronaves e satélites, por sensores que registram a interação entre matéria e energia eletromagnética (Sabins, 1997). Sistemas de satélite multiespectrais, como OLI/*Landsat-8*, ASTER/*Earth Observation* (EO) (Abrams et al., 2015; van der Werff e van der Meer, 2016; Metelka et al., 2017), e sensores hiperespectrais, como *Hyperion* são amplamente utilizados no estudo da superfície da Terra (Bishop et al., 2011). As imagens obtidas por esses sensores auxiliam no planejamento regional, planejamento urbano, agricultura e monitoramento dos recursos naturais (Treitz e Rogan, 2004; Hamedianfar et al., 2014; Kadhim et al., 2016). Em geologia, dados obtidos por sensoriamento remoto permitem identificar estruturas geológicas regionais e as características espectrais da superfície terrestre, auxiliando no mapeamento geológico (Hunt e Ashley, 1979; Crósta e Moore, 1989; Drury e Hunt, 1989; Drury, 2001; Deller, 2006; Pour et al., 2018; Traore et al., 2020). As limitações do sensoriamento remoto incluem: o mascaramento da mineralogia e litologia da superfície pela vegetação densa, efeitos de aquecimento residual solar e topográfico em áreas de relevo moderado a alto e alta sensibilidade ao intemperismo (Watson et al., 2001).

O sensoriamento remoto é uma poderosa ferramenta tecnológica para compreensão do modelado da paisagem e mapeamento do regolito (Souza et al., 2021). Essa tecnologia permite mapear a reflectância espectral da superfície e caracterizar sua composição mineral. As assinaturas são quantificadas de acordo com a razão entre energia refletida (radiância) e a energia incidente (irradiância) de um alvo definido, cujo resultado mede a reflectância (Clark, 1999). A espectroscopia de reflectância envolve a medição da radiação eletromagnética (REM) refletida de alvos em diferentes comprimentos de onda entre o visível e (VIS) e o infravermelho de ondas curtas (SWIR) (0,3 – 2,5 μm), o que resulta em assinaturas espectrais. Nesta faixa espectral alguns componentes tais como óxi-hidróxidos de ferro, materiais orgânicos, carbonatos (CO_3), sulfatos (SO_4), bem como vibrações típicas de transição catiônica presente em filossilicatos (por exemplo, -OH, Al-OH, Mg-OH e Fe-OH em argila, mica e serpentina) podem ser identificados (Grove et al., 1995; Vicente e Souza Filho, 2011).

Embora não seja possível identificar os elementos-traço econômicos (Ni, Au, Ag, Cu, dentre outros) contidos ou adsorvidos aos minerais diretamente por qualquer sensor

remoto, esses minerais podem ser detectados a partir de minerais associados a zonas alteração hidrotermal que possuem assinaturas espectrais diagnósticas principalmente na faixa do infravermelho de ondas curtas (SWIR) do espectro eletromagnético (Bedell et al., 2009; Crósta et al. 2009). As imagens multiespectrais Landsat-8 oferecem faixas de comprimentos de onda que podem ser sensíveis a minerais de alteração em áreas com cobertura vegetal (Guerschman et al. 2015). Dados multiespectrais (imagens Landsat-8/OLI) e hiperespectrais (EO-1/Hyperion) foram usadas na exploração de depósitos de ferro na Província Mineral de Carajás, Brasil (Ducart et al., 2016). McBratney e De Gruijter (1992) discutiram em detalhes a necessidade de uma abordagem mais contínua para classificação de solos e consideram métodos com base em algoritmos difusos mais apropriados para o mapeamento preditivo do regolito.

Razões entre bandas e combinações

Razões de banda são combinações aritméticas simples de bandas diferentes que ressaltam a distribuição e intensidade de absorção ou emissão a serem investigadas de forma semiquantitativa (Sabins, 1997). Nesta técnica, o valor do número digital de uma banda é dividido pelo valor do número digital de outra banda. Nas últimas décadas várias razões de banda foram amplamente utilizadas e desenvolvidas para litologia e mapeamento mineralógico (Abrams et al., 1983; Kaufman, 1988; Sabins, 1997; Carranza e Hale, 2002; Vicente e Souza Filho, 2011; Pour et al., 2018, Traore et al., 2020). As operações entre bandas podem evidenciar diferenças sutis no comportamento espectral de diferentes objetos, o que permite diferenciar vários alvos na mesma imagem, que podem não ser visíveis em bandas brutas (Inzana et al., 2003).

Análise de componentes principais

A análise de componentes principais (PCA) é uma técnica estatística multivariada para reduzir a dimensionalidade dos dados. Ele seleciona combinações lineares (cargas de autovetores) de variáveis de forma que cada componente extraia sucessivamente uma combinação linear com uma variância menor (Singh e Harrison, 1985). Os princípios matemáticos da técnica estão bem estabelecidos e encontrou extensas explicações em quase todas as disciplinas das ciências físicas e engenharia (Johnson e Wichern, 2007; Gupta et al., 2013). Crósta e Moore (1989) relacionam os carregamentos de autovetores de componentes

principais com informações de mapa para todas as bandas. Uma imagem de PCA com carga de autovetor moderada a alta para bandas reflexivas e absortivas diagnósticas de mineral ou grupo mineral de sinais opostos realça esse mineral. Quando o carregamento é positivo na faixa reflexiva do mineral, os pixels aparecem na imagem em tons claros. Quando o carregamento é negativo, os pixels aparecem em tom escuro para o mineral investigado (Gupta et al., 2013; Tangestani e Moore, 2000). Loughlin (1991) propõe um método de entrada seletiva de dois conjuntos de quatro bandas da imagem para a PCA, o qual denominou Técnica Crósta.

2.3.3. Dados de campo e laboratório

Os dados de campo foram obtidos durante campanha de mapeamento geológico prévio à elaboração dos mapas preditivos. Esses dados, os quais compreendem basicamente coleta de amostras e descrição de afloramentos e perfis, foram checados e complementados em campanhas posteriores para aperfeiçoamento do modelo e obtenção de mapas preditivos mais acurados para o regolito da região de estudo.

A geoquímica das amostras além de possibilitar o estabelecimento de correlações entre a rocha-mãe e os demais horizontes do perfil de intemperismo, quando combinada a outros tipos de dados (e.g., gamaespectrométricos, espectroscópicos, altimétricos) por meio ferramentas estatísticas e lógicas matemáticas (e.g., regressão linear multivariada, clusterização hierárquica aglomerativa, Booleana e difusa) ajudam a validar as informações obtidas remotamente e podem revelar informações valiosas para o mapeamento do regolito e prospecção mineral (Carrino et al., 2011; Martelet et al., 2013; Campos et al., 2017; Iza et al., 2018). Resultados de aplicações dessas ferramentas estatísticas e lógicas para mapeamento do regolito têm sido publicados timidamente no Brasil (Carrino et al., 2011; Iza et al., 2018; Campos et al., 2017; Albuquerque et al., 2020).

3. OBJETIVOS

Dentre os objetivos deste estudo destacam-se:

1 - Encontrar padrões utilizando dados gamaespectrométricos e altimétricos em ambiente GIS que permitam mapear de forma sistemática e rápida o regolito.

2 – Desenvolver o mapa do regolito a partir do índice de intensidade de intemperismo (WII) adaptado para a região de Almas;

3 - Buscar assinaturas em imagens multiespectrais Landsat-8 que permitam elaborar mapas preditivos para o regolito em Almas;

4 – Desenvolver a modelagem mais apropriada para mapear regolito em áreas arrasadas e com grande diversidade geológica, a partir de dados de gamaespectrometria aérea, multiespectrais Landsat-8 OLI, altimétricos e geoquímicos;

5 – Identificar limitações das técnicas utilizadas no mapeamento do regolito em Almas.

4. ÁREA DE ESTUDO

Para este estudo foi selecionada a região de Almas, sudeste do Tocantins (Figura 1.2). A região faz parte do Brasil Central e está inserida no contexto geológico da Província Tocantins (Almeida et al., 1981). Esta província é resultado da convergência e colisão entre os paleocontinentes Amazonia e São Francisco durante a orogenia brasiliana do Neoproterozóico. A junção desses fragmentos litosféricos "descendentes de Rodínia" corresponde à aglutinação da porção oeste do Supercontinente Gondwana ocorrida no final do Neoproterozóico. A sedimentação fanerozóica no norte da província originou a Bacia do Parnaíba enquanto no sul a Bacia do Paraná (Fuck et al., 2017).

A Província Tocantins engloba três faixas de dobramentos e empurrões neoproterozóicos: Araguaia e Paraguai, a sudeste e sul do Cráton Amazônico, respectivamente, e Faixa Brasília (*Northern Brasília Belt and Southern Brasília Belt*), desenvolvida ao longo da margem oeste do Cráton São Francisco (Fuck et al., 2017). A partir de associações petrográficas a Faixa Brasília foi compartimentada em três zonas principais: cratônica, externa e interna (Pimentel et al., 1999, 2004; Dardenne, 2000; Valeriano et al., 2008). Nesse contexto, a área de estudo está inserida no domínio da zona externa setentrional. Zona que inclui uma espessa sucessão de rochas sedimentares e metassedimentares de idade Proterozóica (1750-600 Ma) deformadas pela colisão com a margem oeste do Cráton São Francisco, além de amplas exposições do embasamento siálico (Alckmim e Martins Neto, 2012).

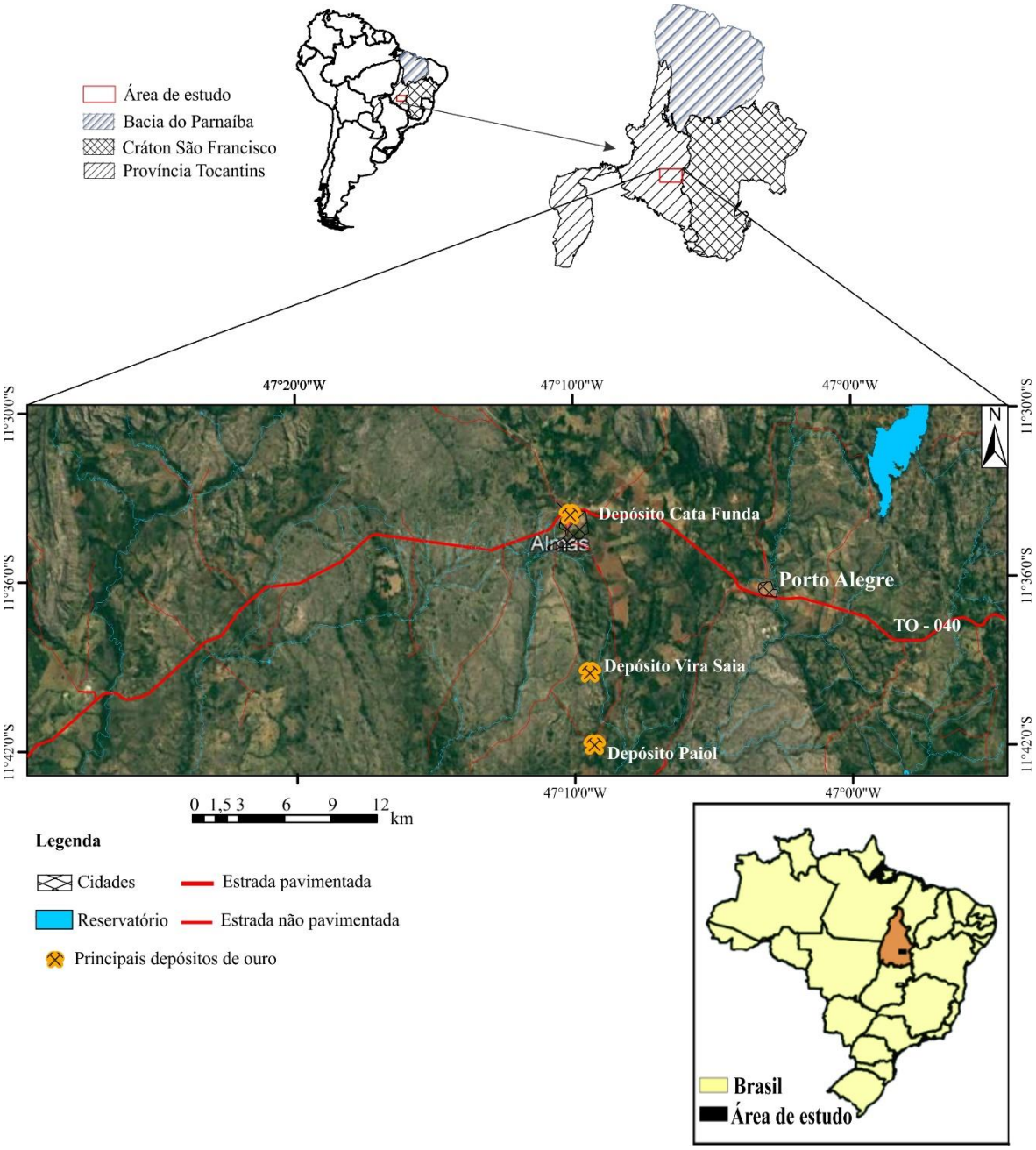

Figura 1.2 – Localização da área de estudo.

4.1. Geologia e geomorfologia

O embasamento da Faixa Brasília na porção norte tem diferentes denominações: Terreno Almas-Dianópolis (Costa, 1985), Terreno Arraias-Natividade (Fuck et al., 2001), Terreno Granito-Greenstone Tocantins (Kuyumjian et al., 2012), dentre outras. As faixas dos greenstone belts distribuem-se linearmente em forma de Y e dispostas na direção NS com ramificações para NE (Figura. 2.1; Costa et al., 1976; Cruz e Kuyumjian, 1998). Estas

rochas são as mais antigas da região e foram reunidas no Grupo Riachão do Ouro (Arqueano). Esse grupo é composto por uma unidade basal representada por rochas metavulcânicas (Formação Córrego do Paiol) como metabasaltos, anfibolito com granada, actinolita clorita xisto, granada anfibolito, metandesito, e outra de topo por rochas metassedimentares (Formação Morro do Carneiro) como metaconglomerado, filito, filito sericítico, quartzito, quartzo- muscovita xisto e formação ferrífera bandada (itabirito).

O Complexo Tonalito-Trondhjemito-Granodiorito – TTG é a unidade de maior distribuição na área. Ocorre na forma de plútons graníticos de idade Paleoproterozóica, fracamente foliados, com bandamento gnáissico localizado, intrusivos no Grupo Riachão do Ouro, configurando típico padrão de domos e quilhas comum em terrenos granito-greenstone (Costa et al., 1976; Cruz e Kuyumjian, 1998). Esta unidade compreende tonalitos (leucotonalito, metatonalito), hornblenda metatonalito, biotita metatonalito e hornblenda gabro que afloram principalmente na forma de lajedos (Campos et al., 2016). Na porção leste e, subordinadamente, centro-sul da área dominam tonalitos e granodioritos com quantidades variadas de biotita e hornblenda da Suíte Serra do Boqueirão (Paleoproterozóico). Estes granitoides apresentam feições típicas de mistura de magmas, xenólitos de anfibolito e enclaves de rochas do Grupo Riachão do Ouro. Na porção sudoeste da área afloram hornblenda metatonalitos, metatonalito com biotita, leucogabros e hornblenda metadiorito do Complexo Riacho do Mato. Essas rochas foram metamorfizadas a baixo grau (xisto verde) e preservam feições típicas de mistura de magmas e bandamento ígneo. Haviam sido cartografadas na região de Dianópolis (Sabóia et al., 2015), mas só recentemente foram descritas em detalhe e proposta a denominação formal (Campos et al., 2016). É uma unidade paleoproterozóica intrusiva no TTG. Corpos circulares a subcirculares de hornblenda gabro intrusivos no Grupo Riachão do Ouro e Complexo TTG correspondem à unidade Intrusivas Máficas-ultramáficas do tipo Gameleira. As idades Rb-Sr de 2050 ± 276 Ma e 2217 ± 85 Ma fornecem uma idade mínima de intrusão do granitóide na sequência greenstone (Costa, 1985).

Quartzito micáceo paleoproterozóico, folhelho sericítico, carbonato e metargilitos carbonosos (Grupo Natividade) estão situados ao longo de cristas alinhadas NNE de 500 a 800 m de altura nas partes centro-norte e oeste da região (Serra da Natividade, Figura 2.1). O contato de todas essas unidades com a cobertura laterítica, que se presume ser Cenozóica, é gradacional.

As altitudes na área da pesquisa variam entre 300 e 780 m. Compreende três unidades morfoestruturais: i) Serra da Natividade, na porção oeste, marcada por relevo elevado (500 – 800 m), escarpado e muito íngreme, sustentado por rochas metassedimentares do Grupo Natividade, portanto mais resistentes ao intemperismo; ii) Depressão do Alto Tocantins, ocupa a porção central da área, caracterizada por relevo arrasado (~350 m), intensamente lateritizado, baixa declividade, correspondente ao domínio das metavulcanossedimentares do Grupo Riachão do Ouro e granitóides do Complexo TTG; e iii) Patamares das Mangabeiras na porção extremo leste da área, caracterizado por relevo ondulado e elevado (~500 m), topos convexos a tabulares, menos dissecados que a Depressão do Alto Tocantins, formados por granitóides da Suíte Serra do Boqueirão (SEPLAN, 1999; Campos et al., 2016; Figura. 2.1.).

As crostas lateríticas têm coloração marrom-avermelhada a amarelada, têm textura vermiforme a maciça e protopisolíticas a pisolíticas (perfis 1, 2, 3 das Figuras 2.2, 2.3 e 2.4). A crosta laterítica ferruginosa consiste principalmente de hematita, goethita, caulinita, gibbsita, quartzo e anatásio, além de muscovita, albita e rutilo como minerais residuais. Quando derivada do gabro, a crosta laterítica ferruginosa é cinza, maciça e contém todorokita, além dos minerais mencionados (crosta laterítica manganesífera, perfil 4 das Figuras 2.2, 2.4C e D). Ambas as crostas lateríticas são cobertas localmente por Ferralsols e Acrisols (de acordo com a taxonomia do solo WRB, 2015).

4.2. Mineralizações de ouro na área de estudo

Paiol, Vira Saia e Cata Funda são os três principais depósitos de ouro na região de estudo (Figura 1.2). Esses depósitos de ouro, classificados como orogênicos, são do tipo mesotérmicos hospedados em zonas de cisalhamento (Cruz e Kuyumjian, 1999; Cruz e Kuyumjian, 2006), estão localizados ao longo de 15 km de corredor do terreno granito-greenstone. O depósito do Paiol é bem conhecido pelo ouro do saprólito que foi extraído em escala industrial (2 Mt de minério processado a 2,5 g/t Au) de 1996 a 2001. A mineralização do ouro está hospedada em anfibolito com zonas de cisalhamento hidrotemal acima 1400 m de comprimento, 330 m de largura e 400 m de profundidade. O depósito Vira Saia está hospedado em um corpo metatonalítico cortado por zonas de cisalhamento rúptil-dúctil sinistral, e o depósito Cata Funda está hospedado em saprólito, fraturas, veios e zonas de cisalhamento desenvolvidas em rochas metabásicas e metassedimentares (Martins-Ferreira

et al., 2017). Nenhuma mineralização de ouro foi encontrada nas lajes, blocos, concreções e nódulos de crostas lateríticas.

CAPÍTULO 2

ARTIGO CIENTÍFICO 1

BOOLEAN AND FUZZY LOGIC OPERATORS AND MULTIVARIATE LINEAR REGRESSION APPLIED TO AIRBORNE GAMMA-RAY SPECTROMETRY DATA FOR REGOLITH MAPPING IN GRANITE-GREENSTONE TERRAIN IN MIDWEST BRAZIL

Journal of South American Earth Sciences 112 (2021) 103562

Contents lists available at ScienceDirect

Journal of South American Earth Sciences

journal homepage: www.elsevier.com/locate/jsames

Boolean and fuzzy logic operators and multivariate linear regression applied to airborne gamma-ray spectrometry data for regolith mapping in granite-greenstone terrain in Midwest Brazil

Sanclever Freire Peixoto [a,b,*], Adriana Maria Coimbra Horbe [a], Túlio Marques Soares [a], Caroline Araújo Freitas [a], Endel Muller Dalat de Sousa [a], Edgar Romeo Herrera de Figueiredo Iza [c]

[a] Universidade de Brasília, Instituto de Geociências, Campus Universitário Darcy Ribeiro, Distrito Federal, Brasília, 70910-900, Brazil
[b] Instituto Natureza do Tocantins-NATURATINS, Q. 302, Norte Alameda 1, s/n - Lote 3, Plano Diretor Norte, Palmas, TO, 77006-336, Brazil
[c] Serviço Geológico do Brasil-CPRM, Salvador, Brazil

ARTICLE INFO

Keywords:
Ferruginous and manganese lateritic duricrusts
Fuzzy logic
Boolean logic
Multivariate linear regression
Map algebra
Weathering intensity index

ABSTRACT

Recent studies have proposed several possibilities of combining K, Th and U airborne gamma-ray spectrometry channels to generate predictive algorithms maps. These algorithms can be used for mapping regolith in deeply weathered terrains with residual, erosion, and deposition surfaces helping to developed strategies to better understand the regolith landscape and to improve geomorphology interpretation, and to identify mineral exploration target sites for primary (bedrock or saprolite) or supergene (hosted in lateritic duricrust) ore deposits. With the goal to easily map the regolith, two mathematical procedures were used on airborne gamma-ray spectrometry data in GIS software, validated by fieldwork on granite-greenstone belts in Midwest Brazil: 1. airborne gamma-ray spectrometry and altimetric data integrated in Boolean and fuzzy logic allowed segregating the areas with ferruginous and manganese residual lateritic duricrusts from erosional surface with rocks and saprolite with 90% of accuracy ($\kappa_{Boolean} = 0.69$ and $\kappa_{FAPO} = 0.66$) and 2. airborne gamma-ray spectrometry and altimetric data integrated with weathering stages in multivariate linear regression (basic statistic) helped establish the regional weathering intensity index, with acceptable error (r^2 adjusted >0.6 and p-value < 5%). These two modeling techniques provide useful, accurate, rapidly and complementary regolith maps and can be applied in large regions for preliminary interpretations.

1. Introduction

Deeply weathered regolith occurs mainly in the modern intertropical zone, where strong chemical weathering favors rock transformation, giving rise to stable products in a superficial environment (Costa, 1997; Horbe and Costa, 1999; Anand and Paine, 2002; Freyssinet et al., 2005; Yang et al., 2009; Anand and Butt, 2010). Predictive mapping tools comprise a set of data processing techniques used in GIScience, which can be a "simple" overlay of data layers or an advanced coordinated multiple view environment data layers with complex models on a desktop (Carranza, 2011; Ormeling and Kraak, 2008). Predictive mapping tools can be easily tested and applied to large regions, based on their characteristics such as the density of vegetation cover, humidity, and the extent of anthropization by agriculture and livestock, thereby helping develop strategies for accurate and rapid regolith exploration.

Supergene gold was found in lateritic duricrusts and mottled horizons in most deposits in the savanna environments of Africa, India, and Brazil (Freyssinet et al., 1989; Santosh et al., 1990; Bowell et al., 1996; Porto and Hale, 1996; Larizatti et al., 2008). For effective greenfield mineral exploration, regolith mapping using integrating mineralogical and geochemical data (*e.g.*, Davy and El-Ansary, 1986; Anand and Paine, 2002; Barnes et al., 2014; Iza et al., 2018) is necessary, especially in a deeply weathered terrain where the overburdens mask paleo residual surfaces and the geochemical redistribution due to weathering forms extensive geochemical anomalies larger than the ore deposit itself (Anand, 2001). Maps showing the distribution of landform-regolith units provide relevant and sometimes subtle information of these terrains, help target selection, and may help in interpreting soil

* Corresponding author. Universidade de Brasília, Instituto de Geociências, Campus Universitário Darcy Ribeiro, Distrito Federal, Brasília, 70910-900, Brazil.
E-mail address: sancleverp@yahoo.com.br (S.F. Peixoto).

https://doi.org/10.1016/j.jsames.2021.103562
Received 17 December 2020; Received in revised form 21 August 2021; Accepted 9 September 2021
Available online 20 September 2021
0895-9811/

geochemical anomalies and identifying supergene mineralization (Smith et al., 2000).

Potassium (K) occurs mainly in primary rock-forming minerals, such as K-feldspar and micas. It is present in high concentrations in felsic rocks (granites, etc.) and low concentrations in mafic rocks. Thorium (Th) and uranium (U) are found as traces in primary rock-forming minerals (e.g., feldspars), but are common in accessory and resistate minerals (zircons, monazite, and xenotime). Th and U occur in high concentrations in granites and K is scarce in mafic rocks (O'Reilly et al., 1988; Dickson and Scott, 1997). The gamma-response reflects the mineralogy and geochemistry of the parent rock, and weathering products, including lateritic duricrusts, mottled horizons, residual and transported clay, sand and gravel (Wilford et al., 1997). Different techniques for the analysis of airborne gamma-ray spectrometry data have been proposed ranging from the ratios of the radiometric channels (Dickson and Scott, 1997; Wilford et al., 1997), agglomerative hierarchical clustering (Martelet et al., 2006), Boolean and fuzzy logic operators (Porwal et al., 2015; Iza et al., 2016), multivariate linear regression (Wilford, 2012; Martelet et al., 2013), artificial neural network classification (Metelka et al., 2018), to combination with optical remote sensing datasets (Voll et al., 2020). Integrated interpretation of airborne gamma-ray spectrometry and Shuttle Radar Topography Mission (SRTM) images has been used to identify geophysical patterns of extensive regolith cover (Dauth, 1997; Jayawardhana and Sheard, 2000; Wilford et al., 1997; Dent et al., 2013; Arhin et al., 2015; Grimaud et al., 2015; Moonjun et al., 2017; Albuquerque et al., 2020). The successful combination of gamma-ray spectrometry and altimetric data in the regolith mapping is because of the capacity of residual lateritic duricrust to concentrate Th, U, and other trace elements on both Fe oxi-hidroxides and residual minerals (zircon and monazite), relative to the parent rocks (Wilford, 1995; Wilford et al., 1997; Dickson and Scott, 1997). This also allows classification of the regolith in weathering regional indexes that indicate the degree to which primary minerals have been altered to form clay minerals and oxides (Wilford, 2012; Iza et al., 2018).

Minas Gerais, Goiás, and Tocantins states in Midwest Brazil have extensive granite-greenstone terrains that host important mineral deposits (Rio das Velhas, Guarinos, Crixás, Faina and Tocantins; Cruz and Kuyumjian, 1998; Pimentel et al., 2000; Lobato et al., 2001; Jost and Fortes, 2001; Jost et al., 2010; Oliveira et al., 2004, 2015; Corrêa et al., 2015; Martins-Ferreira et al., 2017). Airborne gamma-ray spectrometry has been successfully used to identify primary Cu and Au deposits and Ni-bearing mafic-ultramafic bodies in these regions (Silva et al., 2003; Barbosa et al., 2013; Campos et al., 2017). Pires (1995) showed that Au mineralization in hydrothermal alteration zones in the Crixás deposit, Faina Greenstone Belt, were associated with anomalous concentrations of K whereas Campos et al. (2017) indicated the presence of new targets in the Faina greenstone belt.

This paper reports predictive mapping tools for mapping regoliths

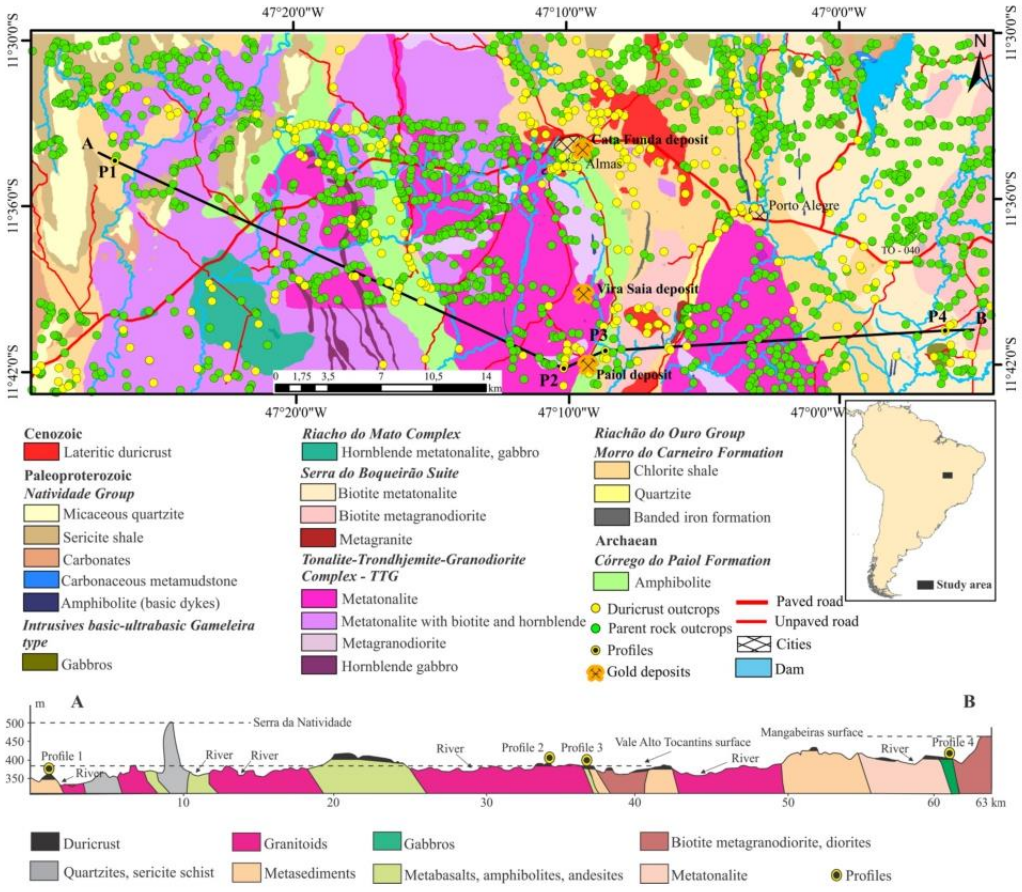

Fig. 1. Geological map of the study region (after CPRM, 2014 and Campos et al., 2016) and cross-section along the A–B transect. The cross-section shows the lithological units and highlights the regolith features (*e.g.*, altitude, slope).

using airborne gamma-ray spectrometry in a granite-greenstone terrain in Midwest Brazil, which contains extensive primary Au ore deposits in saprolite and bedrock surrounded by residual lateritic duricrust (Fig. 1). As the previous maps of the Almas-Dianópolis region did not consider regolith, there was a need to reinterpret the airborne gamma-ray spectrometry data for the study area (CPRM, 2006, 2014). The study aims to develop geocomputational modeling tools that contribute to the delineation of mineral exploration targets in an area where there is a wide variety of rocks. The main contribution it provides to geosciences is that the algorithms developed to apply to differentiate areas of saprolite and parent rock from areas of lateritic duricrusts, and thus serve as a guideline for regional gold exploration. The geochemical variations of radioelements U, Th and K, measured from airborne gamma-ray spectrometry survey together with elevation data from a digital elevation model, and field outcrops observations in training sites that describe the degree of weathering, are used to generate a weathering intensity index (WII). The algorithms processed eU, eTh, K, and elevation variables in supervised classification with Boolean and fuzzy logic operators and multivariate linear regression with WII.

2. Geology, geomorphology, and gold mineralization

The meta-volcano sedimentary NS-trending greenstone sequence (Fig. 1) with the Sm–Nd model aged 2508 Ma, that occurs in the central part of the study region (Cruz and Kuyumjian, 1999; CPRM, 2014; Campos et al., 2016), is composed by basalt, garnet amphibolite, actinolite-chlorite schist, and andesite (Córrego do Paiol Formation) overlaid by a metasedimentary sequence of metaconglomerate, muscovite-chlorite schists, sericitic phyllite, quartzite, muscovite shale, and banded iron formation (Morro do Carneiro Formation) (Borges, 1993; Cruz and Kuyumjian, 1998; Kuyumjian et al., 2012). These two units (the Riachão do Ouro Group) are intruded by tonalite, hornblende-biotite metatonalite, biotite metagranodiorite, and hornblende gabbro plutons (TTG Complex, Serra do Boqueirão Suite, and Riacho do Mato Complex) and cut by NS-striking amphibolite and micro gabbro dikes (Fig. 1). The Rb–Sr ages of 2050 ± 276 Ma and 2217 ± 85 Ma provide a minimum age of granitoid intrusion in the greenstone sequence (Costa, 1985). Paleoproterozoic micaceous quartzite, sericite shale, carbonate, and carbonaceous metargilites (Natividade Group) are situated along the 500–800 m high NNE aligned hills in the central-northern and western parts of the region (Serra da Natividade, Fig. 1). The contact of all these units with the lateritic cover, which is assumed to be Cenozoic, is gradational.

Slabs, blocks, concretions, and nodules of lateritic duricrusts occur in almost the entire study region, except in the central-northern and western parts (>488 m) (Oliveira and Campos, 1991; SEPLAN, 2012; CPRM, 2014; Campos et al., 2016). This sustains the undulating relief with tabular tops of the Vale do Alto Tocantins surface in the south-central part and of the Mangabeiras surface in the extreme eastern part of the study region (348–488 m high) (Figs. 1–4).

The lateritic duricrusts are reddish-brown to yellowish in color, have massive to vermiform texture, and are protopisolitic to pisolitic (profiles 1, 2, and 3 of Figs. 2–4). The lateritic duricrust consists mainly of quartz, hematite, goethite, kaolinite, gibbsite, and anatase, while having muscovite, albite, and rutile as residual minerals. However, on the gabbro, the lateritic duricrust is gray, massive, and contains todorokite, in addition to the above-mentioned minerals (manganese duricrust, profile 4 of Figs. 2 and 4C, and D). Both lateritic duricrusts are locally covered by Ferralsols and Acrisols (as per the WRB soil taxonomy WRB, 2015).

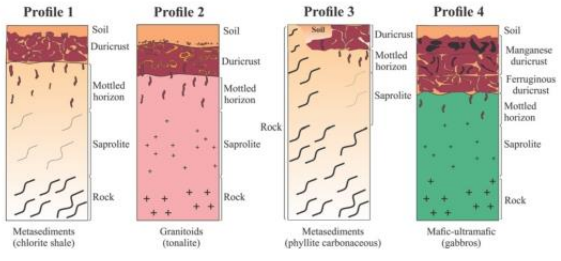

Fig. 2. Weathering lateritic profiles of the study region.

Paiol, Vira Saia, and Cata Funda are the three main gold deposits in the study region (Fig. 1). These gold deposits, classified as orogenic, shear-hosted mesothermal deposits (Cruz and Kuyumjian, 1999, 2006), are located along 15 km of the granite-greenstone terrain corridor. The Paiol deposit is well-known as gold from the saprolite was mined at an industrial scale (2 Mt of processed ore at 2.5 g/t Au) from 1996 to 2001. The gold mineralization is hosted in amphibolites with hydrothermal shear zones that are over 1400 m long, 330 m wide, and 400 m deep. The Vira Saia deposit is hosted in a metatonalitic body cut by a sinistral brittle-ductile shear zone system, and the Cata Funda deposit is hosted on saprolite, fractures, veins, and shear zones developed in metabasic and metasedimentary rocks (Martins-Ferreira et al., 2017). No gold mineralization was found in the slabs, blocks, concretions, and nodules of lateritic duricrusts.

3. Materials and methods

The airborne gamma-ray data used for predictive mapping were acquired from the Tocantins Aerogeophysical Project (CPRM, 2006) flown between July 2005 to January 2006, which coincides with the dry season in the region, and processed by Aerogeophysica Latinoamerica (AGP-LA) under the supervision of the Geological Survey of Brazil (CPRM). The average flight height was 100 m, with flight and control lines spaced 0.5 and 10 km apart, respectively. The aircraft was equipped with a spectrometer of 256 channels and a detector system made of sodium iodide crystals doped with thallium with 2816 cubic inches downward-looking and 512 cubic inches upward-looking detectors. The data were collected depending on flight speed on the transect, that is, approximately integrating the signal over a 75 m distance every second. In the phase prior to the airborne survey, the equipment were tested for data quality and control. Downward-looking detectors were subjected to static calibration with calibration pads and dynamic calibration with flights over dynamic calibration range (DCR) and the ocean. The conversion of counts per second (cps) to the concentration of elements was based on flights over the DCR. Upward-looking detectors were calibrated in high-level flight tests (2500 feet).

The data were corrected by AGP-LA, which adopted the recommendations of the International Atomic Energy Agency (1991). The main steps were: (a) filtering the altimeter radar data, cosmic radiation channel, and uranium to reduce the effects of high-frequency radiation; (b) correction of effective flight height based on environmental temperature and pressure; (c) removing contributions from the aircraft background and cosmic radiation components in each window of the spectrometer; (d) removal of radon background from measurements performed on the uranium window by the upward-looking detector; (e) estimation of sky shine coefficients related to uranium and thorium radiation; (f) correction of the Compton scattering; and (g) correction of altimetry based on the nominal height of the airborne survey and atmospheric attenuation.

The negative values of eU, eTh, and K concentrations, caused by the inadequate atmospheric background correction and/or instrumental calibration processes used in the Tocantins Aerogeophysical Project, were set to zero for this study. The errors in gamma-ray spectrometry data, also called dummies, although small in number and intensity can distort the results, especially when they assume negative values because the inputs used in the modeling are composed by division and multiplication of radioelements.

Airborne gamma-ray and altimetric data were further processed

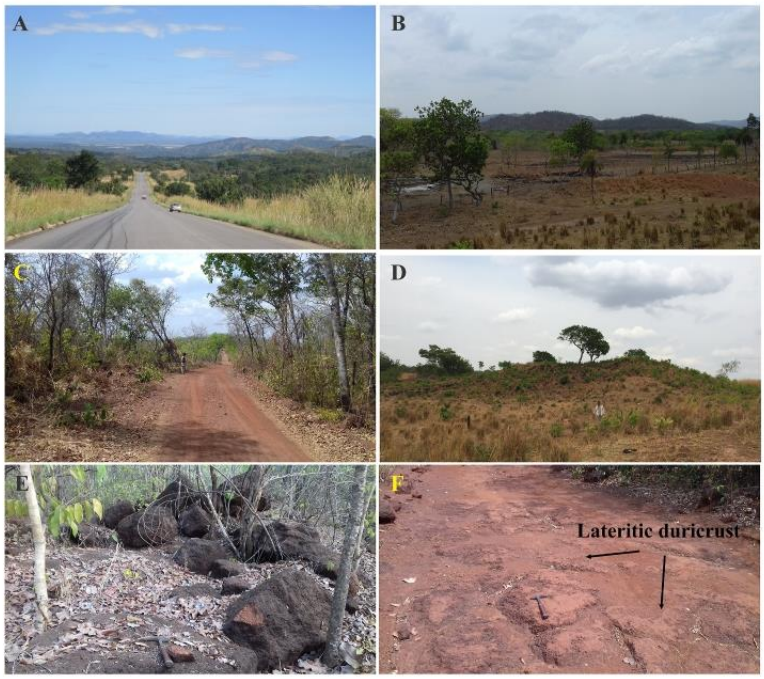

Fig. 3. Regolith landscape of the area. A - view of the greenstone belt (Almas-Dianópolis) highlighting hills lined up to the bottom of the landscape (Mangabeiras surface and Serra da Natividade); B - contrast between low and high relief (Mangabeiras surface) located in the southeastern part of the area; C and D - inselbergs supported by duricrust (Vale do Alto Tocantins surface); E – lateritic duricrust outcrops in blocks; and F - in slabs.

using Oasis Montaj (Geosoft) and ArcGIS (Esri) softwares. The map algebra technique based on transforming numerical data allows highlighting objects of interest on the ground surface (Carranza et al., 1999; Raines et al., 2010; Tomlin, 1994). The characteristics of these data and the way they are transformed into maps are presented in the following sections. The lateritic duricrust has the ability to retain eTh and eU in the Fe oxi-hidroxides relative to the chemical composition of the less leached substrate (saprolite and parent rock) (Wilford et al., 1997; Dickson and Scott, 1997). This allows preparation of predictive maps using airborne gamma-ray data, which when combined with other data (*e.g.*, petrographic, geochemical, aeromagnetic, spectroscopic) can contribute as a guide for regolith studies and can indicate new target sites for ore deposits.

The airborne gamma-ray data (eU, eTh, and K channels) was reclipped from the total region under the Tocantins Aerogeophysical Project and WGS84 was used as the spatial reference system. These data (geodatabases) were interpolated based on minimum curvature, with a 125 m grid cell size, corresponding to a quarter of the spacing between the flight lines (Fig. 5).

For the geochemical study of the regolith, 27 samples were selected from lateritic duricrust (23) and parent rock (4). They were collected in lateritic duricrust and rock slabs outcrops (>30 m^2) that form the tabular tops of the Vale do Alto Tocantins surface distributed throughout the study region. No samples were collected in the incised valley and riverbed because lateritic duricrusts were not found in these locations. The samples were dried in an oven (60 °C), pulverised, and extracted as aliquots for chemical and mineralogical analysis. Chemical analyses were performed by ALS-Laboratory Services. The major elements (SiO_2, Al_2O_3, Fe_2O_3, TiO_2, MgO, CaO, Na_2O e K_2O, P_2O, and MnO) were analyzed by ICP-ES after fusion with $LiBO_2$ and loss to fire (LOI) by gravimetry. The Th and U were analyzed by ICP-MS. The minerals were identified by X-ray diffraction (RIGAKU IV equipped with a Cu tube) in the laboratory of Universidade de Brasília (UnB).

3.1. Boolean and fuzzy logics applied to regolith mapping

Techniques based on Boolean and fuzzy logic operations are used in the construction of knowledge-driven models, i.e., models based on previous information or hypotheses made by an expert (Bonham-Carter, 1994). Boolean logic consists of applying mathematics to human reasoning. It uses the classical theory of sets, in which an element is or is not a part of a set. Logical complementation (NOT), logical multiplication (AND), and logical addition (OR) are the operations that are applied to a data set. The Index Overlay Method (IOM), associated with this logic, allows assigning different weights to the variables while the average normalized by the sum of weights (weight-weighted average) allows identifying the influence of each variable in binary (0 or 1) format (Bonham-Carter, 1994). The resulting maps allow to differentiate exposed areas of parent rock and saprolite from areas with lateritic duricrusts. It is emphasized that the prior traditional mapping of the region was essential for guiding the study. The choice of data, the kinds of information extracted from it, and the assignment of weights to evidence were dependent on the environment regional (Midwest Brazil context). For example, vegetation map was not employed, because it is not directly useable as lateritic duricrust evidence; as well as lower weight assigned to elevation relative to the airborne gamma-ray data, because lateritic duricrust had been observed over a relatively wide range of altitudes.

Fuzzy or diffuse logic is an outgrowth theory of sets (Zadeh, 1965), where the transition between favorable and non-favorable areas can be gradual rather than abrupt (Boolean logic), assuming any value in the interval between 0 and 1. The membership function of a fuzzy set A is denoted by $\mu A(x)$ and usually has the form $\mu A: X \rightarrow [0, 1]$, where X is the universal set under consideration and A is a label of the fuzzy set defined

Fig. 4. Lateritic duricrust textures. A - vermiform to protonodular; B - vermiform; C - manganese vermiform; D - vermiform and massive manganese; E – pisolitic; and F - vermiform with botryoidal goethite.

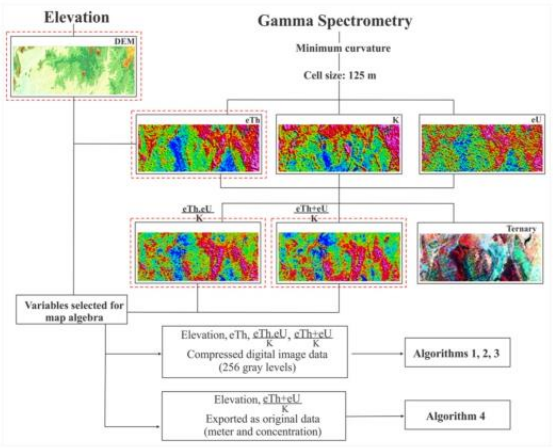

Fig. 5. Data processing flowchart and alternative products from algorithms 1, 2, 3 and 4. Respective colorbars of K, eTh, and eU are presented in Fig. 7.

by this function. The universal set is always assumed to be a crisp set A. For each $x \in X$, the value $\mu A(x)$ expresses the degree of membership of element x of X in the fuzzy set A. Each fuzzy membership function (*e.g.*, large, small, Gaussian, linear) varies with the equation and application while the choice is based on the option that best captures the transformation of the data based on the phenomenon being modeled. The fuzzy large function is used when input values are greater than the defined midpoint (assigned to an association of 0.5), which indicates a greater possibility of being members of the set and values below the midpoint with a decreasing membership (Fig. 6A). The fuzzy small function is the opposite. It is used when the smaller input values are more likely to be a member of the set. Values greater than the midpoint indicate a lower possibility of being a member of the set and values below the midpoint indicate a higher possibility of the membership (Fig. 6B). Fuzzification is the process of converting a crisp input value to a fuzzy value, and is conducted using the information in the knowledge base, while defuzzification is the return to the classic mathematical set (Zadeh, 1965; Zimmermann, 1985). The crisp input value can assume in classification the raw data (e.g., radioelement concentrations) or compressed digital image data (e.g., 8-bit), among other possibilities. These two input data approaches were analyzed in this study to compose the classification algorithms.

Boolean logic uses the Boolean operator '&' (AND), algebraic operator '+', and different weight combinations, for example, 1 for elevation and 4 for $\frac{eTh+eU}{K}$ (IOM). Thus, the different weights are arranged in a geometric progression of common ratio 4; $(A_n = 4^{n-1})$:$(1 * \text{elevation} + 4 * \frac{eTh+eU}{K})/5$ (Iza et al., 2016). These were the criteria applied to define weighting parameters of the variables, which allowed the best discrimination of lateritic duricrusts, mottled horizon, and soil areas. Fuzzy logic uses the fuzzy operators: Fuzzy Algebraic Product Operator (FAPO) to minimize the results, Fuzzy Algebraic Sum Operator (FASO) to maximize the results, and Fuzzy Gamma Operator (FGO) to balance the results. The FAPO tends to be very small with this operator due to

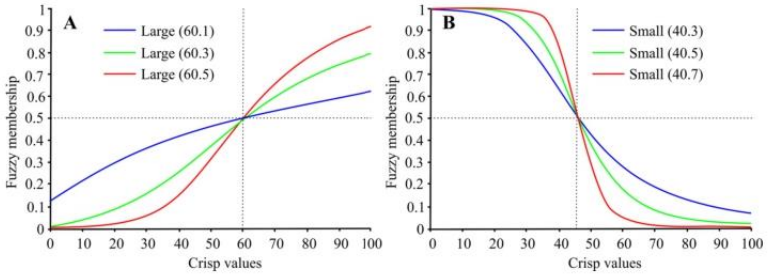

Fig. 6. Fuzzy membership functions. A - Fuzzy large function and B - Fuzzy small function.

multiplication of several numbers less than 1. The output is always smaller than, or equal to, the smallest contributing membership value, and is therefore "decreasive". In the FASO, the result is always larger than (or equal to) the largest contributing fuzzy membership value, and the effect is therefore "increasive". Two pieces of evidence, both favoring a hypothesis, reinforce each other and the combined evidence is more supportive than either piece of evidence taken individually. FGO is the combination of FAPO and FASO. Details regarding these operators can be found in Zadeh (1965), Zimmermann (1985), Bonham-Carter (1994), Klir (2004), Eddy et al. (2006), and Nykänen et al. (2008). Each operator generated a predictive map in the raster calculator and the results were compared to those from the fuzzy large pertinence function (fuzzification) in the GIS software. The fuzzy large function was used as the larger input values are more likely to be a member of the fuzzy set. In this study, the data were divided into five classes: extremely unfavorable, unfavorable, moderately favorable, favorable, and extremely favorable (Wilford, 2012; Iza et al., 2016). The first two classes were assigned to parent rock and saprolite, while the last two were assigned to lateritic duricrust and its dismantling products, and the moderately favorable class was assigned to the mottled horizon where lateritic duricrust fragments are not uncommon. The number of classes most appropriate for the study region was defined by observing the weathering stages of the field outcrops.

3.2. Algorithms validation

The efficiency of the predictive mapping results expressed by the kappa coefficient (κ), is defined as $\kappa = (p_0 - p_e)/(1 - p_e)$, where p_0 indicates the observed agreement, $p_e = [(n_1/n) * (m_1/n)] + [(n_0/n) * (m_0/n)]$ is the expected agreement, m_1 is total parent rock outcrops, m_0 is total duricrust outcrops, n_1 is total parent rock prediction, n_0 is total duricrust prediction, and n is total field outcrops. Table 1 schematically illustrates how kappa coefficient are calculated. Part of the observed agreement is attributed to chance, making it larger than the expected agreement ($p_0 > p_e$). Kappa is a measure of this difference, standardized to lie on a −1 to 1 scale. κ is intended to provide a quantitative measure of the magnitude of the agreement among the lithological information predicted by the model and its nature (e.g., parent rock or lateritic duricrust) confirmed in field outcrop (Cohen, 1960; Viera and Garrett, 2005). Kappa values between 1 and 0.81 indicate almost perfect agreement, between 0.80 and 0.61 indicate substantial, between 0.60 and 0.41 indicate moderate, and values closer to 0 indicate lower agreement (Landis and Koch, 1977). For this study, 1745 field outcrops were recorded, of which 1462 were assigned as parent rock (rock and saprolite) and 283 as lateritic duricrust (mottled horizon, soil and duricrust) in four possibilities: a) concordant lateritic duricrust; b) discordant lateritic duricrust; c) discordant parent rock; and d) concordant parent rock, which are the basis for determining κ. The supervised classification method was adopted in this study.

Table 1
Confusion matrix used to measure the agreement between field outcrops observations and predictive map (adapted from Cohen, 1960 and Viera and Garrett, 2005).

		Predictive map		
		Parent rock	Duricrust	Total
Field outcrops observations	Parent rock	A	B	m_1
	Duricrust	C	D	m_0
	Total	n_1	n_0	n

Note[1]. a = parent rock predicted as parent rock; b = parent rock predicted as duricrust; c = duricrust predicted as parent rock; d = duricrust predicted as duricrust; $n_1 = a + c$; $n_0 = b + d$; $m_1 = a + b$; $m_0 = c + d$; n = total field outcrops.

3.3. Multivariate linear regression

The gamma-ray spectrometric signature via multivariate linear regression is another way for mapping the regolith (Wilford, 2012; Iza et al., 2018) quicker than logic tools. To use this technique, the 1745 mapped sites were grouped in weathering classes (WCs) according to field observations in the study region: 1) unweathered, 2) slightly weathered, 3) moderately weathered, 4) highly weathered, and 5) extremely weathered (Table 2), where the last three classes included lateritic duricrust (mottled horizon, soil and duricrust). Statistical parameters (average, maximum, minimum, and standard deviation) and Pearson correlation coefficient (r) were calculated for elevation, eTh, eU, K, $\frac{eTh.eU}{K}$, and $\frac{eTh+eU}{K}$ for each of the five WCs (Table 2). The Pearson correlation coefficient intervals were classified as weak (0 to ± 0.29), moderate (±0.30 to ± 0.49), and strong (±0.50 to ± 1.00) according to Cohen (1988), and the multivariate regression was conducted according to the backward model stepwise regression of Wilford (2012). This approach identifies the independent variables that most influence the variability in the WC, the dependent variable. In the final step, the independent variables, eTh, eU, $\frac{eTh.eU}{K}$, $\frac{eTh+eU}{K}$, and elevation were used in the weathering intensity index (WII) equation and the map was compared to the Boolean and FAPO predictive maps.

4. Results

4.1. Exploratory data analysis

The total count image of gamma rays emitted by K, Th, and U reflected on the RGB space (Fig. 7A, B, and C), which when combined, resulted in the ternary map shown in Fig. 7D. The lateritic duricrusts occur along the greenish areas identified by high eTh and eU concentrations and low K content (Fig. 7D), especially in the manganese lateritic duricrust, relative to other rocks (Table 3). The central-northern, northwestern, and northeastern parts (whitish colors, Fig. 7D) have zones with high eTh (red to pink color, Fig. 7B) encompassed by high K (red to pink color, Fig. 7A). These zones mark the domain of metatonalites and metagranodiorites (Serra do Boqueirão Suite and TTG), saprolite and the rare lateritic duricrust outcrops

Table 2
Classification of the weathering level of the regolith adapted for the study region (Wilford, 2012; Iza et al., 2018).

Level (WC)	Weathering intensity	Descriptions
1	Unweathered	Rock without signs of decomposition, structure and preserved primary mineralogy. Rock outcrops predominate over soils (>70%). Surface soils when present are Gleysols.
2	Slightly weathered	Rock slightly discolored with eventual staining. The overall fabric of the rock is well preserved, and outcrop are common. Primary minerals are largely preserved; however, feldspars can be slightly weathered. Surface soils are typically Cambisols.
3	Moderately weathered	Residual sands and clays are common in the upper part of the weathering profile. Rock partially weathered but still cohesive. Most of the feldspars are weathered. Profile commonly mottled. Lateritic duricrusts are not uncommon. Surface soils are typically Plinthosols. Absence of a layer of accumulated clay, humus or soluble salts.
4	Highly weathered	Residual sands and clays are common in the upper part of the weathering profile. Profile commonly mottled with the primary bedrock structure typically lost. Saprolite soft and weakly cohesive that can be broken by hand. The mineral content is dominated by clays, oxi-hidroxides of iron and aluminum with or without residual quartz and anatase. Other minerals in low abundance or absent. Blocks and slabs of lateritic duricrusts, lateritic gravels, Acrisols and Ferralsols dominate rock outcrops (>80%).
5	Extremely weathered	Residual sands and clays are common in the upper part of the weathering profile; mottling and leaching are intense and frequent. Saprolite is soft with primary minerals completely weathered to form clays or oxi-hydroxides. However, resistant quartz veins may still remain together with the anatase as the only remaining primary minerals. Blocks and slabs of lateritic duricrust, lateritic gravels, Acrisols and Ferralsols are dominates (>95%). Practically no parent rock appears.

(Fig. 1). The darker areas (Fig. 7D) are characterized by low eTh and eU (cyan, Fig. 7B and C), whereas the reddish colors correspond to parts of the TTG domain (Fig. 1). In some of these sites in the midwestern region, the existing lateritic duricrusts (Fig. 7D) did not show a tendency to concentrate Th and U.

The preliminary analysis illustrated the gamma-ray spectrometry signature of the study region. Thereafter, several combinations of data variables were used in the predictive mapping experiments, along with data transformations (with or without previous data reclassification, raw, and 8-bit image) and modeling methods (Boolean, Fuzzy, and multivariate regression). The individual Th channel, and the $\frac{eTh.eU}{K}$ and $\frac{eTh+eU}{K}$ ratios were used to highlight the signature of the lateritic duricrust (high eTh and eU relative to K values) (Wilford et al., 1997; Carrino et al., 2011; Iza et al., 2016). The Pearson correlation coefficient of $\frac{eTh+eU}{K}$ relative eTh and eU in the lateritic duricrusts (0.74 and 0.58, respectively) was slight higher than the coefficients in the bedrock and saprolite (0.60 and 0.53, respectively), highlighting the suitability of $\frac{eTh+eU}{K}$ ratio for mapping regoliths (Fig. 8). The average $\frac{eTh+eU}{K}$ in the lateritic duricrusts (9.05) was higher than that in the parent rock and saprolite (6.07). The Pearson correlation coefficient of $\frac{eTh.eU}{K}$ relative to eTh and eU in the lateritic duricrusts (0.83 and 0.76, respectively) was similar to the coefficients for bedrock and saprolite (0.81 and 0.75, respectively). The average $\frac{eTh.eU}{K}$ in the lateritic duricrust (19.6) was also higher than that in the parent rock and saprolite (11.17) (Fig. 8).

4.2. Boolean and fuzzy logic

Several combinations of airborne gamma-ray were tested. Fig. 5 shows the flowchart with the four algorithms applied to data to obtain the regolith predictive maps for the study area (Table 4): algorithm 1 - eTh exported from GIS software as an 8-bit image (256 Gy levels) processed with elevation (8-bit) using the Boolean (AND) and fuzzy operators (FAPO, FASO, and FGO); algorithm 2 - $\frac{eTh.eU}{K}$ processed with elevation and exported according to algorithm 1; algorithm 3 - $\frac{eTh+eU}{K}$ exported in the same format as that of algorithm 1 and elevation, applying the Boolean IOM and different weights (1 for elevation and 4 for $\frac{eTh+eU}{K}$) (Bonham-Carter, 1994), and applying the fuzzy method (Zadeh, 1965) to these variables; and algorithm 4 - the same variables as of algorithm 3, but used the raw data (not compressed digital image) including elevation, and exported from GIS software with the appropriate extension (.flt) to maintain the original data in concentration, and then applying the Boolean IOM and fuzzy (see Figs. 9 and 10, respectively) methods.

In each algorithm, the topographic altitudes of the lateritic duricrust (348–488 m), defined by the SRTM images and fieldwork, were used in the raster calculator to generate a Boolean predictive map of elevation by applying the AND operator in the expression [elevation $\geq (\overline{X} - \sigma)$] AND [elevation $\leq (\overline{X} + 3/2\ \sigma)$] for both raw elevation data and compressed digital image data, where $\overline{X}$ is the average and σ the standard deviation (Table 5). The Boolean predictive maps of airborne gamma-ray data were prepared using the expressions: [eTh $\geq (\overline{X} + 1/3\ \sigma)$] (algorithm 1); [$\frac{eTh.eU}{K} \geq (\overline{X} + 1/3\ \sigma)$] (algorithm 2); [$\frac{eTh+eU}{K} \geq (\overline{X} + 1/3\ \sigma)$] (algorithm 3); and [$\frac{eTh+eU}{K} \geq \overline{X}$] (algorithm 4, Table 5).

The combinations of airborne gamma-ray and altimetric data using algebraic operators (−, +, ≥, and ≤) and Boolean logic (AND) resulted in Boolean predictive maps that highlighted the areas favorable and non-favorable for lateritic duricrusts (Fig. 9). The elevation increased the accuracy (91%) and κ (0.69) of the Boolean prediction (algorithm 4) relative to $\frac{eTh+eU}{K}$ (accuracy 87%; κ = 0.56). The fuzzification of the FAPO, FASO, and FGO formulas (Table 4) yielded fuzzified maps (Fig. 10). The five classes in the fuzzy predictive maps (extremely unfavorable, unfavorable, moderately favorable, favorable, and extremely favorable) were based on their histograms and field outcrops observations. The classes with lower values (extremely unfavorable and unfavorable) corresponded to areas of parent rock and saprolite, whereas classes with the three highest values (moderately favorable, favorable and extremely favorable) corresponded to areas of mottled horizon, soil and lateritic duricrust (Wilford, 2012; Iza et al., 2016). The maps that best predicted (Fig. 11) the lateritic duricrusts relative to the parent rocks and saprolites, were the Boolean and FAPO prepared under algorithm 4 (Fig. 11A and B, respectively) using $\frac{eTh+eU}{K}$ and the raw data (Figs. 9 and 10, respectively). Similar to elevation, eU cannot be disregarded in the predictive mapping for the study region. It combined in $\frac{eTh+eU}{K}$ improves the results (accuracy 90%; $\kappa_{FAPO} = 0.66$) in relation to eTh/K single ratio (accuracy 86%; $\kappa_{FAPO} = 0.50$).

4.3. Weathering intensity index

The Pearson correlation coefficient showed that the correlations between the elevation, eTh, eU, K, and $\frac{eTh+eU}{K}$ (Table 6) and the five WCs were strong for eTh (r = 0.58, Table 7), eU (r = 0.52), and $\frac{eTh+eU}{K}$ (r = 0.76), and weak for elevation (r = 0.18) and K (r = −0.12), as per the classification by Cohen (1988) (Table 7). Although the correlation coefficient between elevation and WC was weak, the kappa coefficient (0.58) and field outcrops observations indicated that elevation is an important factor for regolith mapping in the study region (Table 4).

The parameters Th, $\frac{eTh+eU}{K}$, and elevation explained 62.4% of WC variability with the correlation intensity of r = 0.79 (Table 8). These

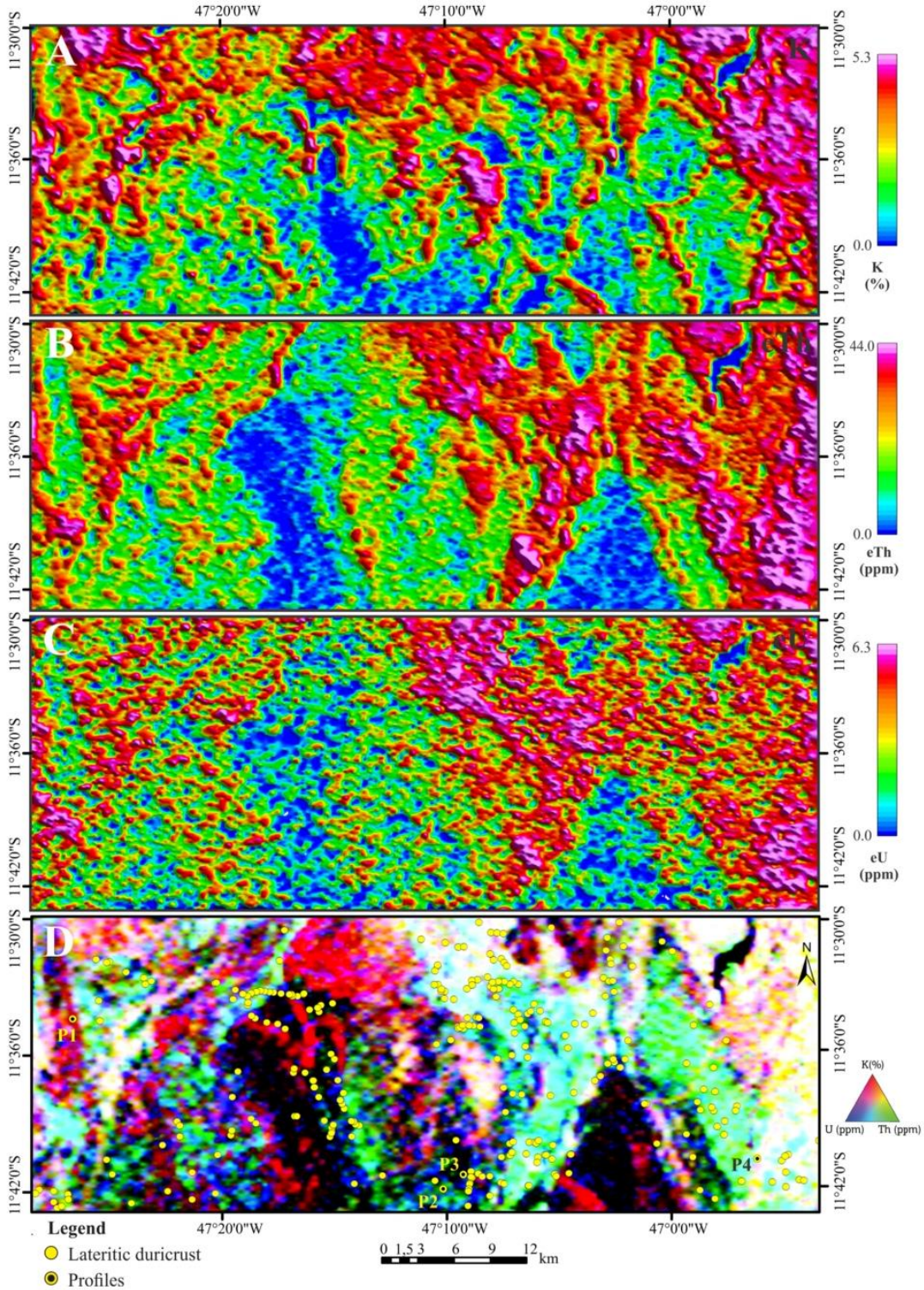

Fig. 7. Airborne radio-element grids of the individual channels and RGB ternary composition of gamma-ray spectrometric data (K, eTh, and eU).

Table 3
Average chemical composition of the lateritic duricrust and rocks, K in % and Th and U in ppm. Estimates of uranium and thorium concentrations are reported as uranium equivalent (eU) and thorium equivalent (eTh).

Average	Chemical composition			Gamma-ray spectrometry		
	K	Th	U	K	eTh	eU
Ferruginous lateritic duricrust	0.2	6.8	2.1	1.3	8.9	2.4
Manganese lateritic duricrust	0.2	12.7	4.1	1.8	28.8	4.6
Parent rock	0.7	2.6	0.5	1.7	8.0	2.2

variables when integrated by multivariate linear regression resulted in a global p-value of 0.00 for the F test (<0.05). This implies that at least one of the variables was correlated with WCs (Table 8). Despite the strong correlation of WC with eU (r = 0.52), eU had a p-value of 0.36 for the F test (>0.05) in multivariate linear regression. This indicated multicollinearity between eU and other variables (Th, $\frac{eTh+eU}{K}$, and elevation) and eU was not used for calculating WII. All three statistically significant (individual p-values < 0.05) variables (Th, $\frac{eTh+eU}{K}$, and elevation) in the multivariate linear regression were used to generate the WII equation (Equation (1)) and the predictive regolith map for the study region (Fig. 12).

$$WII = -1.2810 + 0.0034*elevation + 0.0310*eTh + 0.2327*\frac{eTh+eU}{K} \quad (1)$$

The duricrust lateritic areas are underestimated when they are used in the WII map and in the FAPO map's four classes (unfavorable, moderately favorable, favorable, and extremely favorable) instead of five classes (extremely unfavorable, unfavorable, moderately favorable, favorable, and extremely favorable). The kappa coefficient decreased from 0.66 to 0.52 as many parent rock outcrops were classified in FAPO as lateritic duricrust.

5. Discussion

Algorithms with different combinations of variables were tested. The degree of rocks alteration in 1745 field outcrops; the parent rocks and lateritic radioelements signatures proposed in the literature, in addition to other possibilities; and the kappa coefficient were the criteria adopted to determine the efficiency of the predictive mapping results. The algorithm 4: ($\frac{eTh+eU}{K}$ exported with appropriate extension to maintain the original data in concentration and elevation with $\kappa_{Boolean} = 0.69$ and $\kappa_{FAPO} = 0.66$) was found to has be the most accurate mathematical approach (substantial efficiency; accuracy 91%) for regolith mapping (Table 4 and Fig. 11). This indicates that despite the great variety of rocks covered by sparse shrubs, it was possible to identify the spreading lateritic duricrusts (mottled horizon, soil and duricrust) that covers almost 30% of the total area (Table 4 and Fig. 11). This area is larger than the areas delimited by previous geological mappings (CPRM, 2014; Campos et al., 2016, Fig. 1). Although the low eU concentration ($\bar{X} = 2.2$ ppm, Table 6) when it is combined in $\frac{eTh+eU}{K}$ algorithm (4) it improves the accuracy to 90% and the κ_{FAPO} to 0.66) relative to eTh/K (accuracy 86%; $\kappa_{FAPO} = 0.50$). The altitude range (348–488 m) is an important variable for of the lateritic duricrusts identification, as indicated Iza et al. (2018). In the study area it improves the accuracy (91%) and $\kappa_{Boolean}$ (0.69) of predictive maps to relative to those generated by algorithms using only $\frac{eTh+eU}{K}$ (accuracy 87%; $\kappa_{Boolean} = 0.56$), and therefore their quality.

The weak to moderate efficiency ($\kappa \leq 0.48$) and low accuracy (≤79%) of algorithms 1, 2, and 3 to identify the lateritic duricrusts (Table 4) resulted in a three-fold increase in the number of discordant parent rocks (parent rock and saprolite) of the model (parent rock predicted as duricrust). Further, algorithm 2 ($\kappa_{FGO} = 0.10$), that used the $\frac{eTh.eU}{K}$ ratio, was less efficient than algorithm 3 ($\kappa_{FGO} = 0.34$) that used the $\frac{eTh+eU}{K}$ ratio. The integration of raw data of $\frac{eTh.eU}{K}$ and elevation was also tested. Although the average $\frac{eTh.eU}{K}$ (19.6) in lateritic duricrusts was greater than average $\frac{eTh+eU}{K}$ (9.05), the predictive maps had moderate efficiency ($\kappa_{Boolean} = 0.55$ and $\kappa_{FAPO} = 0.43$) due to excessive restriction of the lateritic duricrust areas. The $\frac{eTh+eU}{K}$ ratio most accurately predicted areas with lateritic duricrusts.

The mathematical logic (Fig. 11) and multivariate linear regression (Fig. 12) showed the efficiency of the airborne gamma-ray spectrometry in mapping regoliths in the Midwest Brazil. The Boolean (91%) and FAPO (90%) are excellent predictive techniques and were marginally more accurate than multivariate regression WII techniques (88%) for the

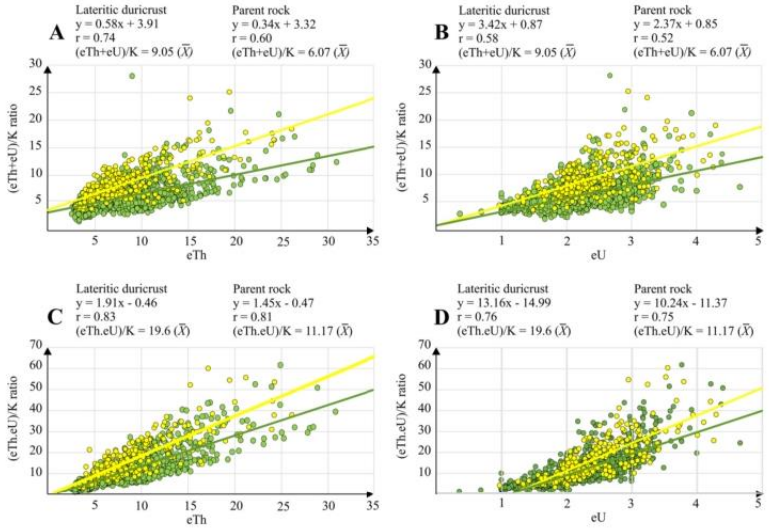

Fig. 8. Plots of gamma-ray spectrometric signatures of lateritic duricrust (yellow dots) relative to those of parent rock (green dots): A – (eTh + eU)/K vs. eTh; B - (eTh + eU)/K vs. eU; C - (eTh.eU)/K vs. eTh; and D - (eTh.eU)/K vs. eU. K (%), Th (ppm), U (ppm).

Table 4
Results of the predictive maps for favorable and extremely favorable areas to the occurrence of lateritic duricrusts using different variables and processing flows. The algorithm used in Boolean and fuzzy predictions maps (4) have the best accuracy and kappa coefficient (κ).

	Input	Logic	Formulas and data type	Confusion matrix*	Accuracy (%)	κ	Area (%)**
Compressed digital image data (0–255)							
1	Elevation (SRTM)	Boolean	Elevation AND eTh	(935-527-66-217)	66	0.25	44.8
		FAPO	Elevation*eTh	(768-694-51-232)	57	0.18	56.0
	eTh	FASO	(1-(1-Elevation)*(1- eTh))	(814-648-52-231)	60	0.20	54.4
		FGO	Power ((FASO),0.7)*Power ((FAPO),0.3)	(501-961-10-273)	44	0.13	74.2
Compressed digital image data (0–255)							
2	Elevation (SRTM)	Boolean	Elevation AND $\frac{eTh \cdot eU}{K}$	(1083-379-29-254)	77	0.43	42.4
		FAPO	Elevation* $\frac{eTh \cdot eU}{K}$	(1003-459-19-264)	73	0.38	59.6
	$\frac{eTh \cdot eU}{K}$	FASO	(1-(1-Elevation)*(1- $\frac{eTh \cdot eU}{K}$))	(971-491-20-263)	71	0.36	56.4
		FGO	Power ((FASO),0.7)*Power ((FAPO),0.3)	(403-1059-4-279)	39	0.10	82.6
Compressed digital image data (0–255)							
3	Elevation (SRTM)	Boolean (IOM)	(1*Elevation)+(4*($\frac{eTh + eU}{K}$))/5	(1124-338-20-263)	79	0.48	49.3
		FAPO	Elevation* $\frac{eTh + eU}{K}$)	(959-503-12-271)	70	0.36	59.8
	$\frac{eTh + eU}{K}$	FASO	(1-(1-Elevation)*(1- $\frac{eTh + eU}{K}$))	(962-500-39-244)	69	0.31	57.8
		FGO	Power ((FASO),0.7)*Power ((FAPO),0.3)	(986-476-34-249)	71	0.34	59.0
Raw data (in concentration and meter)							
4	Elevation (SRTM)	Boolean (IOM)	(1*Elevation)+(4*($\frac{eTh + eU}{K}$))/5	(1352-110-51-232)	91	0.69	30.4
		FAPO	Elevation* $\frac{eTh + eU}{K}$	(1366-96-73-210)	90	0.66	28.5
	$\frac{eTh + eU}{K}$	FASO	(1-(1-Elevation)*(1- $\frac{eTh + eU}{K}$))	(1364-98-73-210)	90	0.65	29.2
		FGO	Power ((FASO),0.7)*Power ((FAPO),0.3)	(1362-100-74-209)	90	0.65	29.9

Note[2]. * Respective values for parent rock predicted as parent rock, parent rock predicted as duricrust, duricrust predicted as parent rock and duricrust predicted as duricrust.
**Area covered by lateritic materials (lateritic duricrust, mottled horizon and soil).
FAPO - Fuzzy Algebraic Product Operator, FASO - Fuzzy Algebraic Sum Operator, FGO - Operator Gamma Fuzzy.

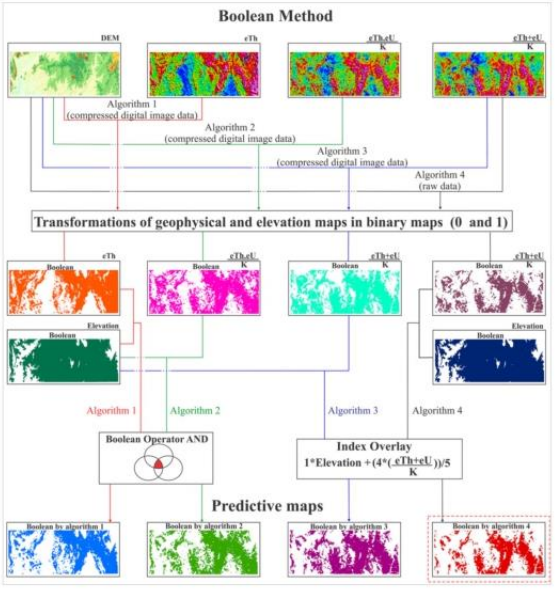

Fig. 9. Flowchart of the algorithms for generating Boolean predictive maps.

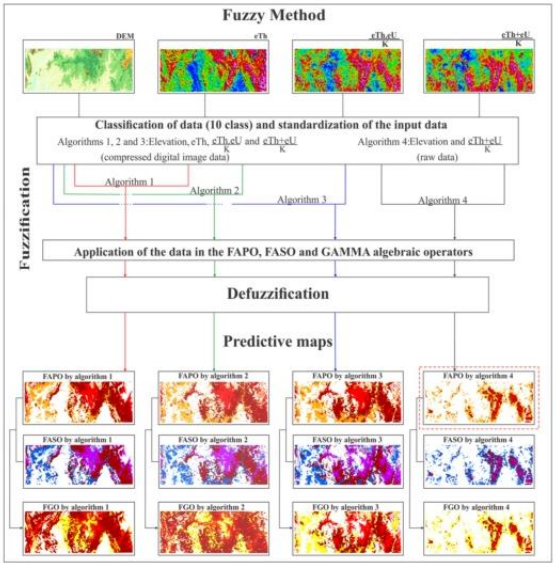

Fig. 10. Flowchart of the algorithms for generating fuzzy predictive maps.

study region (Figs. 11 and 12). However, calculating WII is faster as it requires less mathematical processing and is simpler to work with as it uses basic statistical methods. Thus, the techniques used to prepare regolith maps suitable to discriminate areas of parent rock and saprolite from areas with lateritic duricrusts can help as a guide in the prospecting

Table 5

Statistical summary of eTh$\frac{eTh.eU}{K}$, $\frac{eTh+eU}{K}$ and elevation for the algorithms 1, 2, 3, 4.

Algorithms	Variables	Min	Max	Average ($\bar{X}$)	Standard deviation (σ)
1 *	eTh	0.0	255.0	152.9	97.8
2 *	$\frac{eTh.eU}{K}$	0.0	255.0	154.9	97.4
3 *	$\frac{eTh+eU}{K}$	0.0	255.0	154.7	97.5
(1, 2, 3) *	Elevation	0.0	255.0	46.9	26.7
4 ** *	$\frac{eTh+eU}{K}$	1.0	111.6	7.0	3.5
4 ** *	Elevation	314.0	772.0	404.0	51.5

Note[3]. * Compressed digital image data (0–255). * * Raw data: eTh (ppm), eU (ppm), K (%), elevation (m).

of new targets for mineral exploration in the region.

The combined use of a wide range of data layers (*e.g.*, lateritic index - LI, WII, digital elevation model - DEM, and geochemical map) is now a standard method of automated routines for visualizing the spatial distribution of regolith and landforms in Australia and other countries (Carranza et al., 1999; Wilford, 2012; Metelka et al., 2018). More informative maps can be created as layers in the GIS software and can help with the planning of further geochemical investigations and construction of complex thematic maps (Craig, 2001). There are several combinations of airborne gamma-ray data: eTh/K, eU/K (Iza et al., 2016), and LI ($\frac{eTh.eU}{K^2}$) (Iza et al., 2018). However, they underestimate or overestimate the predicted areas for lateritic duricrusts. The size of the lateritic duricrust outcrops also affects the efficiency of airborne

Table 6

Basic statistics of altimetric and airborne gamma-ray data at observed sites (algorithm 4, raw data).

	N	Minimum	Maximum	Average ($\bar{X}$)	Standard deviation (σ)
Elevation (m)	1745	320	637	410.2	46.6
eTh (ppm)	1745	2.5	30.9	8.2	4.0
eU (ppm)	1745	0.4	4.7	2.2	0.5
K (%)	1745	1.0	4.0	1.7	0.6
$\frac{eTh+eU}{K}$	1745	1.6	28.0	6.6	2.8

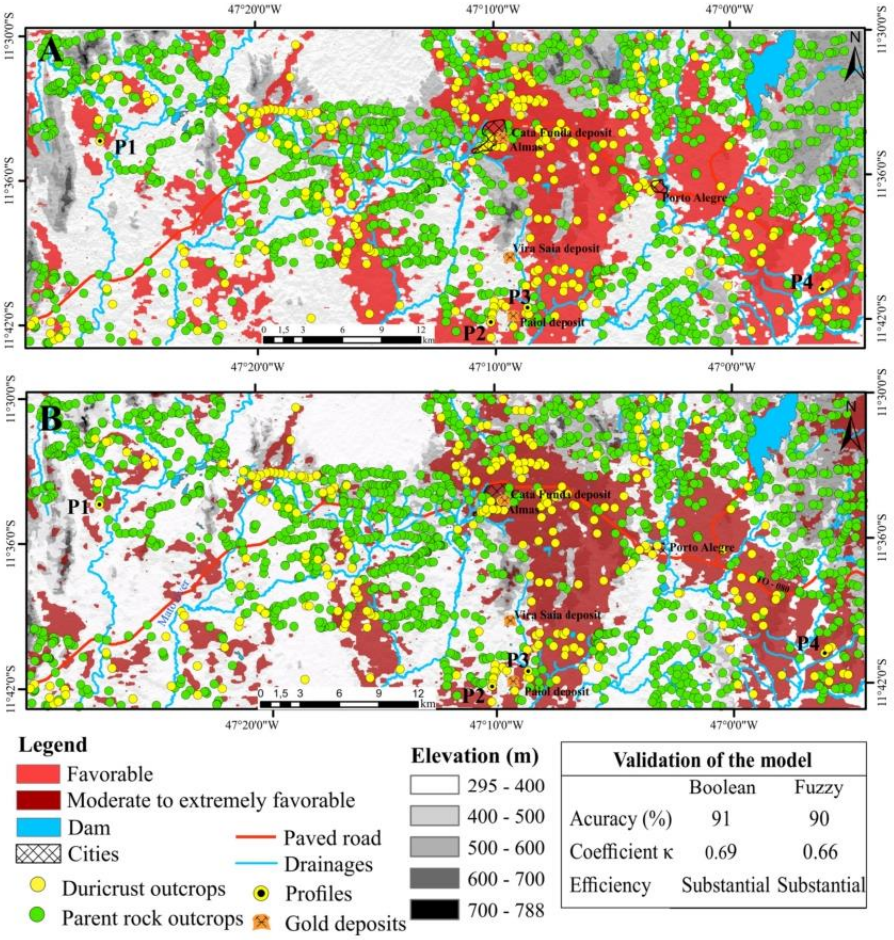

Fig. 11. Predictive maps of lateritic duricrust occurrence using Boolean (A) and fuzzy (B) logics (algorithm 4). Areas in red are lateritic duricrusts, mottled horizon, and soil, whereas the remaining area consists of parent rock and saprolite.

Table 7
Pearson correlation coefficient (r) results.

	WC	Elevation*	eTh	eU	K	$\frac{eTh + eU}{K}$
WC	1.00	**0.18**	**0.58**	**0.52**	−0.12	**0.76**
Elevation		1.00	0.31	0.23	0.49	−0.04
eTh			1.00	0.81	0.51	0.58
eU				1.00	0.41	0.53
K					1.00	−0.26
$\frac{eTh + eU}{K}$						1.00

Note[4]. (1) WC = weathering class described in Table 2. SRTM* = Shuttle Radar Topography Mission; (2) Bold values were referenced in the text.

Table 8
Summary of stepwise regression.

Regression statistic			
r multiple	0.790		
r^2	**0.624**		
r^2 adjusted	**0.623**		
Standard error	0.585		
Global p-value of F test	**0.000**		
	Coefficients	Standard error	Individual p-value
Intersection	**−1.2810**	0.1366	2.1332×10^{-20}
Elevation	**0.0034**	0.0003	9.5602×10^{-25}
eTh	**0.0310**	0.0066	5.5578×10^{-11}
$\frac{eTh + eU}{K}$	**0.2327**	0.0064	3.3357×10^{-210}

gamma-ray spectrometry to map the regolith in the midwestern part of the study site, where there is lateritic duricrust in small outcrops (less than 50 m in diameter) and therefore they are difficult to identify using the methods presented above (Fig. 7D, yellow dots in dark zones in the midwestern region). The choice of the optimal number of classes that represent the materials that make up the regolith strongly influences the quality of the predictive map, and must be adapted to the environmental context of the study region (Wilford, 2012; Iza et al., 2018). For the study region, tests showed that five classes for the WII map produced a satisfactory result (accuracy 88%), as show in Fig. 12.

Despite the possibility of gamma-ray attenuation by vegetation (Wilford, 1997), the manganese lateritic duricrust on gabbro (Serra do Boqueirão Suite) (Fig. 1, profile 4) in the dense vegetation covers in the southeastern part of the study region was highlighted by Boolean and fuzzy (FAPO) logics and WII. This was a consequence of the manganese duricrust having higher eTh (28.8 ppm) and eU (4.6 ppm) than the ferruginous lateritic duricrusts (8.9 and 2.4 ppm, respectively), which was validated by chemical analysis which showed higher concentrations of Th and U (12.7 and 4.1 ppm, respectively) in the manganese duricrust than in the ferruginous duricrust (6.8 and 2.1 ppm, respectively), as shown in Table 3. A recent study in southwestern Amazonia provided similar findings (Albuquerque et al., 2020). Thus, the gamma-ray spectrometry algorithms were found to be suitable also for mapping manganese lateritic duricrusts.

The misinformation about data input is an issue in the application of Boolean and fuzzy logic mapping techniques. When normalized data (256 Gy levels; K, eTh, eU, and their ratios) are used, the lateritic duricrust areas may be overestimated, as shown in algorithms 1, 2, and 3. The assigning of weights to the variables (IOM) instead of using the AND operator can provide better Boolean and fuzzy predictive maps. Considering that the airborne gamma-ray spectrometry data were acquired along a series of approximately parallel survey lines, and then it was interpolated using minimum curvature algorithm into a regular grid network, it is expected that noise, effects of data density and from the interpolation are smoothed (Dentith and Mudge, 2014). Therefore, it is necessary to test several combinations as well as input data formats validated by fieldwork and geological and geomorphological support to identify the most accurate results for a given region.

There are some limitations to the interpretation of gamma-ray spectrometry data associated with the algorithms and mapping techniques. The most obvious limitation is that regolith materials do not have unique gamma-ray signature, therefore gamma-ray data for regolith mapping is best used together with other datasets including multispectral, geochemistry, and altimetric data. Multispectral data can be used to create images showing the distribution of clays and iron oxides, both of which influence the distribution of K, Th and U (Dauth, 1997;

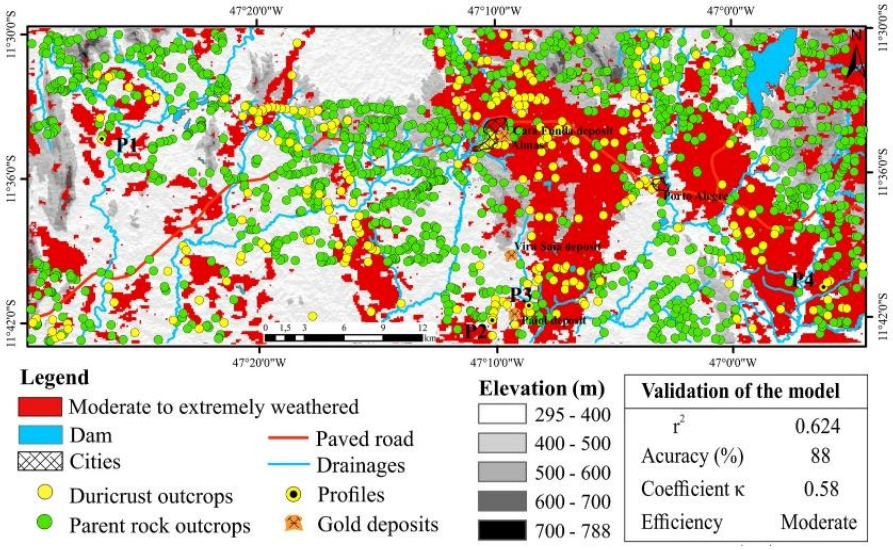

Fig. 12. The WII map overlaid on the shaded altimetry, highlighting moderate to intensely weathered areas. Areas in red are moderate to extremely weathered (lateritic duricrusts, mottled horizon, and soil), as predicted by the WII equation, whereas the remaining areas represent unweathered to slightly weathered areas (parent rock and saprolite).

Metelka et al., 2018). The dense vegetation cover may limit the application of gamma-ray spectrometry. The optical remote sensing is routinely employed in regolith mapping (Souza et al., 2021), including band ratios and principal component analysis. These techniques enhance the response of clay minerals and suppress the effects of vegetation (Crósta and Moore, 1989). Another limitation of the described techniques is that airborne gamma-ray acquisition systems have relatively large "footprints''. This results in poor spatial resolution for local-scale applications (Wilford and Minty, 2007).

6. Conclusions

The efficiency of airborne gamma-ray spectrometry and elevation (SRTM image) in predicting residual lateritic duricrust areas, including mottled horizon and soil, relative to saprolite and parent rock outcrops in tropical terrains was highlighted using map algebra. The algorithm that used $\frac{eTh+eU}{K}$ (in concentration) and elevation exported with appropriate extension to maintain the original data as airborne concentrations (algorithm 4) was the most efficient, with 91% accuracy, as compared to the other three algorithms (eTh in algorithm 1, $\frac{eTh.eU}{K}$ in algorithm 2, and $\frac{eTh+eU}{K}$ in algorithm 3, exported from GIS software as a compressed digital image data integrated with elevation using the Boolean and fuzzy operators).

The classification of WC, eTh, eU, $\frac{eTh+eU}{K}$, and elevation using Pearson correlation coefficient and multivariate linear regression for WII also yielded accurate predictive maps of regolith. Thus, integration of multisource data resulted in efficient mapping algorithms for the regolith in the study region. These algorithms help provide new guidelines and strategies for rapid selection of target sites for regolith exploration and have large applicability in regional geochemical interpretation and geological map reinterpretation.

The predictive mapping tools used in this study (e.g., weathering intensity index) allowed to discriminate areas in different degrees of weathering. The successful application of this technique for mapping regoliths is due to the effects of weathering, where radioelements contained in the rock are released, redistributed, and incorporated into the weathering products, modifying the gamma-spectrometric pattern of the underlying primary rocks. This approach is the key concept to design the algorithms used in this study.

Credit author statement

Author 1: prepared the manuscript. Author 2: supervised all stages of preparing the manuscript. Participated in fieldwork, discussed the data, and revised the manuscript. Author 3: helped in the implementation of Boolean and fuzzy logics. Author 4: helped collect and prepare samples for mineral and chemical composition. Author 5: helped process airborne gamma-ray data. Author 6: contributed to the discussion of data and revision of the manuscript.

Declaration of competing interest

The authors declare that they have no known competing financial interests or personal relationships that could have appeared to influence the work reported in this paper.

Acknowledgments

The authors thank Serviço Geológico do Brasil - CPRM for providing the aerogeophysical data (http://geosgb.cprm.gov.br/), Universidade de Brasília and CAPES (Coordenação de Aperfeiçoamento de Pessoal de Nível Superior) for the technical and physical support, Instituto Natureza do Tocantins (NATURATINS/Governo do Estado do Tocantins) and Conselho Nacional de Desenvolvimento Científico e Tecnológico (CNPq) for financial support (grant n° 302618/2016-3) and to the reviewers and editor for their valuable criticisms and suggestions.

References

Albuquerque, M.F.S., Horbe, A.M.C., Soares, T.M., Sousa, E.M.D., Iza, E.R.H.F., 2020. Airborne radiometric data for identifying lateritic surface in southwestern Amazonia, Brazil. J. Appl. Geophys. 175, 103989. https://doi.org/10.1016/j.jappgeo.2020.103989.

Anand, R.R., 2001. Evolution, classification and use of ferruginous materials in gold exploration, Yilgarn craton, Western Australia. Geochem. Explor. Environ. Anal. 1, 221–236. https://doi.org/10.1144/geochem.1.3.221.

Anand, R.R., Butt, C.R.M., 2010. A guide for mineral exploration through the regolith in the Yilgarn Craton, western Australia. Aust. J. Earth Sci. 57, 1015–1114. https://doi.org/10.1080/08120099.2010.522823.

Anand, R.R., Paine, M., 2002. Regolith geology of the yilgarn craton, western Australia: implications for exploration. Aust. J. Earth Sci. 49, 3–162. https://doi.org/10.1046/j.1440-0952.2002.00912.x.

Arhin, E., Jenkin, G.R.T., Cunningham, D., Nude, P., 2015. Regolith mapping of deeply weathered terrain in savannah regions of the Birimian Lawra Greenstone Belt, Ghana. J. Geochem. Explor. 159, 194–207. https://doi.org/10.1016/j.gexplo.2015.09.008.

Barbosa, I.O., Pires, A.C.B., Lacerda, M.P.C., Carmelo, A.C., 2013. Geology, airborne geophysics, geomorphology and soils in the individualization of the niquelândia mafic-ultramafic complex, Goiás state, Brazil. Rev. Bras. Geofís. 31, 463–481. https://doi.org/10.22564/rbgf.v31i3.316.

Barnes, S.J., Fisher, L.A., Anand, R., Uemoto, T., 2014. Mapping bedrock lithologies through in situ regolith using retained element ratios: a case study from the Agnew-Lawlers area, Western Australia. Aust. J. Earth Sci. 61, 269–285. https://doi.org/10.1080/08120099.2014.862302.

Bonham-Carter, G., 1994. Geographic Information Systems for Geoscientists: Modelling with GIS. Pergamon, Oxford.

Borges, M., 1993. Evolução tectono-estrutural da região de Dianópolis-Almas, SE do Estado do Tocantins. Tese (doutorado em geologia). Universidade Federal do Pará, Belém, Brasil, p. 365p.

Bowell, R.J., Afreh, E.O., Laffoley, N. d'A., Hanssen, E., Abe, S., Yao, R.K., Pohl, D., 1996. Geochemical exploration for gold in tropical soils — four contrasting case studies from West Africa. Institution of Mining and Metallurgy Transactions 105, B12–B33.

Campos, D.S. de, Toledo, C.L.B., Carvalho, M.J. de, Rodrigues, V.G., Araujo, K., Silva, A. M., 2017. Prospectivity analysis of gold and iron oxide copper-gold-(silver) mineralizations from the Faina Greenstone Belt, Brazil, using multiple data sets. Brazilian J. Geol. 47, 561–590. https://doi.org/10.1590/2317-4889201720170012.

Campos, J.E.G., et al., 2016. Mapa base integrado. Projeto Almas 2016. Escala 1:50.000 [Trabalho final de graduação]. Universidade de Brasília, Curso de Geologia, Instituto de Geociências.

Carranza, E.J.M., 2011. Geocomputation of mineral exploration targets. Comput. Geosci. 37, 1907–1916.

Carranza, E.J.M., Mangaoang, J.C., Hale, M., 1999. Application of mineral exploration models and GIS to generate mineral potential maps as input for optimum land-use planning in the Philippines. Nat. Resour. Res. 8, 165–173. https://doi.org/10.1023/A:1021846820568.

Carrino, T.A., Silva, A.M., Botelho, N.F., da Silva, A.A.C., 2011. Discriminação de áreas de espesso regolito do leste do estado do Amazonas usando estatística multivariada, algoritmo hiperespectral e modelagem de dados espaciais. Rev. Bras. Geofís. 29, 155–172. https://doi.org/10.1590/S0102-261X2011000100011.

Cohen, J., 1960. A coefficient of agreement for nominal scales. Educ. Psychol. Meas. 20, 37–46. https://doi.org/10.1177/001316446002000104.

Cohen, J., 1988. Statistical Power Analysis for the Behavioral Sciences, second ed. Erlbaum, Hillsdale, NJ. https://doi.org/10.4324/9780203771587.

Corrêa, R.S., Oliveira, C.G., Vidotti, R.M., Souza, V.S., 2015. Regional-scale pressure shadow-controlled mineralization in the príncipe orogenic gold deposit, Central Brazil. Ore Geol. Rev. 71, 273–304.

Costa, J.B.S., 1985. Aspectos lito-estruturais e evolução crustal da região centro-oeste de Goiás. Universidade Federal do Pará.

Costa, M.L., 1997. Lateritization as a major process of ore deposit formation in the amazon region. Explor. Min. Geol. 6, 79–104.

CPRM - Serviço Geológico do Brasil, 2014. Carta geológica. Projeto sudeste do Tocantins. Folha SC.23-Y-C - dianópolis. In: Sabóia, A.M., Maneghini, P.F.V. (Eds.), Gonçalves, F.G. (org.). Escala 1:250.000.

CPRM - Serviço Geológico do Brasil, 2006. Projeto Aerogeofísico do Tocantins, Relatório Final do Levantamento e processamento de dados magnetométricos e gamaespectrométricos. Available at: http://geosgb.cprm.gov.br/. (Accessed 25 November 2017).

Craig, M.A., 2001. Regolith mapping for geochemical exploration in the Yilgarn craton, Western Australia. Geochem. Explor. Environ. Anal. 1, 383–390.

Crósta, A.P., Moore, J.M., 1989. Enhancement of Landsat Thematic Mapper imagery for residual soil mapping in SW Minas Gerais state Brazil: a prospecting case history in Greenstone belt terrain. Proc. 7th Themat. Conf. Remote Sens. Explor. Geol. Calgary 1173–1187.

Cruz, E.L.C.C., Kuyumjian, R.M., 1998. Geology and tectonic evolution of the Tocantins granito-greenstone terrane: Almas-Dianópolis region, Tocantins State, central Brasil. Rev. Bras. Geociencias 28, 173–182.

Cruz, E.L.C.C., Kuyumjian, R.M., 1999. Mineralizações auríferas filoneanas do terreno granito-greenstone do Tocantins. Rev. Bras. Geociencias 29, 291–298.

Cruz, E.L.C.C., Kuyumjian, R.M., 2006. Geochronology, isotopic signature and metallogenetic model for the Córrego Paiol gold deposit, Tocantins state, central Brazil. Rev. Bras. Geociencias 36 (1-Suplemento), 152–156.
Dauth, C., 1997. Airborne magnetic, radiometric and satellite imagery for regolith mapping in the Yilgarn Craton of Western Australia. Explor. Geophys. 28, 199–203. https://doi.org/10.1071/EG997199.
Davy, R., El-Ansary, M., 1986. Geochemical Patterns in the laterite profile at the boddington gold deposit, western Australia. J. Geochem. Explor. 26, 119–144. https://doi.org/10.1016/0375-6742(86)90062-2.
Dent, D.L., MacMillan, R.A., Mayr, T.L., Chapman, W.K., Berch, S.M., 2013. Use of airborne gamma radiometrics to infer soil properties for a forested area in British Columbia, Canada. J. Ecosyst. Manag. 14, 1–12.
Dentith, M., Mudge, S., 2014. Geophysics for the Mineral Exploration Geoscientist. Cambridge University Press, Cambridge. https://doi.org/10.1017/CBO9781139024358.
Dickson, B.L., Scott, K.M., 1997. Interpretation of aerial gamma-ray surveys-adding the geochemical factors. J. Aust. Geol. Geophys. 17, 187–200.
Eddy, B.G., Graham, D.F., Bonham-Carter, G.F., Jefferson, C.W., 2006. Mineral potential analyzed and mapped at multiple scales—a modified fuzzy logic method using digital geology. In: Harris, J.R. (Ed.), GIS for the Earth Sciences. Geological Association of Canada, pp. 143–162.
Freyssinet, Ph, Butt, C.R.M., Morris, R.C., Piantone, P., 2005. Ore-forming processes related to lateritic weathering. Econ. Geol. 100th Anniv. 1, 681–722.
Freyssinet, Ph, Zeegers, H., Tardy, Y., 1989. Morphology and geochemistry of gold grains in lateritic profiles from South Mali. J. Geochem. Explor. 32, 99–116.
Grimaud, J.L., Chardon, D., Metelka, V., Beauvais, A., Bamba, O., 2015. Neogene cratonic erosion fluxes and landform evolution processes from regional regolith mapping (Burkina Faso, West Africa). Geomorphology 241, 315–330. https://doi.org/10.1016/j.geomorph.2015.04.006.
Horbe, A.M., Costa, M., 1999. Geochemical evolution of a lateritic Sn–Zr–Th–Nb–Y–REE-bearing ore body derived from apogranite: the case of Pitinga, Amazonas – Brazil. J. Geochem. Explor. 66, 339–351. https://doi.org/10.1016/S0375-6742(99)00002-3.
IAEA - International Atomic Energy Agency, 1991. Airborne Gamma Ray Spectrometer Surveying. Technical Reports Series N° 323. Viena.
Iza, E.R.H., de, F., Horbe, A.M.C., Silva, A.M., 2016. Boolean and fuzzy methods for identifying lateritic regoliths in the Brazilian Amazon using gamma-ray spectrometric and topographic data. Geoderma 269, 27–38. https://doi.org/10.1016/j.geoderma.2016.01.037.
Iza, E.R.H.F., Horbe, A.M.C., Castro, C.C., Herrera, I.L.I.E., 2018. Integration of geochemical and geophysical data to characterize and map lateritic regolith: an example in the Brazilian Amazon. G-cubed 19, 3254–3271. https://doi.org/10.1029/2017GC007352.
Jayawardhana, P.M., Sheard, S.N., 2000. The use of airborne gamma-ray spectrometry—a case study from the Mount Isa inlier, northwest Queensland, Australia. Geophysics 65. https://doi.org/10.1190/1.1444883, 1993–2000.
Jost, H., Chemale, F., Dussin, I.A., Tassinari, C.C.G., Martins, R., 2010. A U–Pb zircon Paleoproterozoic age for the metasedimentary host rocks and gold mineralization of the Crixás greenstone belt, Goiás, Central Brazil. Ore Geol. Rev. 37, 127–139. https://doi.org/10.1016/j.oregeorev.2010.01.003.
Jost, H., Fortes, P.T.F.O., 2001. Gold deposits and occurrences of the Crixás goldfield, central Brazil. Miner. Depos. 36 (3–4), 358–376.
Klir, G.J., 2004. Fuzzy logic: a specialized tutorial. In: Demicco, R.V., Klir, G.J. (Eds.), Fuzzy Logic in Geology. Elsevier Academic Press, San Diego, pp. 11–61.
Kuyumjian, R.M., Cruz, E.L.C.C., Araújo Filho, J.O., Moura, M.A., Guimarães, E.M., Pereira, K.M.S., 2012. Geologia e ocorrências de ouro do Terreno Granito-Greenstone do Tocantins, TO: síntese do conhecimento e parâmetros para exploração mineral. Rev. Bras. Geociencias 42, 213–228. https://doi.org/10.25249/0375-7536.2012421213228.
Landis, J.R., Koch, G.G., 1977. The measurement of observer agreement for categorical data. Source: Biometrics 33, 159–174.
Larizzatti, J.H., Oliveira, S.M.B., Butt, C.R.M., 2008. Morphology and composition of gold in a lateritic profile, Fazenda Pison garimpo, Amazonas, Brasil. J. South Am. Earth Sci. 25, 359–376. https://doi.org/10.1016/j.jsames.2007.06.002.
Lobato, L.M., Ribeiro-Rodrigues, L.C., Vieira, F.W.R., 2001. Brazil's premier gold province. Part 11: geology and genesis of gold deposits in the Archean rio das velhas greenstone belt. Quadrilátero ferrífero. Miner. Depos. 36, 249–277. https://doi.org/10.1007/s001260100180.
Martelet, G., Drufin, S., Tourliere, B., Saby, N.P.A., Perrin, J., Deparis, J., Prognon, F., Jolivet, C., Ratie, C., Arrouays, D., 2013. Regional regolith parameter prediction using the proxy of airborne gamma ray spectrometry. Vadose Zone J. 12 (4) https://doi.org/10.2136/vzj2013.01.0003.
Martelet, G., Truffert, C., Tourliere, B., Ledru, P., Perrin, J., 2006. Classifying airborne radiometry data with Agglomerative Hierarchical Clustering: a tool for geological mapping in context of rainforest (French Guiana). Int. J. Appl. Earth Obs. Geoinf. 8, 208–223. https://doi.org/10.1016/j.jag.2005.09.003.
Martins-Ferreira, M.A.C., Campos, J.E.G., Pires, A.C.B., 2017. Near-mine exploration via soil geochemistry multivariate analysis at the Almas gold province, Central Brazil: a study case. J. Geochem. Explor. 173, 52–63. https://doi.org/10.1016/j.gexplo.2016.11.011.
Metelka, V., Baratoux, L., Jessell, M.W., Barth, A., Jezek, J., Naba, S., 2018. Automated regolith landform mapping using airborne geophysics and remote sensing data, Burkina Faso, West Africa. Remote Sens. Environ. 204, 964–978.
Moonjun, R., Shrestha, D.P., Jettena, V.G., Ruitenbeek, F.A.J.V., 2017. Application of airborne gamma-ray imagery to assist soil survey: a case study from Thailand. Geoderma 289, 196–212. https://doi.org/10.1016/j.geoderma.2016.10.035.
Nykänen, V., Groves, D.I., Ojala, V.J., Eilu, P., Gardoll, S.J., 2008. Reconnaissance-scale conceptual fuzzy-logic prospectivity modelling for iron oxide copper - gold deposits in the northern Fennoscandian shield, Finland. Aust. J. Earth Sci. 55, 25–38. https://doi.org/10.1080/08120090701581372.
Oliveira, S.M.B., Campos, E.G., 1991. Gold-bearing iron duricrust in Central Brazil. J. Geochem. Explor. 41, 309–323. https://doi.org/10.1016/0375-6742(91)90005-F.
Oliveira, C.G., Oliveira, F.B., Giustina, M.E.S.D., Marques, G.C., Dantas, E., Pimentel, M. M., Buhn, B.M., 2015. The Chapada Cu–Au deposit, Mara Rosa magmatic arc, Central Brazil: constraints on the metallogenesis of a Neoproterozoic large porphyry-type deposit. Ore Geol. Rev. 72, 1–21. https://doi.org/10.1016/j.oregeorev.2015.06.021.
Oliveira, C.G., Pimentel, M.M., Melo, L.V., Fuck, R.A., 2004. The copper–gold and gold deposits of the Neoproterozoic Mara Rosa magmatic arc, central Brazil. Ore Geol. Rev. 25, 285–299. https://doi.org/10.1016/j.oregeorev.2004.04.006.
O'Reilly, G.A., Corey, M.C., Ford, K.L., 1988. The role of airborne gamma-ray spectrometry in bedrock mapping and mineral exploration: case studies from granitic rocks within the Meguma Zone, Nova Scotia. Marit. Sediments Atl. Geol. 4, 47–60.
Ormeling, F.J., Kraak, M.J., 2008. Maps as predictive tools – mind the gap. Cartographica 43, 125–130.
Pimentel, M.M., , Fuck, R.A., Jost, H., Ferreira Filho, C.F., Araújo, S.M., 2000. The basement of the Brasília fold belt and the Goiás magmatic arc. In: Cordani, U.G., Milani, E.J., Thomaz Filho, A., Campos, D.A. (Eds.), Tectonic Evolution of South America. Rio de Janeiro: 31st IGC. 190–229.
Pires, A.C.B., 1995. Identificação geofísica de áreas de alteração hidrotermal, Crixás-Guarinos. Goiás. Rev. Bras. Geoc. 25 (1), 61–68. https://doi.org/10.25249/0375-7536.19956168.
Porto, C.G., Hale, M., 1996. Mineralogy, morphology and chemistry of gold in the stone line lateritic profile of the Posse deposit, Central Brazil. J. Geochem. Explor. 57, 115–125. https://doi.org/10.1016/S0375-6742(96)00027-1.
Porwal, A., Deb Das, R., Chaudhary, B., Gonzalez-Alvarez, I., Kreuzer, O., 2015. Fuzzy inference systems for prospectivity modeling of mineral systems and a case-study for prospectivity mapping of surfcial Uranium in Yeelirrie Area, Western Australia. Ore Geol. Rev. 71, 839–852. https://doi.org/10.1016/j.oregeorev.2014.10.016.
Raines, G.L., Sawatzky, D.L., Bonham-Carter, G.F., 2010. New Fuzzy Logic Tools in ArcGis 10. ArcUser, ESRI.
Santosh, M., Omana, P.K., Yoshida, M., 1990. Gold grains in laterite weathering profiles of Nilambur, South India and a model for the genesis of supergene gold deposits. Journal of Mineralogy Petrography and Economic Geology 85, 416–423.
SEPLAN - Secretaria do Planejamento e da Modernização Pública, 2012. Atlas do Tocantins: Subsídios ao Planejamento da Gestão Territorial, Superintendência de Pesquisa e Zoneamento Ecológico-Econômico. Diretoria de Zoneamento Ecológico-Econômico – DZE, Palmas.
Silva, A.M., Pires, A.C.B., MacCafferty, A., Moraes, R.A.V. de, Xia, H., 2003. Application of airborne geophysical data to mineral exploration in the uneven exposed terrains of the Rio das Velhas Greenstone Belt. Rev. Bras. Geociencias 33 (2-Suplemento), 17–28.
Smith, R.E., Anand, R.R., Alley, N.F., 2000. Use and implications of paleoweathering surfaces in mineral exploration in Australia. Ore Geol. Rev. 16, 185–204. https://doi.org/10.1016/S0169-1368(99)00030-X.
Souza, M.V., Horbe, A.M.C., Silva, B.C., Peixoto, S.F., Castro, R.T., 2021. Regolith LANDSAT-8/OLI and hyperion/EO-1 images classification in midwest of Brazil. J. S. Am. Earth Sci. 111, 103460. https://doi.org/10.1016/j.jsames.2021.103460.
Tomlin, C.D., 1994. Map algebra: one perspective. Landsc. Urban Plann. 30, 3–12.
Viera, A.J., Garrett, J.M., 2005. Understanding interobserver agreement: the kappa statistic. Fam. Med. 37 (5), 360–363.
Voll, E., Silva, A.M., Pedrosa-Soares, A.C., 2020. Tracking iron-rich rocks beneath Cenozoic tablelands: an integration of geological, airborne geophysical and remote sensing data from northern Minas Gerais State, SE Brazil. J. South Am. Earth Sci. 101, 102604. https://doi.org/10.1016/j.jsames.2020.102604.
Wilford, J.R., 1995. Airborne gamma-ray spectrometry as a tool for assessing relative landscape activity and weathering development of regolith, including soils. Australian Geological Survey Organisation Research Newsletter 22, 12–14.
Wilford, J.R., 2012. A weathering intensity index for the Australian continent using airborne gamma-ray spectrometry and digital terrain analysis. Geoderma 183–184, 124–142. https://doi.org/10.1016/j.geoderma.2010.12.022.
Wilford, J.R., Bierwirth, P.N., Craig, M.A., 1997. Application of airborne gamma-ray spectrometry in soil/regolith mapping and applied geomorphology. AGSO J. Aust. Geol. Geophys. 17 (2), 201–216.
Wilford, J., Minty, B., 2007. The use of airborne gamma-ray imagery for mapping soils and understanding landscape processes. In: Lagacherie, P., McBratney, A.B., Voltz, M. (Eds.), Digital Soil Mapping an Introductory Perspective. Developments in Soil Science, vol. 31. Elsevier.
WRB, 2015. World Reference Base for Soil Resources 2014, Update 2015. International Soil Classification System for Naming Soils and Creating Legends for Soil Maps. World Soil Resources Reports No. 106. FAO, Rome.
Yang, Y., Liu, S., Jin, Z., 2009. Laterization and its control to gold occurrence in Laowanchang gold deposit, Guizhou Province, Southwest of China. J. Geochem. Explor. 100, 67–74. https://doi.org/10.1016/j.gexplo.2008.04.004.
Zadeh, L.A., 1965. Fuzzy sets. Inf. Contr. 8 (3), 338–353.
Zimmermann, H.J., 1985. Fuzzy Set Theory—And its Applications. Kluwer Academic Publishers, Dordrecht.

CAPÍTULO 3

ARTIGO CIENTÍFICO 2

REGOLITH MAPPING USING BAND RATIOS AND COMPONENT PRINCIPAL ANALYSIS TECHNICS FROM LANDSAT-8 DATA IN GRANITE-GREENSTONE TERRAIN IN MIDWEST BRAZIL

Regolith mapping using band ratios and component principal analysis techniques from Landsat-8 data in granite-greenstone terrain in Midwest Brazil

Sanclever Freire Peixoto[1,2], Adriana Maria Coimbra Horbe[1], Bárbara Costa da Silva[1], Marcus Vinicius Souza[1]

1 - Universidade de Brasília, Instituto de Geociências, Campus Universitário Darcy Ribeiro, 70910-900, Brasília, Distrito Federal, Brasil; 2 - Instituto Natureza do Tocantins-NATURATINS, Q. 302, Norte Alameda 1, s/n - Lote 3, Plano Diretor Norte, Palmas - TO, 77006-336, Brasil, sancleverp@yahoo.com.br

ABSTRACT

An area in Midwest Brazil, where there are extensive granite-greenstone terrains and weathering products, was tested for discriminating regolith units using the Landsat-8/OLI system. Band ratios and principal component analysis (PCA) techniques were used on the Landsat-8/OLI level 1T level 1 multispectral image to identify the diagnostic features of iron oxi-hydroxide, hydrous (Al–OH) and (Fe–Mg)–OH minerals, sandstone and quartzite of the regolith units of the study area. The best enhancement for the regolith units is achieved with the ratio RGB color composite R-4/2, G-6/5, B-7/4 image with overall accuracy (71%) and κ (0.37) weak to moderate. Another RGB color composite is achieved with the PCA R-PC5, G-PC3, B-PC4 image has a slight lower accuracy (61%) and κ (0.32) that is also weak to moderate. The efficiency of these band ratios predictive map computed considering all field outcrops (1745; overall accuracy = 63% and $\kappa = 0.31$) increases when the SAVI mask is used to select only field outcrops (790) not covered by vegetation (overall accuracy = 71% and $\kappa = 0.37$). Thus, although vegetation cover affects the efficiency of Landsat-8/OLI system, the application of mask to the band ratios and principal component analysis to Landsat-8 data provide good predictive regolith maps for the Midwest Brazil.

Keywords: Lateritic duricrust; Multispectral data, Band ratio; Landsat-8/OLI image; Regolith mapping.

1. Introduction

In arid-semiarid and in tropical regions, outcropping iron oxi-hydroxides zones are mineralogical conspicuous enough to be detected successfully from spaceborne multispectral and hyperspectral data (White et al., 1997, Abdelsalam et al., 2000, Feizi and Mansouri, 2013; Farooq and Govil, 2014, Ducart et al., 2016; Souza et al., 2021). In addition, these images in digital raster format, combined with a wide range layer data as airborne gamma-ray spectrometry, digital elevation models – DEM, and their derivatives (elevation, slope, curvature) amplify the successful of orbital remote sensing in geological mapping (McBratney and De Gruijter, 1992; Thurmond et al., 2006; Grimaud et al., 2015; Metelka et al., 2018).

Band ratio is a routine image processing technique used in mapping spectral features that are associated with groups of minerals and rocks. This technique in Principal Component Analysis (PCA) that is a multivariate statistical technique, has found extensive applications in multispectral and hyperspectral data (e.g., Goetz and Rowan, 1981; Crósta and Moore, 1989; Gupta et al., 2013; Pour and Hashim, 2015; Adiri et al., 2020; Souza et al., 2021). Several algorithms based in index overlay method, fuzzy logic operators, and artificial neural network models have been developed to facilitate interpretation of remote sensing and aerial geophysical data and provide accurate predictive maps (Hamedianfar et al., 2016; Metelka et al., 2018; Siqueira et al., 2021; Souza et al., 2021). These algorithms help interpret the features of regolith, determine the proportion of weathering minerals and the intensity of weathering and lateritization (Tematio et al., 2015). The use of confusion matrix to assess the efficiency of predictive map band ratios is quite common. However, its application to evaluate PC predictive map is scarce.

In Midwest Brazil, there are meta-volcano sedimentary greenstone rocks overlaid by meta-sedimentary and sedimentary sequences and intruded by granitoid units (tonalite-trondhjemite-granodiorite and gabbro plutons) (Rio das Velhas, Guarinos, Crixás, Faina and Tocantins; Cruz and Kuyumjian, 1998; Pimentel et al., 2000; Lobato et al., 2001; Jost and Fortes, 2001; Jost et al., 2010, Oliveira et al. 2004, 2015, Corrêa et al. 2015, Martins-Ferreira et al., 2017) where an extensive lateritic duricrust blanket was developed (Oliveira and Campos, 1991; SEPLAN, 2012; CPRM, 2014; Campos et al., 2016). This area was chosen to apply the spectral band ratios in supervised classification to identify the main components of the regolith in predictive maps. (Figure 1). This area had a regolith map already developed

using airborne gamma-ray spectrometry and altimetric data (Peixoto et al., 2021), thus the second goal was to compare the two techniques to find the best accurate and quickest way for regolith mapping.

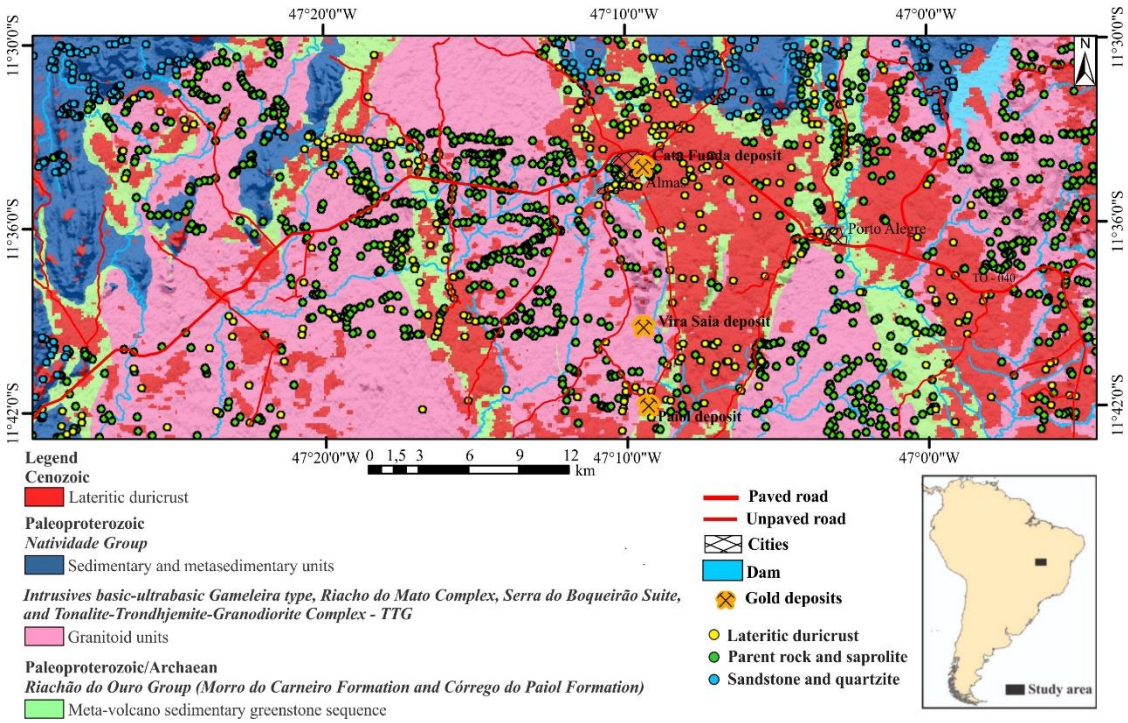

Figure 1 – Simplified geological map of the study area (after Campos et al., 2016 and Peixoto et al., 2021).

2. Materials and methods

2.1. Geological setting

The study area is located in the Midwest Brazil where outcrop meta-volcano sedimentary greenstone rocks overlaid by meta-sedimentary and sedimentary sequence and intruded by granitoid units (tonalite-trondhjemite-granodiorite and gabbro plutons) (Cruz and Kuyumjian, 1998 and Fuck et al., 2014; Figure 1). On these rocks, the tropical weathering developed widespread lateritic duricrusts that outcrops as slabs, blocks, concretions, and nodules except in the central-northern and western zones, which sustain the relief with tabular tops in a flat and wavy relief up to 490 m high. More details about the geology and geomorphology are given by Peixoto et al. (2021).

2.2. Spectral methods

For this study multispectral Landsat-8 images data are used with support of 1745 field outcrop sites observations, and a 1: 50,000 scale geologic map (Campos et al., 2016). The analysis techniques and the integration of the data are presented in the following sections.

The Landsat-8 satellite operates with the Operational Land Imager (OLI) and Thermal Infrared Sensor (TIRS) multispectral sensors. The images produced are freely available by U.S. Geological Survey Earth Observation and Science (EROS) (https://earthexplorer.usgs.gov). The electromagnetic spectrum data collected by these two instruments includes the visible, near-infrared, shortwave, and thermal regions (Tab. 1). The study area is comprised of the scene LC08221068201608222018052 8_01T1, path 221/row 68, level 1T, acquired in nadir on August 22, 2016, when there is little cloud and coincides with the dry season in the region. The large regolith exposure reduces the complexities of spectral mixing caused by the influence of vegetation (Okin et al., 2013; Guerschman et al., 2015).

Table 1 - The performance characteristics of the Landsat-8 satellite are shown in Table 1 (Irons et al., 2012; Roy et al., 2014).

Sensors	Band number	Band name	Spectral range (μm)	Ground resolution (m)	Radiometric resolution (bits)	Swath width (km)
OLI	1	Coastal	0.433–0.453	30		
	2	Blue	0.450–0.515			
	3	Green	0.530–0.590			
	4	Red	0.640–0.670			
	5	NIR	0.850–0.880			
	6	SWIR 1	1.570–1.650		16	185
	7	SWIR 2	2.100–2.290			
	8	Pan	0.500–0.680	15		
	9	Cirrus	1.360–1.380			
TIRS	10	TIRS 1	10.60–11.19	100		
	11	TIRS 2	11.50–12.51			

The Landsat-8 L1T images are pre-processed before being made available for public use. Pre-processing includes radiometric calibration, geometric correction, precision correction assisted by ground control chips, and the use of a digital elevation model to correct parallax error due to local topographic relief (Storey et al., 2008). The images were georeferenced in the UTM projection system, and reference datum WGS-84.

Atmospheric correction was applied in the bands 2 to 7 Landsat 8 level 1T (terrain corrected) image using the Fast Line-of-sight Atmospheric Analysis of Spectral Hypercubes (FLAASH) algorithm with Tropical atmospheric and Rural aerosol models. In the atmospheric correction, the raw data obtained in radiance by the imaging spectrometer are converted to reflectance units. Pre-processing and processing were performed using the ENVI 5.3 software (Fig. 2). The analysis techniques and the integration of the data are presented in the following sections.

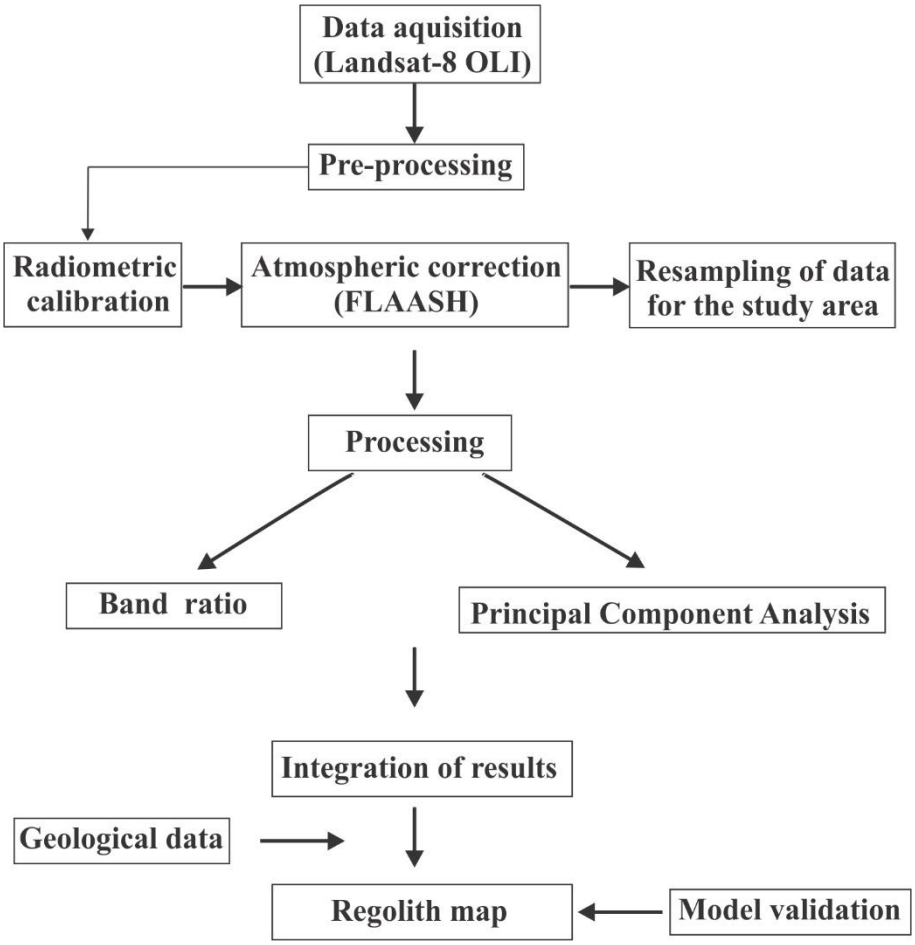

Figure 2 – Flowchart of the methodology applied for regolith mapping in Midwest Brazil.

2.3. Image analysis

Even modern multispectral remote sensing systems have complications in record image data. A multi-component image is a data set with two spatial dimensions and a component or spectral dimension. Multiple components images, such as multispectral and hyperspectral images possess high inter-band correlation due to natural spectral correlation, topographic slope, and overlap of spectral bands (Hao and Shi, 2003). Sabins (1997) proposes groups of image processing methods (*e.g.*, contrast enhancement, digital masking mosaics, merging data sets, band ratios, multispectral classification, among others) to extract the significant inter-band information, eliminate the redundancy, increase the signal/noise ratio and enhance the image, including spectral display and other characteristics of the scene that are not apparent on restored and enhanced images. False-color and natural color compositions, band ratios, and Principal Component Analysis (PCA) were applied to the VNIR (bands 2, 3, 4, 5) and SWIR (bands 6, 7) Landsat-8 OLI spectral bands.

2.3.1. Band ratios and combinations

Band ratio is a technique where the digital numbers (DN) of one band are divided by the DN values of another band in the same image. Ratio and band combination techniques produce images with high spatial resolution and have been used to improve contrast and facilitate geological and mineralogical mapping (Goetz and Rowan, 1981; Pour and Hashim, 2015). The operations between bands can highlight subtle differences in the spectral behaviour of different objects, which allows to differentiate several targets in the same image, that cannot be seen in raw bands (Inzana et al., 2003). As general rule, the addition and multiplication operations highlight the spectral similarities between the bands, on the other hand, subtraction and division highlight the spectral differences.

Iron oxi-hydroxide minerals, including hematite, goethite, and jarosite have characteristic absorption features or bands in the VNIR region (0.4 to 1.1 mm) due to charge transfer processes and iron crystalline field effect. The absorption of blue light and some green light produce the characteristic red, orange and yellow colors of these minerals (Hunt and Ashley, 1979; Clark, 1999; Rockwell, 2013). The charge transfer produces the absorption of electromagnetic energy in the range of 0.48-0.72 μm while the absorption produced by the crystalline field effect occurs in the range of 0.63-0.72 μm for ferrous iron and 0.85-1.0 μm for ferric iron (Hunt and Ashley, 1979; Sherman and Waite, 1985). Landsat-

8 bands 2, 3, 4, and 5 are in the range for these absorptions (Fig. 3). The band ratio Landsat OLI 4/2 (Landsat TM 3/1) (Abrams et al., 1983; Crósta and Moore, 1989; Tangestani and Moore, 2000; Carranza and Hale, 2002; Ducart et al., 2016; Takodjou Wambo et al., 2020) are generally used to mapping iron oxi-hydroxide rich in areas with vegetation cover. As well as OLI 5/2 and 6/5 band ratios are used in sparsely vegetated arid areas (ETM 4/1 and 5/4; Ciampalini et al., 2013). Landsat OLI 4/2 and two more complex band ratio combinations, (4/2)*(4+6)/5 (Rockwell, 2013) and (4+6)/5 (Ducart et al., 2016) were also used to mapping iron oxi-hydroxide in this study.

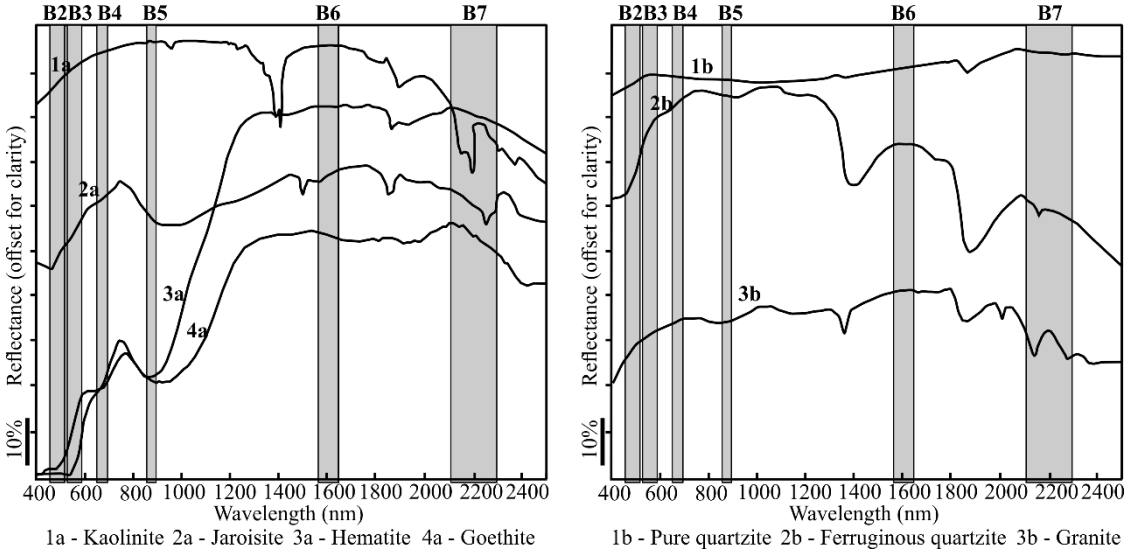

Figure 3 – Laboratory reflectance spectra of minerals and rocks. A - Reflectance spectra of iron oxi-hydroxide minerals and Al-OH and (Fe,Mg)–OH mineral groups (Clark et al., 1993), and the position of Landsat-8 bands 2, 4, 5, 6, and 7. B - Reflectance spectra of some rocks (Meneses et al., 2019).

The channels 6 and 7 of the Landsat-8 OLI (Landsat TM 5 and 7 bands) are in the spectral regions that contain characteristic features of hydrous (Al–OH) and (Fe–Mg)–OH minerals. The contrast between bands 6 (1,566 - 1,651 μm) and 7 (2.107-2.294 μm) of Landsat-8 OLI has been used to map clay minerals such as kaolinite, alunite, muscovite, chlorite, among others (Hunt, 1979; Hunt and Ashley, 1979; Takodjou Wambo, 2020) (Fig. 3A). The more complex combination Landsat-8 OLI (6/7)/(5/4) band ratios was applied to map clay in iron deposits (Ducart et al., 2016) and the 6/5 band ratio to distinguish areas of moderate to high weathering materials (mottled horizon, lateritic duricrust, and soil) with

variable iron oxi-hydroxides content, from areas with unchanged to weakly weathered rocks (parent rock and saprolite) (Ciampalini et al., 2013). These band ratios were tested for the study area.

The sandstones and quartzites porosity allow fluids percolation containing ferric ions causing decreases in reflectance from NIR to Vis. Pure quartz exhibits at relatively constant spectrum with no prominent absorption features of Vis to SWIR-2, thus the relative amounts of the other minerals will determine the absorption that quartzites may have (Fig. 3B; Hunt and Salisbury, 1970). Fig. 3B shows the decrease in reflectance of a ferruginous quartzite (2b) relative to a pure quartzite (1b) in the NIR to Vis region. An increase in the contrast between the SWIR and Vis bands is highlighted in the band ratio (7/4) and can help to identify quartzites and sandstones. The Landsat TM 4/5 band ratio (Landsat-8 OLI 5/6) has been used for the identification of unaltered rocks and common silicate minerals (Abrams et al., 1983). Landsat-8 OLI 5/6 band ratio was tested to investigate sandstone and quartzite in the study area, and the results compared to the Landsat-8 OLI 7/4 band ratio. Finally, the Soil-Adjusted Vegetation Index (SAVI) was calculated as SAVI = (1 + L) * (NIR - Red)/(NIR + Red + L) where L = 0.5, is the appropriate value for mapping the savanna biome vegetation (Huete, 1988).

Besides these band ratios and combinations, other possibilities were tested. From these, it was combining the band ratio in the RGB channels in: i: R - 4/2, G - 6/5, B - 7/4; ii: R - 4/3, G - 6/2, B - 7/4; and iii: R (4/2) * (4+6)/5, G - 6/5, B - 7/4. The results were compared to find the most efficient composition regolith units discrimination. The histograms of the band ratios allied to the field outcrop allowed estimating thresholds (Table 2) and binary images for the classes: 1) Fe-O and Fe-OH minerals abundant in the lateritic duricrust; 2) hydrous (Al–OH) and (Fe–Mg)–OH as clay minerals abundant in saprolites, and 3) blue-colored zones where sandstones and quartzites are found in the field along NNE-aligned hills in the north-central and western zones of the study area (Serra da Natividade, Fig. 1).

Table 2 – Basic statistics derived from histogram of Landsat-8 band ratios. Data in digital number (DN).

Mineral/ vegetation	Band ratio	Min	Max	Average ($\bar{X}$)	Standard deviation (σ)	Threshold
Iron oxi-hydroxides	4/2	0	6.1	2.2	0.3	$\bar{X} + 2*\sigma$

Clay minerals	6/5	0	3.2	1.1	0.2	$\overline{X}$ + 2*σ
Sandstone and quartzite	7/4	0	27.4	1.8	0.3	$\overline{X}$ + 2*σ
Vegetation	SAVI	-1.5	1.5	0.7	0.2	$\overline{X}$ + σ

A binary image for the vegetation class using Boolean logic was obtained as a mask for discrimination between field outcrops covered or not by vegetation. This discrimination of field outcrops allows the determination of the influence of the vegetation component on the regolith mapping. The Boolean logic transform an input image '*f*' to an output (segmented; Equation 1) binary image 'g' as follows:

$$g(i, j) = 1 \text{ for } f(i, j) \geq T, \quad (1)$$
$$= 0 \text{ for } f(i, j) > T$$

It is desired to pick a threshold that minimizes the error of miss-classifying a point (Bonham-Carter, 2014; Fatima et al., 2017; Fernández et al., 2018). Thresholds were driven by prior knowledge of field outcrops. The input images of band ratios 4/2, 6/5, and 7/4 were segmented into DN values close to $\overline{X}$ + 2*σ. The SAVI image was segmented into DN values ($\overline{X}$ + σ; Tab. 2) to discriminate areas of vegetation including the dry vegetation of exposed soil areas.

The segmentation of images allowed extracting the iron oxi-hydroxides minerals, clay minerals, and quartzite and sandstone features (vectors). These images segmentation provide a rule-based classification map (e.g., regolith map, land-cover map). Details regarding image classification techniques and tools can be found in Jin and Paswaters (2007), Exelis Visual Information Solutions (2009), Bhaskaran et al. (2010), Hamedianfar et al. (2014), and Hamedianfar and Shafri (2016).

2.3.2. Principal component analysis

Principal components analysis (PCA) was applied to removing the correlation allowing to compare the mineral or minerals group diagnostic reflective and absorptive bands (Crósta and Moore, 1989). This analysis was based on the covariance matrix of the 2, 3, 4, 5, 6, and 7 Landsat-8 bands. Three PC images (PC3, PC4 and PC5) were selected in the

RGB channels to obtain the PC predictive map of the regolith units. As well as on band ratios, thresholds were driven by prior knowledge of field outcrops. The input images of PC3, PC4 and PC5 were segmented into DN values (Tab. 3). The PC2 image was segmented to discriminate areas with vegetation.

Table 3 – Basic statistics derived from histogram of Landsat-8 PC bands. Data in digital number (DN).

Mineral/ vegetation	PC	Min	Max	Average ($\bar{X}$)	Standard deviation (σ)	Threshold
Iron oxi-hydroxides	5	-1743.6	3178.3	0	65.5	2/3*σ
Clay minerals	3	-2127.7	4616.7	0	191.3	1/2*σ
Sandstone and quartzite	4	-1116.9	8894.8	0	115.5	3/2*σ
Vegetation	2	-5666.7	12915.6	0	401.4	3/4*σ

2.4. Model validation

The predictive maps were evaluated from 1745 field outcrops of ferruginous lateritic duricrust mostly composed by iron oxi-hydroxides (283), saprolite composite by clay minerals (1220), and of sandstones and quartzites (242). The efficiency of the predictive mapping was performed using: 1. Overall accuracy (Congalton, 1991) expressed in percentage by OA = $\sum_{i-1}^{M} \frac{nii}{N}$ from a confusion matrix which *M* is the number of informational classes or category, *nii* is an element of the major diagonal or elements classified correctly, and *N* the total number of samples. is expressed in percentage where values close to 100 % indicate high agreement between field outcrops observations and data classification in the predictive map; 2. Kappa coefficient (κ) calculated by $\kappa = \frac{OA-Pc}{1-Pc}$, which Pc is the proportion of units which agreement is attributed to chance (Cohen, 1960). Kappa values between 1 and 0.81 indicate almost perfect agreement, between 0.80 and 0.61 indicate substantial, between 0.60 and 0.41 indicate moderate, and values closer to 0 indicate lower agreement (Landis and Koch, 1977).

Confusion matrices of predictive mapping with band ratios and PC bands presented use only field outcrops not covered by vegetation. For the selection of these field outcrops,

SAVI and PC vegetation images were used as a mask. The overall accuracy and κ were also calculated without using the masks. These two approaches to predictive mapping analysis make it possible to minimize the influence of vegetation on the accuracy of the results.

3. Results and discussions

3.1. Band ratio and combination analysis

The high iron oxi-hydroxide minerals that form the mottled horizon, lateritic duricrust, and topsoil from lateritic profiles, have been highlighted in the 4/2 bands ratio image as the high DN pixels (Fig. 4). These horizons are mainly developed from meta-volcano sedimentary greenstone sequence in the central zone and, subordinately, from the granitic units in the southeast of the study area (Fig. 4A and 1) and mapped as moderate to extremely weathered in previous study (Peixoto et al., 2021). This confirms the efficiency of the 4/2 band ratio in detecting high iron oxi-hydroxide minerals terrains. However, the (4+6)/5 bands combination used to detect high iron oxi-hydroxide minerals by Ducart et al., (2016) exhibited bright pixels mainly in zones where lateritic duricrusts are scarce being inaccurate to map iron oxi-hydroxide mineral in the study area (Fig. 5A, and 1). The (4/2)*((4+6)/5) bands combination highlighted the lateritic duricrust zones and produced an image similar to the 4/2 band ratio (Fig. 6 and 4A; Rockwell, 2013).

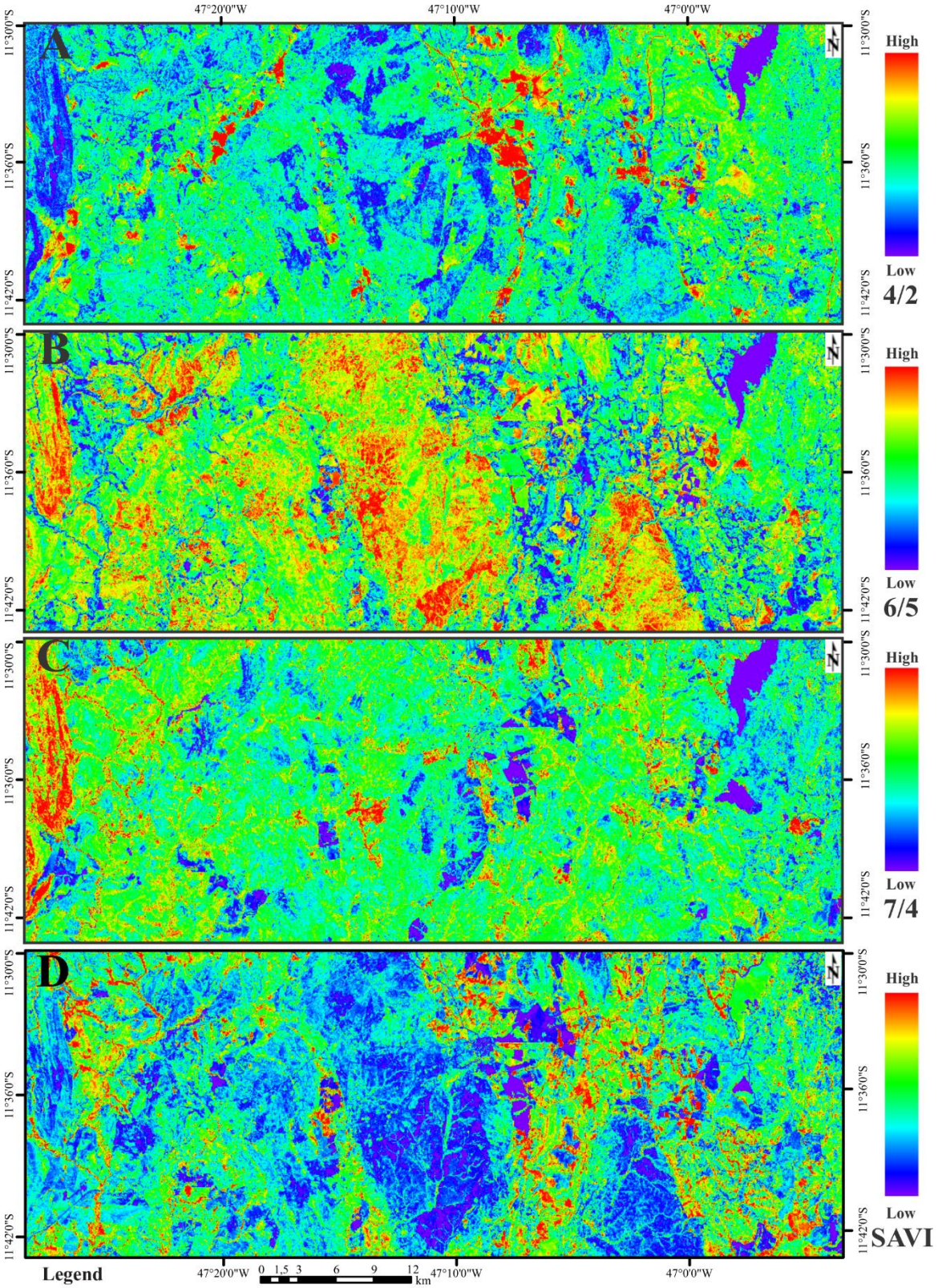

A - Iron oxi-hydroxide minerals

B - Hydrous (Al–OH) and (Fe–Mg)–OH minerals (clay minerals)

C - Sandstone and quartzite

D - Vegetation

274

Figure 4 – Pseudo-color ramp applied to each band ratio image of alteration minerals and vegetation: (A) 4/2 band ratio for mapping iron oxi-hydroxide; (B) 6/5 band ratio for mapping hydrous (Al–OH) and (Fe–Mg)–OH minerals; (C) 7/4 band ratio for mapping sandstone and quartzite; (D) SAVI for mapping vegetation.

The 6/5 band ratio for mapping (Al–OH) and (Fe–Mg)–OH minerals (Hunt, 1979; Hunt and Ashley, 1979; Goetz and Rowan, 1981; Ciampalini et al., 2013; van der Werff and van der Meer, 2016) produces bright pixels image where outcrops TTG, sedimentary and metasedimentary rocks and derived saprolite in the study area (Fig. 4B and 1). However, despite 6/7 band ratio is also very useful for this goal (Hunt and Ashley, 1979; Takodjou Wambo, 2020), in our study, the image produced was inaccurate to identify the TTG saprolite and overlaps the lateritic duricrust areas already marked by the 4/2 band ratio. This 6/7 band ratio also highlighted vegetation and drainage zones (Fig. 5B). The ratio of bands (6/7)/(5/4) image of Ducart et al. (2016) highlights both TTG unit and the lateritic duricrust (Fig. 5C and 1) not being efficient to distinguish among parent rock, lateritic duricrust, and cultivation areas.

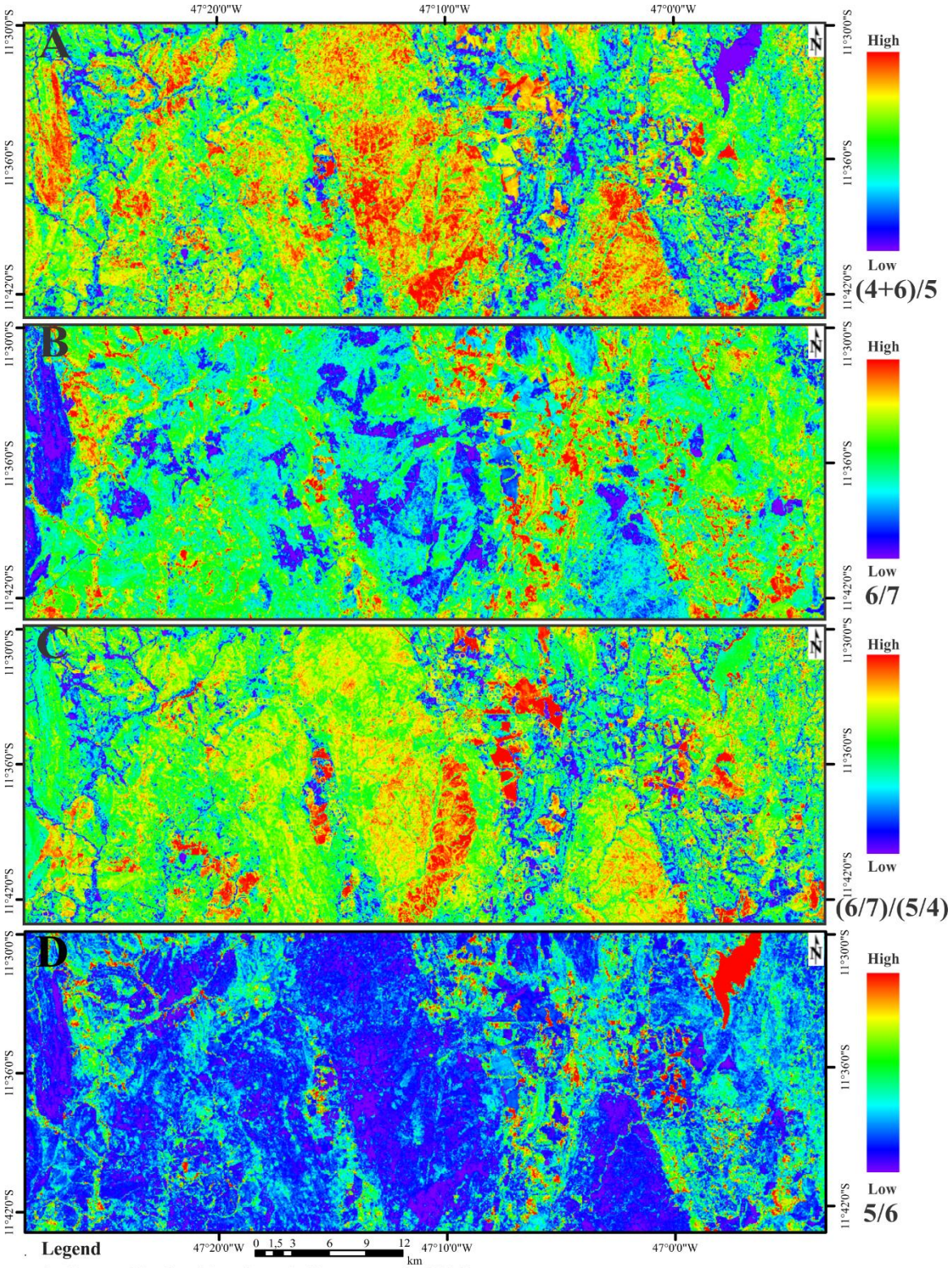

A - Iron oxi-hydroxide minerals (Ducart et al., 2016)

B - Hydrous (Al–OH) and (Fe–Mg)–OH minerals (Goetz and Rowan, 1981; van der Werff and van der Meer, 2016)

C - Clay minerals (Ducart et al., 2016)

D - Unaltered rock and common silicate minerals (Abrams et al., 1983)

291

Figure 5 – Pseudo-color ramp applied to band ratio images used by other authors: (a) (4+6)/5 band ratio for mapping iron oxi-hydroxide minerals (Ducart at al., 2016); (b) 6/7 band ratio for mapping hydrous (Al–OH) and (Fe–Mg)–OH minerals (clay minerals) (Goetz and Rowan, 1981; van der Werff and van der Meer, 2016); (c) (6/7)/(5/4) band ratio for mapping clay minerals (Ducart et al., 2016); and (d) 5/6 band ratios for mapping sandstone and quartzite (Abrams et al., 1983).

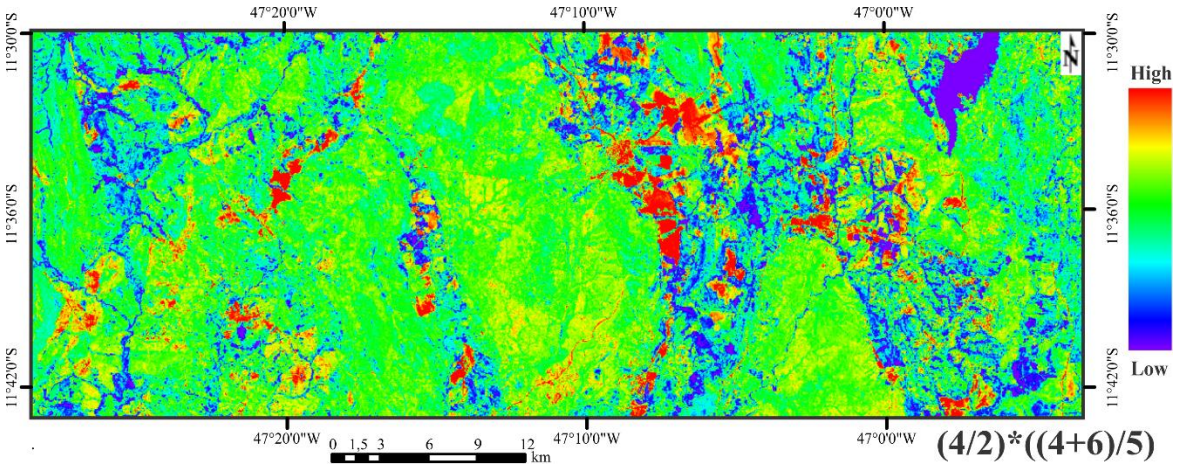

Figure 6 – Pseudo-color ramp of the (4/2)*((4+6)/5) band ratio combination image for mapping of iron oxi-hydroxide minerals (Rockwell, 2013).

The 7/4 band ratio for mapping sandstone and quartzite spectral features, highlights the zones with bright pixels, mainly in the west and north-central where these rocks outcrop in the study area (Fig. 1 and 4C). The 5/6 band ratio also used for discriminate unaltered sandstone and quartzite (Abrams et al., 1983; Landsat TM 4/5) was inaccurate in the study area and detected vegetation in bright pixels in some locations (Fig. 5D). Therefore, as silica does not show diagnostic spectral features in the VNIR/SWIR regions, the identification of the group of minerals highlighted in bright pixels in the 7/4 band ratio image is a gap in the mapping of the regolith of the Almas region.

Although the spectral reflectance of vegetation is a spectral mixture, which includes soil background as one of the components, the SAVI image is more efficient to vegetation mapping in the study area (Fig. 4D) compared to the 5/6 band ratio image (Huete, 1998; Prudnikova et al., 2019).

In the three band ratios selected in the RGB channels (4/2, 6/5, 7/4; 4/3, 6/2, 7/4; (4/2)*(4+6)/5, 6/5, 7/4), were used red for 4/2 band ratio, green for 6/5, and blue for 7/4 to

obtain the most appropriate false-color composition for the study area (Fig. 7A). Hence, red and orange pixels highlight zones with iron oxi-hydroxide minerals (lateritic duricrust, mottled horizon, and topsoil); green pixels the zones with hydrous (Al – OH) and (Fe – Mg)–OH minerals (parent rock and clay saprolite); and blue pixels sandstone and quartzite. The RGB R - (4/2) * ((4+6)/5), G - 6/5, B - 7/4 image (Fig. 7C) is similar to 4/2, 6/5, 7/ 4 image and are both efficient to discriminate between lateritic duricrust and TTG units. On the other hand, the RGB R-4/3, G-6/2, B-7/4 image (Fig. 7B; Mwaniki et al., 2015) presents lower contrast between the zones with hydrous (Al – OH) and (Fe–Mg)–OH minerals and zones with iron oxi-hydroxide minerals both highlighted in purple, red and orange pixels. The granitoids of the TTG Complex in intrusive or faulted contact with greenstone belts are highlighted and show regular mosaic patterns in the three RGB images in Figure 7. Sandstone and quartzite in the west zone (Natividade Group) are subordinately highlighted for the three combinations of tested band ratios.

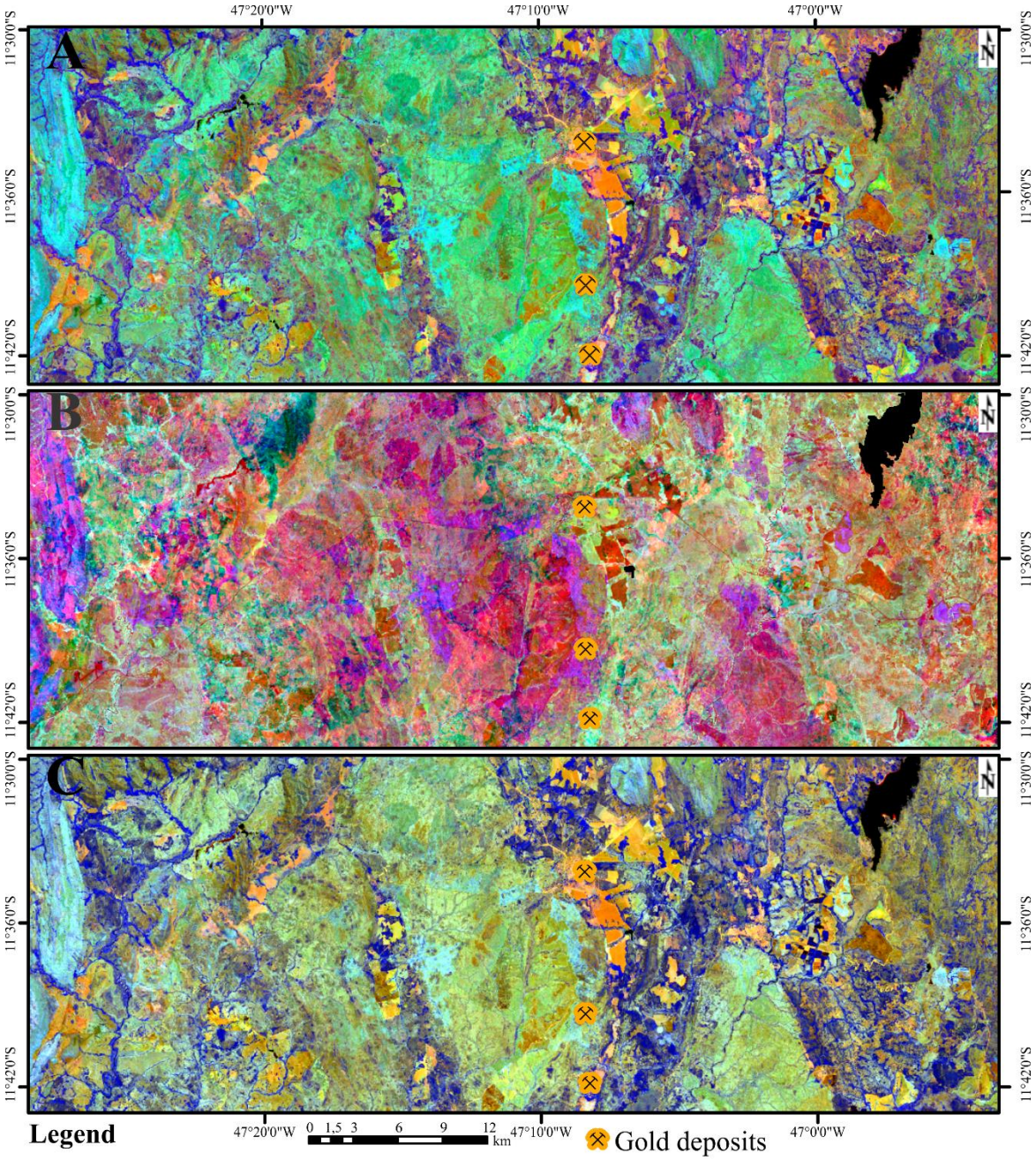

Figure 7 – Combinations of RGB images to improve the contrast in the geological information of the regolith in Almas. A) R-4/2, G-6/5, B-7/4: in this image, lateritic duricrust, mottled horizon, and topsoil appear in red and orange pixels; parent rock and saprolite in green; sandstone, quartzite and silicification zones appear in blue pixels. B) R-4/3, G-6/2, B-7/4: rock, saprolite and lateritic duricrusts zones are highlighted in purple, red and orange pixels. Sandstone, quartzite and silicification zones appear in blue and purple in

the west zone. C) R-(4/2) * ((4+6)/5), G-6/5, B-7/4 image is similar to (A), and both discriminate between lateritic duricrust and saprolite.

The basic statistical data calculated for Landsat-8 (4/2, 6/5, 7/4, SAVI) band ratios are in Table 2. The threshold value for 4/2 band ratio is 2.8, which means that iron oxi-hydroxides minerals lie between 2.8 to 6.1 (Tab. 2); hydrous (Al–OH) and (Fe–Mg)–OH minerals between 1.3 to 3.2; sandstone and quartzite between 2.4 to 27.4; and vegetation between 0.9 to 1.5. These thresholds allowed automated extracting of features of the regolith profile (Inzana et al., 2003; Souza et al., 2021).

3.2. PCA analysis

The PCA statistical eigenvector factors for the 2, 3, 4, 5, 6, and 7 bands of Landsat-8 bands are in Table 4. The PC1 with the highest variance (86%) but low variability in the eigenvector factors does not discriminate important spectral features in the analysis, However, it provides information about albedo (the ratio of the amount of electromagnetic energy reflected by a surface to the amount of energy incident upon it) and topography (Holben and Justice, 1981; Conese et al., 1988). Illumination differences due to topography, surface shading caused by solar illumination angle and slope orientation are the major source of spurious information in raw images of rugged terrain (Colby, 1991). This information in addition to water and organic matter, may have strongly affected in the accuracy of regolith mapping (Ricchetti, 2000; Silvero et al., 2020).

Table 4 - PCA statistical eigenvector factors for bands of Landsat-8 OLI. Original data set.

Eigenvector	Band 2	Band 3	Band 4	Band 5	Band 6	Band 7	Variance (%)
PC1	0.1563	0.2144	0.3461	0.2326	0.6708	0.5530	86.0239
PC2	-0.0756	0.0033	**-0.0397**	**0.9285**	0.0128	-0.3611	10.4242
PC3	-0.3231	-0.4767	-0.5423	**-0.0860**	**0.6007**	-0.0770	2.3687
PC4	0.0804	-0.0595	**-0.5508**	0.2577	-0.3755	**0.6923**	0.8628
PC5	**0.6742**	0.4244	**-0.4837**	-0.0793	0.2155	-0.2803	0.2776
PC6	0.6359	-0.7369	0.2172	0.0610	-0.0390	-0.0083	0.0427

Note[1]. Bold values were referenced in the text.

The PC2 contributes 10% of the total variance. This PC has a lower eigenvector factor in band 4 (-0.0397) and higher in band 5 (0.9285), indicate it is related to vegetation pixels (Tab. 4; Conese et al., 1988). Figure 8D displays the bright pixels overlaid on the PC image by green pixels on the segmented SAVI image. This is also indicated by the pixels along with the drainage systems and on the meta-volcano sedimentary greenstone sequence units in the central and southeastern zones of the study area where the vegetation is well developed.

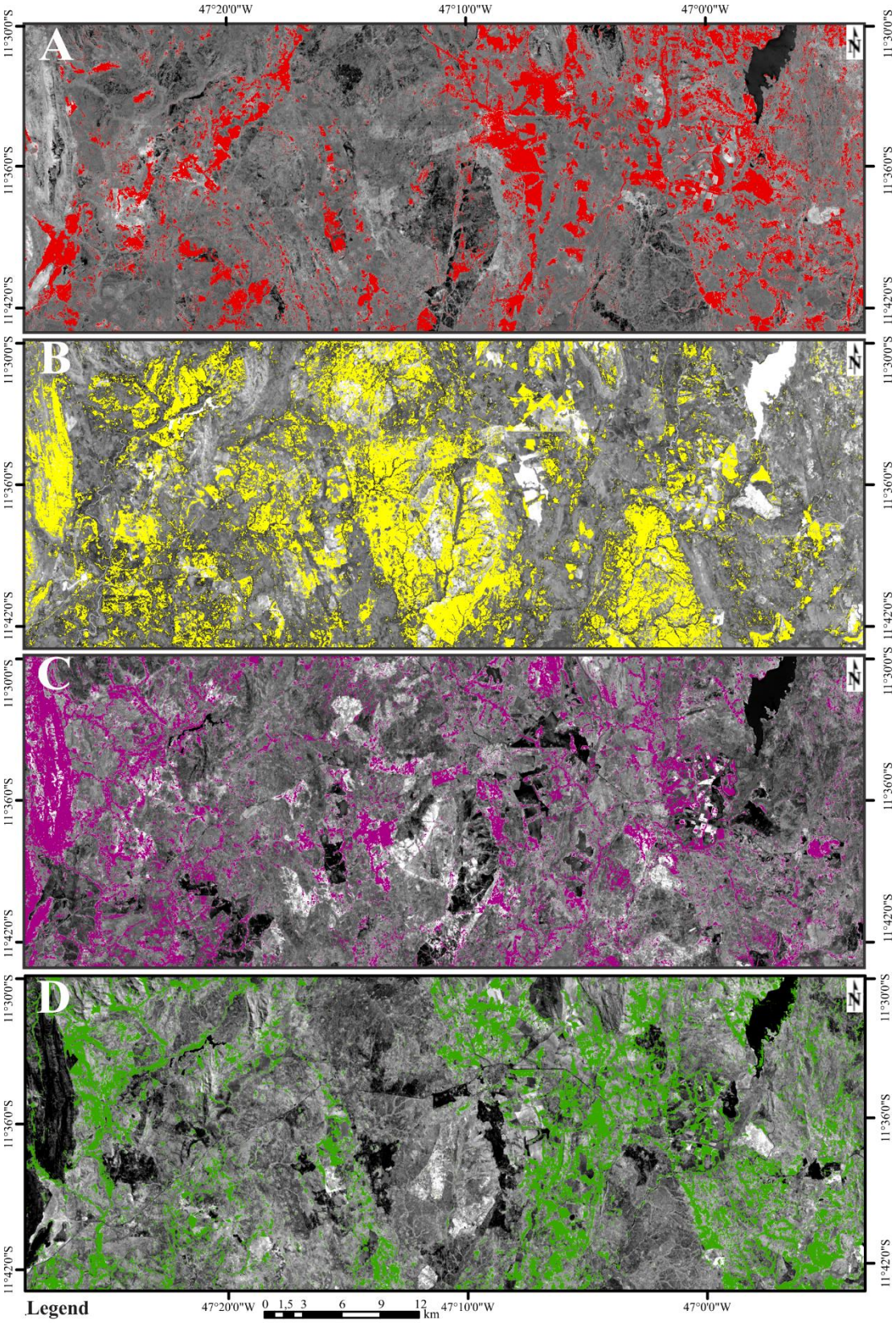
47°20'0"W
47°10'0"W
47°0'0"W
11°30'0"S
11°36'0"S
11°42'0"S
A
B
C
D
N
Legend
0 1,5 3 6 9 12 km
A - Iron oxy-hydroxide minerals
B - Hydrous (Al–OH) and (Fe–Mg)–OH minerals
C - Sandstone and quartzite
D - Vegetation

369

Figure 8 – PC images of the study area overlaid by the band ratios mask to alteration minerals (4/2 e 6/5), sandstone and quartzite (7/4), and vegetation (SAVI). (a) PC5 image showing Fe oxi-hydroxide minerals in red pixels; (b) PC3 image showing clay minerals as purple pixels; (c) PC4 image showing sandstone, quartzite, and silicification zones, and (d) PC2 image showing the vegetation in the study area.

PCs 3 to 6 have a lower contribution to the total variance than PCs 1 and 2, but they give important information about mineral or minerals group. When the loading is positive in the reflective band the pixels has bright tone in the image, allowing to investigated mineral features (Loughlin, 1991; Gupta et al., 2013; Tangestani and Moore, 2000).

The PC3 has lower eigenvector factor in band 5 (-0.0860) and higher in 6 (0.6007) (Tab. 4). Despite the weak value of band 5, a simple negation of PC3 will indicate high IR reflectance by bright pixels Loughlin (1991). Furthermore the positive eigenvector loading in band 6 (reflection band) relative band 5 according to the theoretical basis (Fig. 8B; Crósta and Moore, 1989) follows the hydrous (Al–OH) and (Fe–Mg)–OH minerals (clay minerals). This is highlighted by the clay minerals (yellow pixels) spatially distributed in the central and western zones of the study area, where outcrop the TTG Complex and Natividade Group, respectively (Fig. 8B and 1).

The PC4 eigenvector has a substantial contribution loading of bands 7 (0.6923) and 4 (-0.5508) with oppositely signed loads (Tab. 4). The positive eigenvector loading in band 7 reflected the distribution of sandstones and quartzites as bright pixels in PC4 image. Figure 8C displays also that these areas in PC4 image overlaid by purple pixels obtained from the binary mask image (7/4 band ratio) were mapped in the Natividade Group, located at the west end of the study area (Fig. 1).

PC5 has a strong negative contribution in band 4 (-0.4837) and strong positive contribution in band 2 (0.6742). Hence, iron oxi-hydroxide minerals appear in grey to bright pixels tone on the PC5 image (Fig. 8A). The zones highlighted in red in this image correspond to the lateritic duricrusts on the meta-volcano sedimentary rocks in the central zone, and on granitic units in the southeast of the study area (Fig. 8A and 1).

The RGB color composite of the PC5 in red, PC3 in green, and PC4 in blue endorse the mapping procedures in the study area (Fig. 9). The iron oxi-hydroxide minerals mapped in the meta-volcano sedimentary greenstone sequence (Fig. 9 and 1) appear in red, orange,

and yellow colors. The Al–OH, (Fe,Mg)–OH mineral groups stand out as green, light green, and yellow colors in the TTG Complex units. Silicification zones (and unaltered rocks) are depicted as blue in the Natividade Group, as well as in part of the TTG Complex (Fig. 9 and 1).

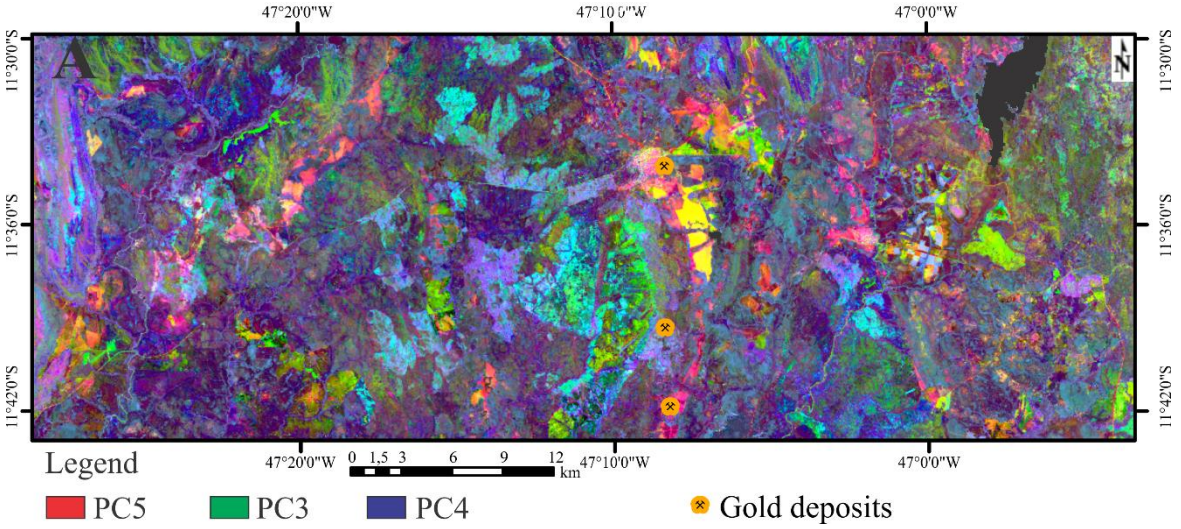

Figure 9 – RGB color composite of PC5, PC3, and PC4 showing alteration zones, lithological units in the study area. Iron oxi-hydroxide minerals appear in in red, orange, and yellow colors; clay mineral group in green, light green, and yellow colors; and silicification zones (and unaltered rocks) as blue in the Natividade Group and part of TTG Complex.

3.3. Predictive multispectral maps of regolith at regional scale

The classification by statistical attribute rules indicates the R-4/2, G-6/5, B-7/4 (Fig. 7A) has the best contrast for the study area, and it is the input for the band ratios predictive regolith map (Fig. 10). The confusion matrix shows an overall weak to moderate accuracy (71%) and κ (0.37) (Tab. 5), which was expected due to the complications in distinguishing parent rock and saprolite, because their chemical and mineralogical compositions are very similar (Horbe and Costa, 1999, Anand and Paine, 2002). These data indicate that 4/2 band ratio is an optimal combination for mapping the iron oxi-hydroxide of hematite and goethite in greater amounts in the lateritic duricrust, mottled horizon, and in the topsoil (Fig. 10 and 4A; Abrams et al., 1983; Takodjou Wambo et al., 2020; Traore et al., 2020; Souza et al., 2021). The 6/5 band ratio successfully highlighted the hydrous (Al–OH) and (Fe–Mg)–OH of kaolinite, alunite, muscovite, and chlorite the common minerals in bedrock (Fig. 10 and 4B; Goetz and Rowan, 1981; van der Werff and van der Meer, 2016). The 7/4 band ratio

highlights the quartzites and sandstone (Fig. 10 and 4C; Mwaniki et al., 2015). The visual investigation of Fig. 7 allows to affirm that, in general, the zones highlighted in red pixel (lateritic duricrusts) in Fig 7A are opposite to the zones in yellow pixels (parent rock and saprolite) in Fig. 7B, which confirms the success of 4/2 and 6/5 band ratios on the regolith mapping.

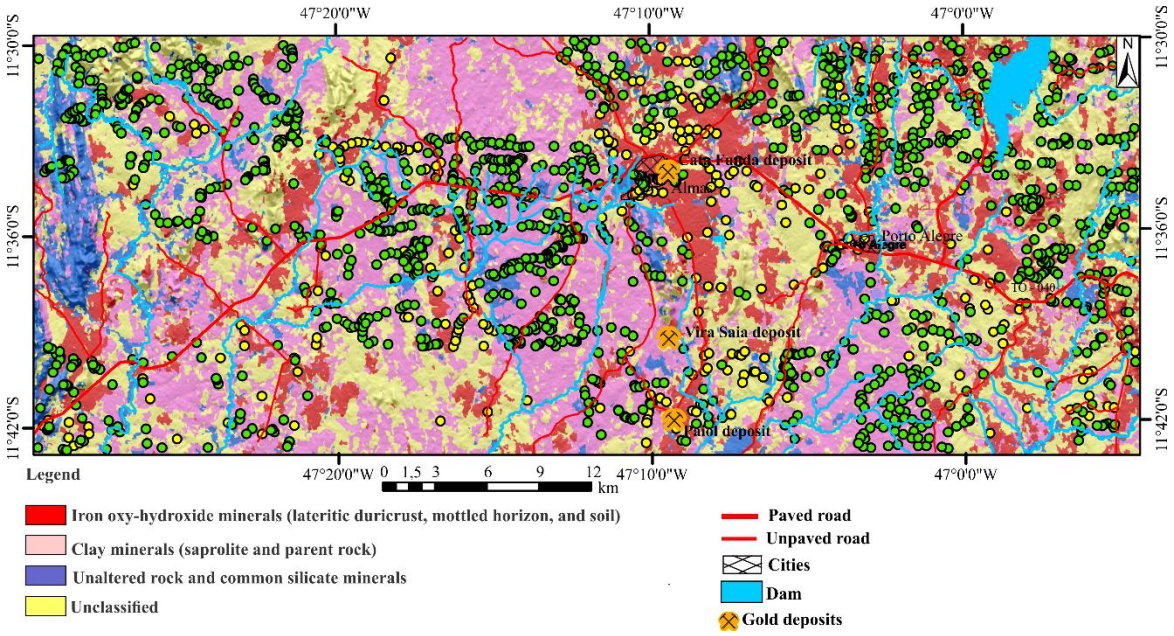

Figure 10 – Band ratios predictive map of regolith in the Almas region overlaid on the shaded altimetry. The unclassified pixels correspond to masked areas which do not have a numerical value assigned.

Table 5 – Confusion matrix of band ratios predictive map. Number of samples per class used to calculate overall accuracy and Kappa coefficient. 1: iron oxi-hydroxide minerals; 2: clay minerals; 3: sandstone and quartzite.

	Predictive map	1	2	3	Total
Field outcrops observations	1 - Lateritic duricrust	56	30	3	89
	2 - Parent rock and saprolite	120	458	41	619
	3 - Sandstone and quartzite	25	12	45	82
	Total	120	500	89	790

The results show that from the total mapped area (1,538.1 km^2), those of the iron oxi-hydroxide class (18.13%; Tab. 6) have substantial accuracy for the occurrence of lateritic duricrusts, mottled horizon, and topsoil. Clay class (33.28%) predicted parent rock and saprolite. Sandstone and quartzite class predicted sandstone, quartzite, and silicification zones over a smaller part of the area (7.73%). Unclassified pixels (40.86%) that correspond to most of the study area identify vegetation (Fig. 8D and 10) and affect the accuracy overall and κ coefficient. The efficiency of the predictive map band ratio (overall accuracy = 63% and κ = 0.31) increases when the SAVI mask is used to select only field outcrops (790 from a total of 1745) not covered by vegetation (overall accuracy = 71% and κ = 0.37; Tab. 5).

Table 6 - Summary of areas generated by rules classification for the band ratios predictive map of regolith units.

Class	Pixel amount	Area (Km^2)	Area (%)
Iron oxi-hydroxide minerals	309,864	278.88	18.13
Clay minerals	568,846	511.98	33.28
Sandstone and quartzite	132,206	118.99	7.73
Unclassified	698,418	628.58	40.86
Total	1,709,334	1,538.43	100

PCA analysis revealed patterns in the R-PC5, G-PC3, B-PC4 image providing the PC predictive map of regolith to the study area (Fig. 11) with an overall accuracy (61%) and κ (0.32) weak to moderate (Tab. 7). This accuracy is approximately 10% lower than the band ratios predictive map since the PCA map has a higher number of unclassified pixels (60.87%; Tab. 8), which are mainly vegetation areas. The areas mapped as lateritic duricrusts (10.78%) and clay minerals (18.8%) are smaller, while sandstone and quartzite are marginally equal (9.55%) relative to map done with R-4/2, G-6/5, B-7/4 map (Fig. 10; 18.13%, 33.28% and 7.33%, Tab. 6).

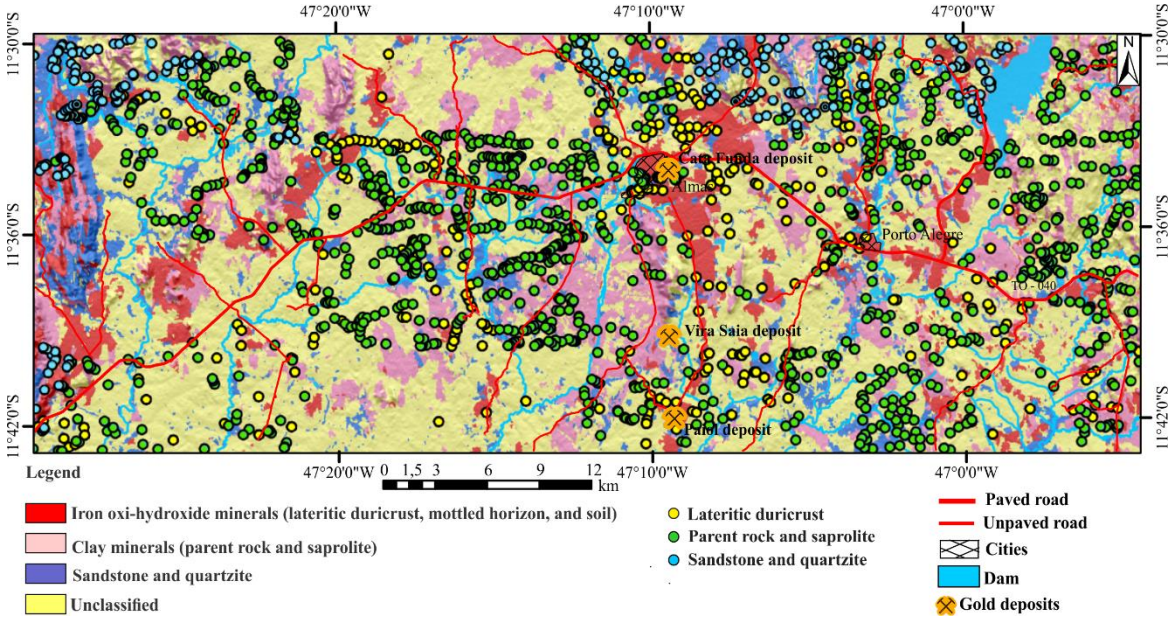

Figure 11 – PC predictive map of regolith in the Almas region overlaid on the shaded altimetry. The unclassified pixels correspond to masked areas which do not have a numerical value assigned.

Table 7 – Confusion matrix of PC predictive map. Number of samples per class used to calculate overall accuracy and Kappa coefficient. 1: iron oxi-hydroxide minerals; 2: clay minerals; 3: sandstone and quartzite.

	Predictive map	1	2	3	Total
Field outcrops observations	1 - Lateritic duricrust	56	6	5	67
	2 - Parent rock and saprolite	70	251	71	392
	3 - Sandstone and quartzite	40	25	33	98
	Total	166	282	109	557

Table 8 - Summary of areas generated by rules classification for the PC predictive map of regolith units.

Class	Pixel amount	Area (Km^2)	Area (%)
Iron oxi-hydroxide minerals	184,241	165.81	10.78
Clay minerals	321,545	289.39	18.80
Sandstone and quartzite	163,169	146.85	9.55
Unclassified	1,040,379	936.34	60.87
Total	1,709,334	1,538.39	100

The vegetation has an impact on predictive map quality, however, a visual analysis of band ratios and PC predictive maps, as well as field observations, allow to reduce the vegetation influence and improve the quality of regolith maps.

Thus, the use of processing techniques allowed to successfully discriminate the regolith units in the study areas. However, there are some limitations. While the hyperspectral imagery may help to identify the regolith specific minerals (Dehaan and Taylor, 2004; De Boissieu et al., 2018; Souza et al, 2021), the multispectral imagery enables us only to distinguish certain mineral groups. Moreover, algorithms and mapping techniques using auxiliary data (e.g., airborne gamma-ray spectrometry, hyperspectral, altimetric, and geomorphological data) can enhance image quality, and act as an additional attribute information during the classification process (Ricchetti, 2000; Metelka et al, 2018; Siqueira et al., 2021). However, these multispectral data was less accurate (61-71%) than using geophysical data (90-91%; Peixoto et al., 2021), but very useful where airborne gamma-ray spectrometry (Souza et al., 2021) and hyperspectral (Peixoto et al., 2021) data are not available.

4. Conclusions

Geological information about different weathered regolith minerals assemblies (iron oxi-hydroxide: hematite and goethite; clay: kaolinite and muscovite), sandstone, and quartzite were highlighted when calculated band ratios and principal component analysis to Landsat-8 OLI data. Both the 4/2 band ratio and (4/2)*((4+6)/5) bands combination confirming the efficiency of the 4/2 band ratio in detecting high iron oxi-hydroxide minerals in lateritic duricrust terrains. The 6/5 band ratio highlighted (Al–OH) and (Fe–Mg)–OH

minerals common in TTG, sedimentary and metasedimentary rocks, and derived saprolite outcrops. The 7/4 band ratio mapped sandstone, quartzite, and silicification zones highlighted by the high reflectance of these rocks. However, more research in the Almas region is needed to elucidate the material or minerals group that, associated with the sandstones and quartzites, have characteristic spectral signatures that allow the identification in the VNIR-SWIR bands of Landsat-8.

The best enhancement in the image for the regolith units is achieved with the RGB color composite R-4/2, G-6/5, B-7/4, which has an overall weak to moderate accuracy (71%) and κ (0.37). The greatest contrast between the regolith units is marked by the 4/2 band ratio relative to the 6/5 and 7/4 band ratios. This difference in the efficiency of band ratios is due the complications in discriminating early stages of alteration and unaltered rock highlighted by the 6/5 and 7/4 band ratios.

The RGB color composite R-PC5, G-PC3, B-PC4 endorses the mapping procedures in the study area. The PC predictive map of regolith has an accuracy (61%) and κ (0.32) weak to moderate. This accuracy slightly lower than the band ratios predictive map is caused by the greater of unclassified pixels, which correspond to the vegetation areas mainly. Although, vegetation masks and field control can minimize this problem.

The use of band ratios and principal component analysis to Landsat-8 data allowed the successful mapping of the regolith units in the study area. However, the combination of multi-source data (e.g., airborne gamma-ray spectrometry, altimetric, and geomorphological) can amplify the success of the results.

Acknowledgments

The authors thank Universidade de Brasília for the technical and physical support, Governo do Estado do Tocantins for financial support to the first autor, Conselho Nacional de Desenvolvimento Científico e Tecnológico (CNPq) for financial support (grant nº 302618/2016-3). This study was financed in part by the Coordenação de Aperfeiçoamento de Pessoal de Nível Superior - Brasil (CAPES) - Finance Code 001. The authors thank also the reviewers and editor for their valuable criticisms and suggestions.

References

Abdelsalam, M.G., Stern, R.J., Berhane, W.G., 2000. Mapping gossans in arid regions with Landsat TM and SIR-CIX-SAR images: The Beddaho alteration zone in northern Eritrea. Journal of African Earth Sciences. 30(4), 903-916. https://doi.org/10.1016/S0899-5362(00)00059-2.

Abrams, M.J., Brown, D., Lepley, L., Sadowski, R., 1983. Remote sensing for porphyry copper deposits in southern Arizona. Economic Geology. 78, 591–604.

Adiri, Z., Lhissou, R., El Harti, A., Jellouli, A., Chakouri, M., 2020. Recent advances in the use of public domain satellite imagery for mineral exploration: A review of Landsat-8 and Sentinel-2 applications. Ore Geology Reviews. 117, 103332. https://doi.org/10.1016/j.oregeorev.2020.103332.

Anand, R.R., Paine, M., 2002. Regolith geology of the Yilgarn Craton, Western Australia: implications for exploration. Australian Journal of Earth Sciences. 49, 3-162.

Bhaskaran, S., Paramananda, S., Ramnarayan, M., 2010. Per-pixel and object-oriented classification methods for mapping urban features using Ikonos satellite data. Applied Geography. 30, 650-665. https://doi.org/10.1016/j.apgeog.2010.01.009.

Bonham-Carter, G., 1994. Geographic information systems for geoscientists: Modelling with GIS. Pergamon, Oxford.

Campos, J.E.G. et al., 2016. Mapa base integrado. Projeto Almas 2016. Escala 1:50.000 [Trabalho final de graduação]. Universidade de Brasília, Curso de Geologia, Instituto de Geociências.

Carranza, E.J., Hale, M., 2002. Spatial Association of Mineral Occurrences and Curvilinear Geological Features. Mathematical Geology. 34. 10.1023/A:1014416319335.

Ciampalini, A., Garfagnoli, F., Delventisette, C., Moretti, S., 2013. Potential use of remote sensing techniques for exploration of iron deposits in Western Sahara and Southwest of Algeria. Nat. Resour. Res. 22, 179–190. https://doi.org/10.1007/s11053-013-9209-5

Clark, R.N., 1999. Spectroscopy of rocks and minerals and principles of spectroscopy, in: Rencz, A.N. (Ed.), Remote Sensing for the Earth Sciences: Manual of Remote Sensing. John Wiley & Sons, New York, pp. 3–52.

Clark, R.N., Swayze, G.A., Gallagher, A.J., King, T.V.V., Calvin, W.M., 1993. The U.S. Geological Survey, Digital Spectral Library: Version 1: 0.2 to 3.0 microns. U.S. Geological Survey Open File Report 93-592, 1340 p. http://speclab.cr.usgs.gov.

Cohen, J., 1960. A Coefficient of Agreement for Nominal Scales. Educ. Psychol. Meas. 20, 37–46. https://doi.org/10.1177/001316446002000104.

Colby, J.D, 1991. Topographic normalization in rugged terrain. Photogramm. Eng. Remote Sens. 57(5), 531-537.

Conese, C., Maracchi, G., Miglietta, F., Maselli, F., 1988. Forest classification by principal component analyses of TM data. Int. J. Remote Sens. 9(10;11), 1597-1612. https://doi.org/10.1080/01431168808954963.

Congalton, R.G., 1991. A review of assessing the accuracy of classificatins of remotely sensed data. Remote Sensing of Environment. 37, 35-46.

Corrêa, R.S., Oliveira, C.G., Vidotti, R.M., Souza, V.S., 2015. Regional-scale pressure shadow-controlled mineralization in the Príncipe Orogenic Gold Deposit, Central Brazil. Ore Geology Reviews. 71, 273–304.

CPRM - Serviço Geológico do Brasil, 2014. Carta Geológica. Projeto Sudeste do Tocantins. Folha SC.23-Y-C - Dianópolis. Sabóia, A.M., Maneghini, P.F.V, Gonçalves, F.G. (org.). Escala 1:250.000.

Crósta, A.P., Moore, J.M., 1989. Enhancement of Landsat Thematic Mapper imagery for residual soil mapping in SW Minas Gerais state Brazil: a prospecting case history in Greenstone belt terrain. Proc. 7th Themat. Conf. Remote Sens. Explor. Geol. Calgary, 1173–1187.

Cruz, E.L.C.C., Kuyumjian, R.M., 1998. Geology and tectonic evolution of the Tocantins granite-greenstone terrane: Almas-Dianópolis region, Tocantins State, central Brazil. Rev. Bras. Geociências. 28, 173–182.

De Boissieu, F., Sevin, B., Cudahy, T., Mangeas, M., Chevrel, S., 2018. Regolith-geology mapping with support vector machine: A case study over weathered Ni-bearing peridotites, New Caledonia. Int J. Appl. Earth Obs. Geoinformation. 64, 377-385. https://doi.org/10.1016/j.jag.2017.05.012.

Dehaan, R.L., Taylor, G.R., 2004. A remote-sensing method of mapping soils and surficial lags from a deeply weathered arid region, near Cobar, NSW, Australia. Geochemistry: Exploration, Environment, Analysis. 4, 99-112. https://doi.org/10.1144/1467-7873/03-026.

Ducart, D.F., Silva, A.M., Toledo, C.L.B., Assis, L.M. de, 2016. Mapping iron oxides with Landsat-8/OLI and EO-1/Hyperion imagery from the Serra Norte iron deposits in the

Carajás Mineral Province, Brazil. Brazilian J. Geol. 46, 331–349. https://doi.org/10.1590/2317-4889201620160023.

Exelis Visual Information Solution, 2009. ENVI EX user's guide. Boulder, Colorado, USA. 275p.

Farooq, S., Govil, H. 2014. Mapping regolith and gossan for mineral exploration in the Eastern Kumaon Himalaya, India using hyperion data and object oriented image classification. Advances in Space Research. 53, 1676-1685.

Fatima, K., Muhammad, U.K.K., Kausar, A.B., Toqeer, M., Haider, N., Rehman, A.U., 2017. Mineral identification and mapping using ASTER satellite image. Journal of Applied Remote Sensing. 11(4). 046006. https://doi: 10.1117/1.JRS.11.046006

Feizi, F., Mansouri, E., 2013. Introducing the iron potential zones using remote sensing studies in South of Qom Province, Iran. Open Journal of Geology. 3, 278-286.

Fernández, A., García, S., Galar, M., Prati, R., Krawczyk, B., Herrera, F., 2018. Learning from Imbalanced Data Sets. Springer, Cham. 253-277. https://doi.org/10.1007/978-3-319-98074-4.

Fuck, R.A., Dantas, E.L., Pimentel, M.M., Botelho, N.F., Armstrong, R., Laux, J.H., Junges, S.L., Soares, J.E., Praxedes, I.F., 2014. Paleoproterozoic crust-formation and reworking events in the Tocantins Province, central Brazil: A contribution for Atlantica supercontinent reconstruction. Precambrian Research. 244, 53-74.

Goetz, A.F.H., Rowan, L.C., 1981. Geologic Remote Sensing. Science. 211, 781-791.

Grimaud, J.L., Chardon, D., Metelka, V., Beauvais, A., Bamba, O., 2015. Neogene cratonic erosion fluxes and landform evolution processes from regional regolith mapping (Burkina Faso, West Africa). Geomorphology. 241, 315–330. https://doi.org/10.1016/j.geomorph.2015.04.006.

Guerschman, J. P., Scarth, P. F., McVicar, T. R., Renzullo, L. J., Malthus, T. J., Stewart, J. B., Trevithick, R. 2015. Assessing the effects of site heterogeneity and soil properties when unmixing photosynthetic vegetation, non-photosynthetic vegetation and bare soil fractions from Landsat and MODIS data. Remote Sensing of Environment, 161, 12–26. https://doi.org/10.1016/j.rse.2015. 01.021.

Gupta, R.P., Tiwari, R.K., Saini, V., Srivastava, N., 2013. A Simplified Approach for Interpreting Principal Component Images. Adv. Remote Sens. 02, 111–119. https://doi.org/10.4236/ars.2013.22015.

Hamedianfar, A., Shafri, H.Z.M, Mansor, S., Ahmad, N., 2014. Improving detailed rule-based feature extraction of urban areas from WorldView-2 image and lidar data. Int. J. Remote Sens. 35(5), 1876–1899.

Hamedianfar, A., Shafri, H.Z.M., 2016. Integrated approach using data mining-based decision tree and object-based image analysis for high-resolution urban mapping of WorldView-2 satellite sensor data. J. Appl. Remote Sens. 10(2), 025001.

Hao, P., Shi, Q., 2003. Reversible integer KLT for progressive-to-lossless compression of multiple component images. IEEE Int. Conf. Image Process. 1, 633–636. https://doi.org/10.1109/icip.2003.1247041.

Holben, B., Justice, C., 1981. An examination of spectral band ratioing to reduce the topographic effect on remotely sensed data. Int. J. Remote Sens. 2(2), 115-133. https://doi.org/10.1080/01431168108948349.

Horbe, A.M.C., Costa, M.L. 1999. Geochemical evolution of a lateritic Sn-Zr-Th-Nb-Y-REE-bearing ore body derived from apogranite: the case of Pitinga, Amazonas – Brasil. Jour. Geochem. Explor. 66, 339-351

Huete, A.R., 1988. A soil-adjusted vegetation index (SAVI). Remote Sens. Environ. 25, 205–309. https://doi.org/10.1016/0034-4257(88)90106-X.

Huete, A.R., Jackson, R.D., Post, D.F., 1985. Spectral response of a plant canopy with different soil backgrounds 17, 37–53. https://doi.org/10.1016/0034-4257(85)90111-7.

Hunt, G.R., 1979. Near-infrared (1.3-2.4 μm) spectra of alteration minerals — Potential for use in remote sensing. Geophysics. 44 (12), 1974-1986. https://doi.org/10.1190/1.1440951.

Hunt, G.R, Ashley, R.P., 1979. Spectra of altered rocks in the visible and near infrared. Econ. Geol. 74, 1613–1629.

Hunt, G.R., Salisbury, J.W., 1970. Visible and near infrared spectra of minerals and rocks: I. Silicate minerals. Modern Geology, Amsterdam. 1, 283-300.

Inzana, J., Kusky, T., Higgs, G., Tucker, R., 2003. Supervised classifications of Landsat TM band ratio images and Landsat TM band ratio image with radar for geological interpretations of central Madagascar. J. African Earth Sci. 37, 59–72. https://doi.org/10.1016/S0899-5362(03)00071-X.

662 Irons, J. R., Dwyer, J. L., Barsi, J. A., 2012. The next Landsat satellite: The Landsat data
663 continuity mission. Remote Sensing of Environment, 122, 11-21.
664 http://doi:10.1016/j.rse.2011.08.026.
665 Jin, X., Paswanters, S., 2007. A fuzzy rule base system for object-based feature extraction
666 and classification. A fuzzy rule base system for object-based feature extraction and
667 classification. In: I. Kadar (ed). Signal processing, sensor fusion, and target recognition
668 XVI. Proceedings of SPIE. vol. 6567, 65671H–665671H.
669 Jost, H., Chemale, F., Dussin, I.A., Tassinari, C.C.G., Martins, R., 2010. A U–Pb zircon
670 Paleoproterozoic age for the metasedimentary host rocks and gold mineralization of the
671 Crixás greenstone belt, Goiás, Central Brazil. Ore Geol. Rev. 37, 127–139.
672 https://doi.org/10.1016/j.oregeorev.2010.01.003.
673 Jost, H., Fortes, P.T.F.O., 2001. Gold deposits and occurrences of the Crixás Goldfield,
674 central Brazil. Miner. Depos. 36(3-4), 358–376.
675 Landis, J.R., Koch, G.G., 1977. The Measurement of Observer Agreement for Categorical
676 Data. Source: Biometrics. 33, 159–174.
677 Lobato, L.M., Ribeiro-Rodrigues, L.C., Vieira, F.W.R., 2001. Brazil's premier gold
678 province. Part 11: Geology and genesis of gold deposits in the Archean rio das velhas
679 greenstone belt, Quadrilátero ferrifero. Miner. Depos. 36, 249–277.
680 https://doi.org/10.1007/s001260100180.
681 Loughlin, W.P., 1991. Principal Component Analysis for Alteration Mapping.
682 Photogrammetric Engineering and Remote Sensing, 57, 1163-1169.
683 Martins-Ferreira, M.A.C., Campos, J.E.G., Pires, A.C.B., 2017. Near-mine exploration via
684 soil geochemistry multivariate analysis at the Almas gold province, Central Brazil: A
685 study case. J. Geochemical Explor. 173, 52–63.
686 https://doi.org/10.1016/j.gexplo.2016.11.011.
687 Meneses, P.R., Almeida, T., 2019. Reflectância das rochas. In: Reflectância dos materiais
688 terrestres. Meneses, P.R., Almeida, T., Baptista, G.M.M.B. (org.), cap. 4. Oficina de
689 textos, São Paulo. 119-162.
690 McBratney, A.B., De Gruitjer, J.J., 1992. A continuum approach to soil classification by
691 modified fuzzy k-mean with extragrades. J. Soil Sci. 43, 159-175.
692 https://doi.org/10.1111/j.1365-2389.1992.tb00127.x.

693 Metelka, V., Baratoux, L., Jessell, M.W., Barth, A., Jezek, J., Naba, S., 2018. Automated
694 regolith landform mapping using airborne geophysics and remote sensing data, Burkina
695 Faso, West Africa. Remote Sens. Environ. 204, 964-978.
696 Mwaniki, M.W., Moeller, M.S., Schellmann, G., 2015. A comparison of Landsat 8 (OLI)
697 and Landsat 7 (ETM+) in mapping geology and visualising lineaments: A case study of
698 central region Kenya. The International Archives of the Photogrammetry, Remote
699 Sensing and Spatial Information Sciences, Volume XL-7/W3, 36th International
700 Symposium on Remote Sensing of Environment, Berlin, Germany. 897-903.
701 Okin, G.S., Clarke, K.D., Lewis, M.M., 2013. Comparison of methods for estimation of
702 absolute vegetation and soil fraction cover using MODIS normalized BRDF-adjusted
703 reflectance data. Remote Sensing of Environment, 130, 266-279.
704 https://dx.doi.org/10.1016/j.rse.2012.11.021.
705 Oliveira, S.M.B., Campos, E.G., 1991. Gold-bearing iron duricrust in Central Brazil. J.
706 Geochemical Explor. 41, 309–323. https://doi.org/10.1016/0375-6742(91)90005-F.
707 Oliveira, C.G., Oliveira F.B., Giustina M.E.S.D., Marques G.C., Dantas E., Pimentel M.M.,
708 Buhn B.M., 2015. The Chapada Cu–Au deposit, Mara Rosa magmatic arc, Central
709 Brazil: Constraints on the metallogenesis of a Neoproterozoic large porphyry-type
710 deposit. Ore Geology Reviews. 72, 1–21.
711 https://doi.org/10.1016/j.oregeorev.2015.06.021.
712 Oliveira, C.G., Pimentel, M.M., Melo, L.V., Fuck, R.A., 2004. The copper–gold and gold
713 deposits of the Neoproterozoic Mara Rosa magmatic arc, central Brazil. Ore Geology
714 Reviews. 25, 285–299. https://doi.org/10.1016/j.oregeorev.2004.04.006.
715 Peixoto, S.F., Horbe, A.M.C., Soares, T.M., Freitas, C.A., Sousa, E.M.D. Iza, E.R.H.F.,
716 2021. Boolean and fuzzy logic operators and multivariate linear regression applied to
717 airborne gamma-ray spectrometry data for regolith mapping in granite-greenstone
718 terrain in Midwest Brazil. Journal of South American Earth Sciences, 112. 103562.
719 Pimentel, M.M., Fuck, R.A., Jost, H., Ferreira Filho C.F., Araújo, S.M., 2000. The basement
720 of the Brasília Fold Belt and the Goiás Magmatic Arc. In: Cordani U.G., Milani, E.J.,
721 Thomaz Filho, A., Campos, D.A. (Eds.). Tectonic Evolution of South America. Rio de
722 Janeiro: 31st IGC. 190–229.

723 Pour, A.B., Hashim, M., 2015. Hydrothermal alteration mapping from Landsat-8 data, Sar
724 Cheshmeh copper mining district, south-eastern Islamic Republic of Iran. Journal of
725 Taibah University for Science. 9, 155-166.
726 Prudnikova, E., Savin, I., Vondeker, G., Grubina, P., Shishkonakova, E., Sharychev, D.,
727 2019. Influence of soil background on spectral reflectance of winter wheat crop canopy.
728 Remote Sens. 11, 1932. Doi:10.3390/rs11161932.
729 Ricchetti, E., 2000. Multispectral satellite image and ancillary data integration for geological
730 classification. Photogrammetric Engineering & Remote Sensing. 66(4), 429-435.
731 Rockwell, B.W., 2013. Automated mapping of mineral groups and green vegetation from
732 Landsat Thematic Mapper Imagery with an example from the San Juan Mountains,
733 Colorado. U.S. Geol. Surv. Sci. Investig. Map 3252 25.
734 https://doi.org/https://doi.org/10.3133/sim3252
735 Roy, D. P., Wulder, M.A., Loveland, T.A., Woodcock, C.E., Allen, R.G., Anderson, M.C.,
736 et al., 2014. Landsat-8: Science and product vision for terrestrial global change research.
737 Remote Sensing of Environment 145, 154-172.
738 https://doi.org/10.1016/j.rse.2014.02.001.
739 Sabins, F.F., 1997. Remote Sensing — Principles and Interpretation, 3rd ed. Freemam,
740 W.H., New York.
741 SEPLAN - Secretaria do Planejamento e da Modernização Pública, 2012. Atlas do
742 Tocantins: Subsídios ao Planejamento da Gestão Territorial, Superintendência de
743 Pesquisa e Zoneamento Ecológico-Econômico, Diretoria de Zoneamento Ecológico-
744 Econômico – DZE, Palmas.
745 Sherman, D.M., Waite, T.D., 1985. Eletronic spectra of Fe^{3+} oxides and oxide hidroxides in
746 the near IR and near UV. American Mineralogist. 70(11-12), 1262-1269.
747 Silvero, N.E.Q., Di Raimo, L.A.D.L., Pereira, G.S., de Magalhães, L.P., da Silva Terra, F.,
748 Dassan, M.A.A., Salazar, D.F.U., Demattê, J.A.M., 2020. Effects of water, organic
749 matter, and iron forms in mid-IR spectra of soils: Assessments from laboratory to
750 satellite-simulated data. Geoderma 375, 114480.
751 Siqueira, G.S., Veloso, G.V., Fernandes-Filho, E.I., Francelino, M.R., Schaefer, C.E.G.R.,
752 Corrêa, G.R., 2021.Evaluation of machine learning algorithms to classify and map
753 landforms in Antarctica. Earth Surf. Process. Landforms. 1-16.
754 https://doi.org//10.1002/esp.5253

Souza, M.V., Horbe, A.M.C., Silva, B.C., Peixoto, S.F., Castro, R.T., 2021. Regolith LANDSAT-8/OLI and Hyperion/EO-1 images classification in midwest of Brazil. Journal of South American Earth Sciences. 111, 103460.

Storey, J., Choate, M., Lee, K., 2008. Geometric performance comparison between the OLI and ETM+. In: Proceedings of PECORA 17 Conference — The Future of Land Imaging Going Operational, Denver, CO, USA.

Takodjou Wambo, J.D., Pour, A.B., Ganno, S., Asimow, P.D., Zoheir, B., Salles, R. dos R., Nzenti, J.P., Pradhan, B., Muslim, A.M., 2020. Identifying high potential zones of gold mineralization in a sub-tropical region using Landsat-8 and ASTER remote sensing data: A case study of the Ngoura-Colomines goldfield, eastern Cameroon. Ore Geol. Rev. 122, 103530. https://doi.org/10.1016/j.oregeorev.2020.103530

Tangestani, M.H., Moore, F., 2000. Iron oxide and hydroxyl enhancement using the Crosta Method : a case study from the Zagros Belt, Fars Province, Iran. Int. J. Appl. Earth Obs. Geoinf. 2, 140–146.

Tematio, P., Songmene, S.M., Leumbe, O.L., Nouazi, M.M., Yemefack, M., Fouateu, R.Y., 2015. Mapping bauxite indices using Landsat ETM+ imageries constrained with environmental factors in Foumban area (West Cameroon). J. African Earth Sci. 109, 47-54. https://doi.org/10.1016/jafrearsci.2015.05.010.

Thurmond, A.K., Abdelsalam, M.G., Thurmond, J.B., 2006. Optical-radar-DEM remote sensing data integration for geological mapping in the Afar Depression, Ethiopia. J. African Earth Sci. 44, 119-134. https://doi.org/10.1016/j.afrearsci.2005.10.006.

Traore, M., Takodjou Wambo, J.D., Ndepete, C. P., Tekine, S., Pour, A.B., Muslim, A.M., 2020. Lithological and alteration mineral mapping for alluvial gold exploration in the south east of Birao area, Central African Republic using Landsat-8 Operational Land Imager (OLI) data. Journal of African Earth Sciences. 170. 10.1016/j.jafrearsci.2020.103933.

Van der Werff, H.M.A., van der Meer, F.D., 2016. Sentinel-2A MSI and Landsat 8 OLI provide data continuity for geological remote sensing. Remote Sensing. 8, 883. https://doi.org/10.3390/rs8110883.

White, K., Walden, J., Drake, N., Eckardt, F., Settle, J., 1997. Mapping the iron oxide content of dune sands, Namib Sand Sea, Namibia, using Landsat Thematic Mapper data. Remote Sensing of Environment, 62, 30-39.

CAPÍTULO 4

COMPARAÇÃO ENTRE OS MODELOS DE MAPEAMENTO PREDITIVO E CONSIDERAÇÕES FINAIS

7. COMPARAÇÃO ENTRE OS MODELOS DE MAPEAMENTO PREDITIVO E CONSIDERAÇÕES FINAIS

Os modelos de mapeamento preditivo para o regolito na região de Almas foram construídos usando diferentes algoritmos, operadores lógicos, técnicas estatísticas, matemáticas e de geoprocessamento.

A modelagem desenvolvida e apresentada nesta tese forneceu cinco mapas preditivos para o regolito da área de estudo: 1- mapa preditivo Booleano (Fig. 2.11A); 2 – mapa preditivo difuso (Fig. 2.11B); 3 – mapa do índice de intensidade do intemperismo (WII; Fig. 2.12); 4 – mapa preditivo de razões de bandas (Fig. 3.10); e o mapa preditivo de componentes principais (Fig. 3.11). Os mapas 1, 2 e 3 foram elaborados usando operadores Booleano, fuzzy e regressão linear multivariada sobre os dados de gamaespectrometria aérea, enquanto os mapas 4 e 5 usando técnicas de geoprocessamento aplicadas a dados de imagens multiespectrais.

A eficiência de cada mapa foi avaliada pela acurácia e coeficiente kappa. O mapa preditivo Booleano teve acurácia = 91% e $\kappa = 0,69$; o mapa preditivo difuso acurácia = 90% e $\kappa = 0,66$; o mapa WII acurácia = 88% e $\kappa = 0,58$; o mapa preditivo de razões de bandas teve acurácia de 71% e $\kappa = 0,37$; e o mapa preditivo PC acurácia = 61% e $\kappa = 0,32$. Portanto, os mapas preditivos obtidos a partir dos dados de gamaespectrometria aérea foram mais eficientes que de dados multiespectrais para mapear o regolito da região de Almas.

Apesar dos mapas preditivos usando dados de imagens multiespectrais serem menos acurados que os de gamaespectrometria aérea, eles são apropriados para mapear o regolito em áreas onde dados de gamaespectrometria aérea não estão disponíveis.

Os princípios relacionados à aquisição, tratamento e resolução dos dados geofísicos e de imagens multiespectrais são bastante distintos e estão sujeitos à uma série de interferências (vegetação, umidade do solo, sombreamento, atmosfera, etc), as quais são inerentes à cada técnica. Os resultados sugerem que a vegetação exerceu pouca influência no mapeamento das crostas lateríticas usando gamaespectrometria aérea. Contudo, apesar da vegetação interferir de modo mais evidente na acurácia dos mapas preditivos usando imagens multiespectrais Landsat-8, não foi um impeditivo para mapear o regolito da região de estudo.

REFERÊNCIAS BIBLIOGRGRÁFICAS

Abdelsalam, M.G., Stern, R.J., Berhane, W.G. 2000. Mapping gossans in arid regions with Landsat TM and SIR-CIX-SAR images: The Beddaho alteration zone in northern Eritrea. Journal of African Earth Sciences. 30(4), 903-916. https://doi.org/10.1016/S0899-5362(00)00059-2.

Abrams, M., Tsu, H., Hulley, G., Iwao, K., Pieri, D., Cudahy, T., Kargel, J. 2015. International Journal of Applied Earth Observation and Geoinformation The Advanced Spaceborne Thermal Emission and Reflection Radiometer (ASTER) after fifteen years: Review of global products. Int. J. Appl. Earth Obs. Geoinf. 38, 292–301. https://doi.org/10.1016/j.jag.2015.01.013.

Abrams, M.J., Brown, D., Lepley, L., Sadowski, R. 1983. Remote sensing for porphyry copper deposits in southern Arizona. Economic Geology. 78, 591–604.

Adiri, Z., Lhissou, R., El Harti, A., Jellouli, A., Chakouri, M. 2020. Recent advances in the use of public domain satellite imagery for mineral exploration: A review of Landsat-8 and Sentinel-2 applications. Ore Geology Reviews. 117, 103332. https://doi.org/10.1016/j.oregeorev.2020.103332.

Albuquerque, M.F.S., Horbe, A.M.C. 2015. Mineralogia, geoquímica e evolução da lateritização em Apuí, sudeste do Amazonas. Brazilian Journal Geology 45, 569–590.

Albuquerque, M.F.S., Horbe, A.M.C., Botelho, N.F. 2017. Genesis of manganese deposits in southwestern Amazonia: mineralogy, geochemistry and paleoenvironment. Ore Geol Rev. 89, 270–289.

Albuquerque, M.F.S., Horbe, A.M.C., Soares, T.M., Sousa, E.M.D., Iza, E.R.H.F. 2020. Airborne radiometric data for identifying lateritic surface in southwestern Amazonia, Brazil. Journal of Applied Geophysics 175, 103989. https://doi.org/10.1016/j.jappgeo.2020.103989.

Aleva, G.J.J. 1994. Laterites. Concepts, Geology, Morphology and Chemistry. ISRIC, Wageningen. 153 pp.

Alkmim, F.F., Martins Neto, M.A. 2012. Proterozoic first-order sedimentar sequences of the São Francisco Craton, eastern Brazil. Marine and Petroleum Geology. 33, 127-139.

Almeida, F. F. M. 1981. O Cráton do Paramirim e suas relações com o do São Francisco. In: Simpósio sobre o Craton do São Francisco e suas Faixas Marginais, 1. Salvador. Anais...Salvador: SBG Núcleo Bahia, 1-10.

Anand, R.R. 2005. Weathering history, landscape evolution and implications for exploration. In: Butt, C.R.M.; Robertson, I.D.M.; Scott, K.M.; Cornelius, M. Editors, editor/s. Regolith expression of Australian ore systems: a compilation of exploration case histories with conceptual dispersion, process and exploration models. Perth, W.A.: CRC LEME; 2005. 15-45.

Anand, R.R. 2001. Evolution, classification and use of ferruginous materials in gold exploration, Yilgarn craton, Western Australia. Geochemistry: Exploration, Environment, Analysis. 1, 221–236. https://doi.org/10.1144/geochem.1.3.221.

Anand, R.R., Butt, C.R.M. 2010. A guide for mineral exploration through the regolith in the Yilgarn Craton, western Australia. Aust. J. Earth Sci. 57, 1015–1114. https://doi.org/10.1080/08120099.2010.522823.

Anand, R.R., Paine, M. 2002. Regolith geology of the Yilgarn Craton, Western Australia: Implications for exploration. Aust. J. Earth Sci. 49, 3–162. https://doi.org/10.1046/j.1440-0952.2002.00912.x.

Angélica, R.S., Costa, M.L. 1993. Geochemisty of rare-earth elements in surface lateritic rocks and soils from the Maicuru complex, Pará, Brazil. Journal of Geochemical Exploration. 47, 165-182.

Arhin, E., Jenkin, G.R.T., Cunningham, D., Nude, P. 2015. Regolith mapping of deeply weathered terrain in savannah regions of the Birimian Lawra Greenstone Belt, Ghana. J. Geochem. Explor. 159, 194–207.

Barbosa, I.O., Pires, A.C.B., Lacerda, M.P.C., Carmelo, A.C. 2013. Geology, airborne geophysics, geomorphology and soils in the individualization of the Niquelândia Mafic-Ultramafic Complex, Goiás State, Brazil. Revista Brasileira de Geofísica. 31, 463-481.

Barnes, S.J., Fisher, L.A., Anand, R., Uemoto, T. 2014. Mapping bedrock lithologies through in situ regolith using retained element ratios: a case study from the Agnew-Lawlers area, Western Australia. Aust. J. Earth Sci. 61, 269–285. https://doi.org/10.1080/08120099.2014.862302.

Beauvais, A., Colin, F. 1993. Formation and transformation processes of iron duricrust systems in tropical humid environment. Chem. Geol. 106, 77–101.

Bedell, R., Crósta, A.P., Grunsky, E. 1992. Remote sensing and spectral geology. Reviews in Economic Geology, v. 1. Society of Economic Geologists: Littleton, CO, USA, 2009.

Bhaskaran, S., Paramananda, S., Ramnarayan, M. 2010. Per-pixel and object-oriented classification methods for mapping urban features using Ikonos satellite data. Applied Geography. 30, 650-665. https://doi.org/10.1016/j.apgeog.2010.01.009.

Bishop, C.A., Liu, J.G., Mason, P.J. 2011. Hyperspectral remote sensing for mineral exploration in Pulang, Yunnan Province, China. International Journal of Remote Sensing. 32, 2409–2426.

Bonham-Carter, G., 1994. Geographic information systems for geoscientists: Modelling with GIS. Pergamon, Oxford, 400 pp.

Borges, M.S. 1993. Evolução tectono-estrutural da região de Dianópolis-Almas, SE do Estado do Tocantins. Tese de Doutorado, Instituto de Geociências, Universidade Federal do Pará, Belém. 365p.

Boulangé, B., Carvalho, A. 1997. The Bauxite of Porto Trombetas. In: Carvalho, A., Boulangé, B.; Melfi, A.J. & Lucas, Y. (Organizadores). Brazilian Bauxites, USP/FAPESP/ORSTOM, Brazil. 55-73.

Bowell, R.J., Afreh, E.O., Laffoley, N. d'A., Hanssen, E., Abe, S., Yao, R.K., Pohl, D. 1996. Geochemical exploration for gold in tropical soils — four contrasting case studies from West Africa. Institution of Mining and Metallurgy Transactions. 105, B12–B33.

Campos, D.S. de, Toledo, C.L.B., Carvalho, M.J. de, Rodrigues, V.G., Araujo, K., Silva, A.M. 2017. Prospectivity analysis of gold and iron oxide copper-gold-(silver) mineralizations from the Faina Greenstone Belt, Brazil, using multiple data sets. Brazilian J. Geol. 47, 561–590. https://doi.org/10.1590/2317-4889201720170012.

Campos, J.E.G. et al. 2016. Mapa base integrado. Projeto Almas 2016. Escala 1:50.000 [Trabalho final de graduação]. Universidade de Brasília, Curso de Geologia, Instituto de Geociências.

Carranza, E.J., Hale, M. 2002. Spatial Association of Mineral Occurrences and Curvilinear Geological Features. Mathematical Geology. 34. 10.1023/A:1014416319335.

Carranza, E.J.M. 2011. Geocomputation of mineral exploration targets. Comput. Geosci. 37, 1907–1916.

Carranza, E.J.M., Mangaoang, J.C., Hale, M. 1999. Application of mineral exploration models and GIS to generate mineral potential maps as input for optimum land-use planning in the Philippines. Nat. Resour. Res. 8 (2), 165–173.

Carrino, T.A., Silva, A.M., Botelho, N.F., da Silva, A.A.C. 2011. Discriminação de áreas de

espesso regolito do leste do estado do Amazonas usando estatística multivariada, algoritmo hiperespectral e modelagem de dados espaciais. Rev. Bras. Geofis. 29, 155–172. https://doi.org/10.1590/S0102-261X2011000100011.

Carrol, T.R. 1981. Airborne soil moisture measurement using natural terrestrial gamma radiation. Soil Science. 132(5), 358-366.

Castro, R.T.; Horbe, A.M.C.; Almeida, C.M. de. 2016. A crosta laterítica ferro-titanífera da Vila Nova Colina e a lateritização no sul de Roraima. Revista Acta Amazônica. 46, 47-60.

Ciampalini, A., Garfagnoli, F., Delventisette, C., Moretti, S., 2013. Potential use of remote sensing techniques for exploration of iron deposits in Western Sahara and Southwest of Algeria. Nat. Resour. Res. 22, 179–190. https://doi.org/10.1007/s11053-013-9209-5

Clark, R.N. 1999. Spectroscopy of rocks and minerals and principles of spectroscopy, in: Rencz, A.N. (Ed.), Remote Sensing for the Earth Sciences: Manual of Remote Sensing. John Wiley & Sons, New York, pp. 3–52.

Clark, R.N., Swayze, G.A., Gallagher, A.J., King, T.V.V., Calvin, W.M., 1993. The U.S. Geological Survey, Digital Spectral Library: Version 1: 0.2 to 3.0 microns. U.S. Geological Survey Open File Report 93-592, 1340 p. http://speclab.cr.usgs.gov.

Cohen, J. 1960. A coefficient of agreement for nominal scales. Educational and Psychological Measurement. 20, 37-46.

Cohen, J. 1988. Statistical power analysis for the behavioral sciences. Hillsdale, NJ, Erlbaum. 567 pp.

Colby, J.D, 1991. Topographic normalization in rugged terrain. Photogramm. Eng. Remote Sens. 57(5), 531-537.

Colin, F., Nahon, D., Trescases, J.J., Melfi, A.J. 1990. Lateritic weathering of pyroxenites at Niquelandia, Goias, Brazil; the supergene behavior of nickel. Economic Geology. 85(5), 1010-1023.

Conese, C., Maracchi, G., Miglietta, F., Maselli, F. 1988. Forest classification by principal component analyses of TM data. Int. J. Remote Sens. 9(10;11), 1597-1612. https://doi.org/10.1080/01431168808954963.

Congalton, R.G. 1991. A review of assessing the accuracy of classificatins of remotely sensed data. Remote Sensing of Environment. 37, 35-46.

Cook, S.E., Corner, R.J., Groves, P.R., Grealish, G.J. 1996. Use of airborne gamma radiometric data for soil mapping. Aust. J. Soil Res. 34 (1), 183–194.

Corrêa, R.S., Oliveira, C.G., Vidotti, R.M., Souza, V.S., 2015. Regional-scale pressure shadow-controlled mineralization in the Príncipe Orogenic Gold Deposit, Central Brazil. Ore Geology Reviews. 71, 273–304.

Costa, J.B.S. 1985. Aspectos litoestruturais e evolução crustal da região centro-norte de Goiás. Centro de Geociências, Universidade Federal do Pará, Belém, Tese de Doutoramento, 210 p.

Costa, L.A.M., Portella, A.C.P., Nilson, A.A., Vale, C.R.O., Marchetto, C.L.M., Santos, E.L., Meneguesso, G., Inda, H.A.V., Sterna, L.H., Marchetto, M., Baptista, M.B., Fratin, O., Mosmann, O., Oliveira, T. F., Silva, W. G. 1976. Projeto Leste Tocantins/Oeste do São Francisco. Relatório Final, Rio de Janeiro, DNPM/CPRM/PROSPEC, 200 p.

Costa, M.L. 1997. Lateritization as a major process of ore deposit formation in the Amazon region. Exploration Mining Geology. 6, 79-104.

Costa, M.L., Cruz, G.S., Almeida, H.D.F., Poellmann, H. 2014. On the geology, mineralogy and geochemistry of the bauxite-bearing regolith in the lower Amazon basin: Evidence of genetic relationships: Journal of Geochemical Exploration. 146, 58–74.

CPRM - Serviço Geológico do Brasil, 2006. Projeto Aerogeofísico do Tocantins, Relatório Final do Levantamento e processamento de dados magnetométricos e gamaespectrométricos. Available at: http://geosgb.cprm.gov.br/. Accessed on: 25 Nov. 2017.

CPRM - Serviço Geológico do Brasil, 2014. Carta Geológica. Projeto Sudeste do Tocantins. Folha SC.23-Y-C - Dianópolis. Sabóia, A.M., Maneghini, P.F.V, Gonçalves, F.G. (org.). Escala 1:250.000.

CPRM – Serviço Geológico do Brasil. 1998. Programa Nacional de Prospecção de Ouro – PNPO. Mapa de jazimentos auríferos. Área TO-01 – Almas – Natividade – Tocantins. Escala 1:250.000.

CPRM – Serviço Geológico do Brasil. 2008. Geologia dos Estado de Goiás e do Distrito Federal. Moreira, M.L.O., Moreton L.C., Araujo V.A., Lacerda Filho J.V., Costa H.F. (org.). CPRM/SIC – FUNMINERAL.

Craig, M.A. 2001. Regolith mapping for geochemical exploration in the Yilgarn craton, Western Australia. Geochemistry: Exploration, Environment, Analysis. 1, 383–390.

Crósta, A.P., Ducart, D.F., Souza Filho, C.R., Azevedo, F., Brodie, C. 2009. Mineral Exploration for Epithermal Gold in Northern Patagonia, Argentina: From Regional- to Deposit-Scale Prospecting Using Landsat TM and Terra ASTER. Reviews in Economic Geology, v. 16. 97-108.

Crósta, A.P., Moore, J.M. 1989. Enhancement of Landsat Thematic Mapper imagery for residual soil mapping in SW Minas Gerais state Brazil: a prospecting case history in Greenstone belt terrain. Proc. 7th Themat. Conf. Remote Sens. Explor. Geol. Calgary, 1173–1187.

Cruz, E.L.C.C., Kuyumjian, R.M., 1998. Geology and tectonic evolution of the Tocantins granite-greenstone terrane: Almas-Dianópolis region, Tocantins State, central Brazil. Rev. Bras. Geociências. 28, 173–182.

Cruz, E.L.C.C., Kuyumjian, R.M. 1999. Mineralizações auríferas filoneanas do terreno granito-greenstone do Tocantins. Rev. Bras. Geociências. 29, 291–298.

Cruz, E.L.C.C., Kuyumjian, R.M. 2006. Geochronology, isotopic signature and metallogenetic model for the Córrego Paiol gold deposit, Tocantins state, central Brazil. Rev. Bras. Geoc. 36(1-Suplemento), 152–156.

Dardenne, M.A. 2000. The Brasilia Fold Belt. In: U.G. Cordani, E.J. Milani, A. Thomaz Filho, D.A. Campos (eds.). Tectonic Evolution do South America. Rio de Janeiro, 31st International Geological Congress, SBG. 231-263.

Darnley, A.G., Ford, K.L. 1989. Regional airborne gamma-ray surveys: A review. In 'Exploration '87. Geophysical Methods: Advances in the State of the Art'. Ed. G.D. Garland. Ontario Geological Surveys. 40-229.

Dauth, C. 1997. Airborne magnetic, radiometric and sat imagery for regolith mapping in the Yilgarn Craton of Western Australia. Explor. Geophys. 28 (2), 199–203.

Davy, R., El-Ansary, M., 1986. Geochemical Patterns in the laterite profile at the boddington gold deposit, western Australia. J. Geochem. Explor. 26, 119–144. https://doi.org/10.1016/0375-6742(86)90062-2.

De Boissieu, F., Sevin, B., Cudahy, T., Mangeas, M., Chevrel, S., 2018. Regolith-geology mapping with support vector machine: A case study over weathered Ni-bearing peridotites, New Caledonia. Int J. Appl. Earth Obs. Geoinformation. 64, 377-385. https://doi.org/10.1016/j.jag.2017.05.012.

Dehaan, R.L., Taylor, G.R., 2004. A remote-sensing method of mapping soils and surficial lags from a deeply weathered arid region, near Cobar, NSW, Australia. Geochemistry: Exploration, Environment, Analysis. 4, 99-112. https://doi.org/10.1144/1467-7873/03-026.

Deller, M.E.A. 2006. Facies discrimination in laterites using Landsat Thematic Mapper, ASTER and ALI data—examples from Eritrea and Arabia. Int. J. Remote Sens. 27, 2389–2409. https://doi.org/10.1080/01431160600586050.

Dent, D.L., MacMillan, R.A., Mayr, T.L., Chapman, W.K., Berch, S.M. 2013. Use of airborne gamma radiometrics to infer soil properties for a forested area in British Columbia, Canada. J. Ecosystem Management. 14, 1–12.

Dentith, M., Mudge, S. 2014. Geophysics for the Mineral Exploration Geoscientist. Cambridge: Cambridge University Press. doi:10.1017/CBO9781139024358.

Dickson, B.L., Fraser, S.J., Kinsey-Henderson, A. 1996. Interpreting aerial gamma-ray surveys utilizing geomorphological and weathering models, Journal of Geochemical exploration. 57, 75-88.

Dickson, B.L., Scott, K.M. 1997. Interpretation of aerial gamma-ray surveys — adding the geochemical factors. AGSO J. Aust. Geol. Geophys. 17 (2), 187–200.

Drury, S. 2001. Image Interpretation in geology, 3rd Ed. Blackwell Science Inc, Malden.

Drury, S.A., Hunt, G.A. 1989. Geological uses of remotely-sensed reflected and emitted data of lateritized Archaean terrain in Western Australia. Int. J. Remote Sens. 10, 475–497. https://doi.org/10.1080/01431168908903886.

Ducart, D.F., Crósta, A.P., Souza Filho, C.R. 2007. Processamento de imagens hiperespectrais do EO-1/Hyperion para o mapeamento de minerais de alteração hidrotermal na Patagônia Argentina. Anais XIII Simpósio Brasileiro de Sensoriamento Remoto, Florianópolis, Brasil, 21-26 abril, INPE. 6449-6451.

Ducart, D.F., Silva, A.M., Toledo, C.L.B., Assis, L.M.D. 2016. Mapping iron oxides with Landsat-8/OLI and EO1/Hyperion imagery from the Serra Norte iron deposits in the Carajás Mineral Province, Brazil. Brazilian Journal of Geology. 46(3), 331-349.

Eddy, B.G., Graham, D.F., Bonham-Carter, G.F., Jefferson, C.W. 2006. Mineral Potential Analyzed and Mapped at Multiple scales—A Modified Fuzzy Logic Method Using Digital Geology. In: Harris, J.R. (Ed.), GIS for the Earth Sciences. Geological Association of Canada. 143-162.

Exelis Visual Information Solution. 2009. ENVI EX user's guide. Boulder, Colorado, USA. 275p.

Farooq, S., Govil, H. 2014. Mapping regolith and gossan for mineral exploration in the Eastern Kumaon Himalaya, India using hyperion data and object oriented image classification. Advances in Space Research. 53, 1676-1685.

Fatima, K., Muhammad, U.K.K., Kausar, A.B., Toqeer, M., Haider, N., Rehman, A.U. 2017. Mineral identification and mapping using ASTER satellite image. Journal of Applied Remote Sensing. 11(4). 046006. https://doi: 10.1117/1.JRS.11.046006

Feizi, F., Mansouri, E. 2013. Introducing the iron potential zones using remote sensing studies in South of Qom Province, Iran. Open Journal of Geology. 3, 278-286.

Fernández, A., García, S., Galar, M., Prati, R., Krawczyk, B., Herrera, F. 2018. Learning from Imbalanced Data Sets. Springer, Cham. 253-277. https://doi.org/10.1007/978-3-319-98074-4.

Freyssinet, P.H., Butt, C.R.M., Morris, R.C., Piantone, P. 2005. Ore-forming processes related to lateritic weathering. Economic geology. 100th Anniversary Volume, 681-722.

Freyssinet, Ph., Zeegers, H., Tardy, Y. 1989. Morphology and geochemistry of gold grains in lateritic profiles from South Mali. J. Geochem. Explor. 32, 99–116.

Fuck, R.A., Dantas, E.L., Pimentel, M.M., Botelho, N.F., Armstrong, R., Laux, J.H., Junges, S.L., Soares, J.E., Praxedes, I.F. 2014. Paleoproterozoic crust-formation and reworking events in the Tocantins Province, central Brazil: A contribution for Atlantica supercontinent reconstruction. Precambrian Research. 244, 53-74.

Fuck, R.A., Dantas, E.L., Pimentel, M.M., Junges, S.L., Moraes, R. 2001. Nd isotopes, U–Pb single grain and SHRIMP zircon ages from basement rocks of the Tocantins Province. In: III South American Symposium on Isotope Geology, 2001, Pucon. Proceedings, Extended Abstract Volume (CD ROM), Santiago: Servicio Nacional de Geologia y Mineria 1, 141–144.

Fuck, R.A., Pimentel, M.M., Alvarenga, C.J.S., Dantas, E.L. 2017. The Northern Brasília Belt. In: Heilbron, M., Cordani, U.G., Alkmim, F.F. (Org.). São Francisco Craton, Eastern Brazil. Zurich: Springer. 205-220.

Goetz, A.F.H., Rowan, L.C. 1981. Geologic Remote Sensing. Science. 211, 781-791.

Grimaud, J.L., Chardon, D., Metelka, V., Beauvais, A., Bamba, O. 2015. Neogene cratonic erosion fluxes and landform evolution processes from regional regolith mapping (Burkina Faso, West Africa). Geomorphology. 241, 315-330.

Grove, C.I., Hook, S.J., Paylor, E.D. 1995. Laboratory reflectance spectra of 166 minerals 0.4 to 2.5 micrometer. Jet Propulsion Laboratory (JPL) Publ., Pasadena, CA: California Institute of Technology. 92–2.

Guerschman, J. P., Scarth, P. F., McVicar, T. R., Renzullo, L. J., Malthus, T. J., Stewart, J. B., Trevithick, R. 2015. Assessing the effects of site heterogeneity and soil properties when unmixing photosynthetic vegetation, non-photosynthetic vegetation and bare soil fractions from Landsat and MODIS data. Remote Sensing of Environment, 161, 12–26. https://doi.org/10.1016/j.rse.2015. 01.021.

Gupta, R.P., Tiwari, R.K., Saini, V., Srivastava, N., 2013. A Simplified Approach for Interpreting Principal Component Images. Adv. Remote Sens. 02, 111–119. https://doi.org/10.4236/ars.2013.22015.

Hamedianfar, A., Shafri, H.Z.M, Mansor, S., Ahmad, N. 2014. Improving detailed rule-based feature extraction of urban areas from WorldView-2 image and lidar data. Int. J. Remote Sens. 35(5), 1876–1899.

Hamedianfar, A., Shafri, H.Z.M. 2016. Integrated approach using data mining-based decision tree and object-based image analysis for high-resolution urban mapping of WorldView-2 satellite sensor data. J. Appl. Remote Sens. 10(2), 025001.

Hao, P., Shi, Q. 2003. Reversible integer KLT for progressive-to-lossless compression of multiple component images. IEEE Int. Conf. Image Process. 1, 633–636. https://doi.org/10.1109/icip.2003.1247041.

Herrera, I.L.I.E, Silva Filho, E.P., Iza, E.R.H.F., Horbe, A.M.C. 2016. Cartografia geológica e geomorfológica de crostas lateríticas na porção nordeste do estado de Rondônia. Revista Brasileira de Geomorfologia. 17, 177-190.

Holben, B., Justice, C. 1981. An examination of spectral band ratioing to reduce the topographic effect on remotely sensed data. Int. J. Remote Sens. 2(2), 115-133. https://doi.org/10.1080/01431168108948349.

Horbe, A.M., Costa, M. 1999. Geochemical evolution of a lateritic Sn–Zr–Th–Nb–Y–REE-bearing ore body derived from apogranite: the case of Pitinga, Amazonas – Brazil. J. Geochemical Explor. 66, 339–351. https://doi.org/10.1016/S0375-6742(99)00002-3.

Horbe, A.M.C.; Albuquerque M.F.S; Castro, R.T.; Peixoto, S.F. 2021. Advances in geochemical footprint, iron speciation, and Pb isotopes in the tropical regolith of north-northwestern Amazonia, Brazil. JOURNAL OF SOUTH AMERICAN EARTH SCIENCES, v. 106, p. 103096.

Huete, A.R. 1988. A soil-adjusted vegetation index (SAVI). Remote Sens. Environ. 25, 205–309. https://doi.org/10.1016/0034-4257(88)90106-X.

Huete, A.R., Jackson, R.D., Post, D.F., 1985. Spectral response of a plant canopy with different soil backgrounds 17, 37–53. https://doi.org/10.1016/0034-4257(85)90111-7.

Hunt, G.R, Ashley, R.P. 1979. Spectra of altered rocks in the visible and near infrared. Econ. Geol. 74, 1613–1629.

Hunt, G.R. 1979. Near-infrared (1.3-2.4 μm) spectra of alteration minerals — Potential for use in remote sensing. Geophysics. 44 (12), 1974-1986. https://doi.org/10.1190/1.1440951.

Hunt, G.R., Salisbury, J.W. 1970. Visible and near infrared spectra of minerals and rocks: I. Silicate minerals. Modern Geology, Amsterdam. 1, 283-300.

IAEA - International Atomic Energy Agency, 1991. Airborne gamma ray spectrometer surveying. Technical Reports Series nº 323. Viena.

Inzana, J., Kusky, T., Higgs, G., Tucker, R., 2003. Supervised classifications of Landsat TM band ratio images and Landsat TM band ratio image with radar for geological interpretations of central Madagascar. J. African Earth Sci. 37, 59–72. https://doi.org/10.1016/S0899-5362(03)00071-X.

Irons, J. R., Dwyer, J. L., Barsi, J. A. 2012. The next Landsat satellite: The Landsat data continuity mission. Remote Sensing of Environment, 122, 11-21. http://doi:10.1016/j.rse.2011.08.026.

Iza, E.R.H.F., Horbe, A.M.C, Silva, A.M. 2016. Boolean and fuzzy methods for identifying lateritic regoliths in the Brazilian Amazon using gamma-ray spectrometric and topographic data. Geoderma. 269, 27-38.

Iza, E.R.H.F., Horbe, A.M.C., Castro, C.C., Herrera, I.L.I.E. 2018. Integration of geochemical and geophysical data to characterize and map lateritic regolith: an example in the Brazilian Amazon. Geochemistry, Geophysics, Geosystems. 19(9), 3254-3271.

Jayawardhana, P.M., Sheard, S.N. 2000. The use of airborne gamma-ray spectrometry: a case study from the Mount Isa Inlier, northwest Queensland, Australia. Geophysics. 65(6), 1993–2000.

Jin, X., Paswanters, S., 2007. A fuzzy rule base system for object-based feature extraction and classification. A fuzzy rule base system for object-based feature extraction and classification. In: I. Kadar (ed). Signal processing, sensor fusion, and target recognition XVI. Proceedings of SPIE. vol. 6567, 65671H–665671H.

Johnson, R.A., Wichern, D.W. 2007. Applied multivariate statistical analysis. 6th ed. Upper Saddle River: Prentice Hall. 773p.

Jost, H., Chemale Jr. F., Dussin I.A., Martins R.A. 2010. U-Pb zircon Paleoproterozoic age for the metasedimentary host rocks and gold mineralization of the Crixás greenstone belt, Goiás, Central Brazil. Ore Geology Reviews. 37, 127-139.

Jost, H., Fortes, P.T.F.O. 2001. Gold deposits and occurrences of the Crixás Goldfield, central Brazil. Mineralium Deposita. 36(3-4), 358-376.

Kadhim, N., Mourshed, M., Bray, M. 2016. Advances in remote sensing applications for urban sustainability. Euro-Mediterr J Environ Integr. 1(7). DOI 10.1007/s41207-016-0007-4.

Kaufmann, H. 1988. Mineral exploration along the Aqaba—Levent structure by use of Landsat TM data; concepts, processing, and results. International Journal of Remote Sensing 9, 1639–1658.

Klir, G.J. 2004. Fuzzy logic: a specialized tutorial. In R. V. Demicco and G. J. Klir (Eds). Fuzzy logic in geology. San Diego, California. Elsevier Academic Press. 11–61.

Kotschoubey, B., Truckenbrodt, W., Heironimous, B. 1997. Bauxite Deposits of Paragominas. In: Carvalho, A., Boulangé, B.; Melfi, A.J. & Lucas, Y. (Organizadores). Brazilian Bauxites, USP/FAPESP/ORSTOM, Brazil. 75-116.

Kuyumjian, R.M., Cruz, E.L.C.C., Araújo Filho, J.O., Moura, M.A., Guimarães, E.M., Pereira, K.M.S. 2012. Geologia e ocorrências de ouro do Terreno Granito-Greenstone do Tocantins, TO: síntese do conhecimento e parâmetros para exploração mineral. Revista Brasileira de Geociências. 42, 213-228.

Landis, J.R., Koch, G.G. 1977. The measurement of observer agreement for categorical data. Biometrics. 33, 159-74.

Larizzatti, J.H., Oliveira, S.M.B., Butt, C.R.M. 2008. Morphology and composition of gold

in a lateritic profile, Fazenda Pison garimpo, Amazonas, Brasil. J. South Am. Earth Sci. 25, 359–376. https://doi.org/10.1016/j.jsames.2007.06.002.

Lima, C. V. 2002. Quantificação da taxa erosiva e estudo de perfis lateríticos da Bacia do Rio Jardim – Distrito Federal. Tese de Doutorado, IG-UnB.

Lobato, L.M., Ribeiro-Rodrigues, L.C., Vieira, F.W.R., 2001. Brazil's premier gold province. Part 11: Geology and genesis of gold deposits in the Archean rio das velhas greenstone belt, Quadrilátero ferrifero. Miner. Depos. 36, 249–277. https://doi.org/10.1007/s001260100180.

Loughlin, W.P., 1991. Principal Component Analysis for Alteration Mapping. Photogrammetric Engineering and Remote Sensing, 57, 1163-1169.

Martelet, G., Drufin, S., Tourliere, B., Saby, N.P.A., Perrin, J., Deparis, J., Prognon, F., Jolivet, C., Ratie, C., Arrouays, D. 2013. Regional regolith parameter prediction using the proxy of airborne gamma ray spectrometry. Vadose Zone J. 12(4). https://doi.org/10.2136/vzj2013.01.0003.

Martelet, G., Truffert, C., Tourliere, B., Ledru, P., Perrin, J. 2006. Classifying airborne radiometry data with Agglomerative Hierarchical Clustering: a tool for geological mapping in context of rainforest (French Guiana). Int. J. Appl. Earth Obs. Geoinf. 8, 208–223. https://doi.org/10.1016/j.jag.2005.09.003.

Martins, E. S. 1991. Comportamento mineralógico do ouro em perfis de intemperismo nas regiões de Luziânia – GO e Paracatu –MG. Dissertação de mestrado, IG-UnB. 187 p.

Martins, E. S. 2000. Petrografia, mineralogia e geomorfologia de regolitos lateríticos no Distrito Federal. Tese de Doutorado, IG-UnB. 181 p.

Martins-Ferreira, M.A.C, Campos, J.E.G, Pires, A.C.B. 2017. Near-mine exploration via soil geochemistry multivariate analysis at the Almas gold province, Central Brazil: A study case. Journal of Geochemical Exploration. 173, 52-63.

McBratney, A.B., De Gruitjer, J.J. 1992. A continuum approach to soil classification by modified fuzzy k-mean with extragrades. J. Soil Sci. 43, 159-175. https://doi.org/10.1111/j.1365-2389.1992.tb00127.x.

Meneses, P.R., Almeida, T., 2019. Reflectância das rochas. In: Reflectância dos materiais terrestres. Meneses, P.R., Almeida, T., Baptista, G.M.M.B. (org.), cap. 4. Oficina de textos, São Paulo. 119-162.

Metelka, V., Baratoux, L., Jessell, M.W., Barth, A., Jezek, J., Naba, S. 2018. Automated regolith landform mapping using airborne geophysics and remote sensing data, Burkina Faso, West Africa. Remote Sensing of Environment. 204, 964–978.

Minty, B.R.S. 1997. Fundamental of airborne gamma-ray spectrometry. AGSO J. Aust. Geol. Geophys. 17, 39–50.

Moojun, R., Shrestha, D.P., Jetten, V.G., van Ruitenbeek, F.J.A. 2017. Application of airborne gamma-ray imagery to assist soil survey: A case study from Thailand. Geoderma. 289, 196-212.

Mwaniki, M.W., Moeller, M.S., Schellmann, G. 2015. A comparison of Landsat 8 (OLI) and Landsat 7 (ETM+) in mapping geology and visualising lineaments: A case study of central region Kenya. The International Archives of the Photogrammetry, Remote Sensing and Spatial Information Sciences, Volume XL-7/W3, 36th International Symposium on Remote Sensing of Environment, Berlin, Germany. 897-903.

Nykänen, V., Groves, D.I., Ojala, V.J., Eilu, P., Gardoll, S.J. 2008. Reconnaissance-scale conceptual fuzzy-logic prospectivity modelling for iron oxide copper - Gold deposits in the northern Fennoscandian shield, Finland. Aust. J. Earth Sci. 55, 25–38. https://doi.org/10.1080/08120090701581372.

Okin, G.S., Clarke, K.D., Lewis, M.M. 2013. Comparison of methods for estimation of absolute vegetation and soil fraction cover using MODIS normalized BRDF-adjusted reflectance data. Remote Sensing of Environment, 130, 266-279. https://dx.doi.org/10.1016/j.rse.2012.11.021.

Oliveira, C.G., Oliveira F.B., Giustina M.E.S.D., Marques G.C., Dantas E., Pimentel M.M., Buhn B.M., 2015. The Chapada Cu–Au deposit, Mara Rosa magmatic arc, Central Brazil: Constraints on the metallogenesis of a Neoproterozoic large porphyry-type deposit. Ore Geology Reviews. 72, 1–21.

Oliveira, C.G., Pimentel, M.M., Melo, L.V., Fuck, R.A., 2004. The copper–gold and gold deposits of the Neoproterozoic Mara Rosa magmatic arc, central Brazil. Ore Geology Reviews. 25, 285–299. https://doi.org/10.1016/j.oregeorev.2004.04.006.

Oliveira, F.S., Varajão, A.F.D.C., Varajão, C.A.C., Boulangé, B., Costa, J.L.G., Vessani, L.A. 2009. Alteração supergênica e morfogênese tropical no complexo máfico-ultramáfico acamadado de Barro Alto, GO. Geociências. 28, 255-272.

Oliveira, F.S., Varajão, A.F.D.C., Varajão, C.A.C., Boulangé, B., Gomes, N.S. 2011. Bauxitisation of anorthosites from Central Brazil. Geoderma. 167-168, 319–327.

Oliveira, S.M., Trescases, J.J., Melfi, A.J. 1992. Lateritic nickel deposits of Brazil. Mineralium Deposita. 27, 137-146.

Oliveira, S.M.B., Campos, E.G. 1991. Gold-bearing iron duricrust in Central Brazil. J. Geochemical Explor. 41, 309–323. https://doi.org/10.1016/0375-6742(91)90005-F.

O'Reilly, G.A., Corey, M.C., Ford, K.L 1988. The role of airborne gamma-ray spectrometry in bedrock mapping and mineral exploration: case studies from granitic rocks within the Meguma Zone, Nova Scotia. Maritime Sediments and Atlantic Geology. 4, 47-60.

Ormeling, F.J. and Kraak, M.J. 2008. Maps as predictive tools – mind the gap. Cartographica. 43, 125–130.

Peixoto, S.F., Horbe, A.M.C. 2008. Bauxite in the northern of Amazonas. Revista Brasileira de Geociências. 38, 406-422.

Peixoto, S.F., Horbe, A.M.C., Soares, T.M., Freitas, C.A., Sousa, E.M.D. Iza, E.R.H.F. 2021. Boolean and fuzzy logic operators and multivariate linear regression applied to airborne gamma-ray spectrometry data for regolith mapping in granite-greenstone terrain in Midwest Brazil. Journal of South American Earth Sciences, 112. 103562.

Pimentel, M.M, Jost, H., Fuck, R.A. 2004. O Embasamento da Faixa Brasília e o Arco Magmático de Goiás. In: V. Mantesso Neto, A. Bartorelli, C.D.R. Carneiro, B.B. Brito Neves (Org.). Geologia do Continente Sul-Americano: Evolução da Obra de Fernando Flávio Marques de Almeida. Ed. Beca, São Paulo. 355–368.

Pimentel, M.M., Fuck, R.A., Botelho, N.F. 1999. Granites and the geodynamic history of the Neoproterozoic Brasília Belt, Central Brazil: a review. Lithos. 46(3), 463–483.

Pimentel, M.M., Fuck, R.A., Jost, H., Ferreira Filho C.F., Araújo, S.M., 2000. The basement of the Brasília Fold Belt and the Goiás Magmatic Arc. In: Cordani U.G., Milani, E.J., Thomaz Filho, A., Campos, D.A. (Eds.). Tectonic Evolution of South America. Rio de Janeiro: 31st IGC. 190–229.

Pires, A.C.B, Moraes, R.A.V. 2006. New processing technologies applied do airborne geophysical data: impact on interpretation. In: II Simpósio Brasileiro de Exploração Mineral, SIMEXMIN, Ouro Preto, MG - Brazil.

Pires, A.C.B. 1995. Identificação geofísica de áreas de alteração hidrotermal, Crixás-Guarinos, Goiás. Rev. Bras. Geoc. 25(1), 61–68. https://doi.org/10.25249/0375-

7536.19956168.

Porto, C.G., Hale, M., 1996. Mineralogy, morphology and chemistry of gold in the stone line lateritic profile of the Posse deposit, Central Brazil. J. Geochem. Explor. 57, 115–125. https://doi.org/10.1016/S0375-6742(96)00027-1.

Porwal, A., Deb Das, R., Chaudhary, B., Gonzalez-Alvarez, I., Kreuzer, O., 2015. Fuzzy inference systems for prospectivity modeling of mineral systems and a case-study for prospectivity mapping of surfcial Uranium in Yeelirrie Area, Western Australia. Ore Geol. Rev. 71, 839–852. https://doi.org/10.1016/j.oregeorev.2014.10.016.

Pour, A.B., Hashim, M. 2015. Hydrothermal alteration mapping from Landsat-8 data, Sar Cheshmeh copper mining district, south-eastern Islamic Republic of Iran. Journal of Taibah University for Science. 9, 155-166.

Pour, A.B., Park, Y., Park, T.S., Hong, J.K., Hashim, M., Woo, J., Ayoobi, I. 2018. Regional geology mapping using satellite-based remote sensing approach in Northern Victoria Land, Antarctica. 16, 23-46.

Prudnikova, E., Savin, I., Vondeker, G., Grubina, P., Shishkonakova, E., Sharychev, D., 2019. Influence of soil background on spectral reflectance of winter wheat crop canopy. Remote Sens. 11, 1932. Doi:10.3390/rs11161932.

Raines, G.L, Sawatzky, D.L., Bonham-Carter, G.F. 2010. New fuzzy logic tools in ArcGis 10: ArcUser, ESRI, 13pp.

Ricchetti, E., 2000. Multispectral satellite image and ancillary data integration for geological classification. Photogrammetric Engineering & Remote Sensing. 66(4), 429-435.

Rockwell, B.W., 2013. Automated mapping of mineral groups and green vegetation from Landsat Thematic Mapper Imagery with an example from the San Juan Mountains, Colorado. U.S. Geol. Surv. Sci. Investig. Map 3252 25. https://doi.org/https://doi.org/10.3133/sim3252

Roy, D. P., Wulder, M.A., Loveland, T.A., Woodcock, C.E., Allen, R.G., Anderson, M.C., et al., 2014. Landsat-8: Science and product vision for terrestrial global change research. Remote Sensing of Environment 145, 154-172. https://doi.org/10.1016/j.rse.2014.02.001.

Sabins, F.F. 1997. Remote Sensing — Principles and Interpretation, 3rd ed., W.H. Freeman, New York, NY., 494 p.

Sabóia, A.M., Meneguini, P.F.V.B., Gonçalves, G.F., Lacerda Filho, J.V. 2015. Carta Geológica Folha Dianópolis SC.23-Y-C – 1:250.000 – TO. CPRM.

Santosh, M., Omana, P.K., Yoshida, M. 1990. Gold grains in laterite weathering profiles of Nilambur, South India and a model for the genesis of supergene gold deposits. Journal of Mineralogy Petrography and Economic Geology. 85, 416–423.

SEPLAN - Secretaria do Planejamento e da Modernização Pública 2012. Atlas do Tocantins: Subsídios ao Planejamento da Gestão Territorial, Superintendência de Pesquisa e Zoneamento Ecológico-Econômico, Diretoria de Zoneamento Ecológico-Econômico – DZE, Palmas.

SEPLAN - Secretaria do Planejamento e Meio Ambiente. 1999. Atlas do Tocantins: subsídios ao planejamento da gestão territorial. Diretoria de Zoneamento Ecológico Econômico. Palmas. 49 p.

Sherman, D.M., Waite, T.D. 1985. Eletronic spectra of Fe^{3+} oxides and oxide hidroxides in the near IR and near UV. American Mineralogist. 70(11-12), 1262-1269.

Silva, A.M., Pires, A.C.B., MacCafferty, A., Moraes, R.A.V. de, Xia, H. 2003. Application of airborne geophysical data to mineral exploration in the uneven exposed terrains of the Rio das Velhas Greenstone Belt. Rev. Bras. Geoc., 33(2-Suplemento), 17-28.

Silvero, N.E.Q., Di Raimo, L.A.D.L., Pereira, G.S., de Magalhães, L.P., da Silva Terra, F., Dassan, M.A.A., Salazar, D.F.U., Demattê, J.A.M. 2020. Effects of water, organic matter, and iron forms in mid-IR spectra of soils: Assessments from laboratory to satellite-simulated data. Geoderma 375, 114480.

Singh, A., Harrison, A. 1985. Standardized principal components. Int. J. Remote Sens. 6, 883–896. https://doi.org/10.1080/01431168508948511.

Siqueira, G.S., Veloso, G.V., Fernandes-Filho, E.I., Francelino, M.R., Schaefer, C.E.G.R., Corrêa, G.R. 2021.Evaluation of machine learning algorithms to classify and map landforms in Antarctica. Earth Surf. Process. Landforms. 1-16. https://doi.org//10.1002/esp.5253

Smith, R.E, Anand, R.R., Alley, N.F. 2000. Use and implications of paleoweathering surfaces in mineral exploration in Australia. Ore Geology Reviews 16, 185–204. https://doi.org/10.1016/S0169-1368(99)00030-X.

Souza, M.V., Horbe, A.M.C., Silva, B.C., Peixoto, S.F., Castro, R.T. 2021. Regolith LANDSAT-8/OLI and Hyperion/EO-1 images classification in Midwest of Brazil.

Journal of South American Earth Sciences. 111, 103460. https://doi.org/10.1016/j.jsames.2021.103460.

Storey, J., Choate, M., Lee, K., 2008. Geometric performance comparison between the OLI and ETM+. In: Proceedings of PECORA 17 Conference — The Future of Land Imaging Going Operational, Denver, CO, USA.

Takodjou Wambo, J.D., Pour, A.B., Ganno, S., Asimow, P.D., Zoheir, B., Salles, R. dos R., Nzenti, J.P., Pradhan, B., Muslim, A.M. 2020. Identifying high potential zones of gold mineralization in a sub-tropical region using Landsat-8 and ASTER remote sensing data: A case study of the Ngoura-Colomines goldfield, eastern Cameroon. Ore Geol. Rev. 122, 103530. https://doi.org/10.1016/j.oregeorev.2020.103530

Tangestani, M.H., Moore, F. 2000. Iron oxide and hydroxyl enhancement using the Crósta Method: a case study from the Zagros Belt, Fars Province, Iran. Int. J. Appl. Earth Obs. Geoinf. 2, 140–146.

Tardy, Y. 1992. Diversity and terminology of lateritic profiles. In: Weathering, Soils and Paleosols. Edited by I.P. Martini and W. Chesworth. Developments in Earth Surface Processes. Elsevier, Amsterdam. 379-401.

Tardy, Y. 1993. Petrologie des Latérites et des Sols Tropicaux. Masson, Paris, 460p.

Tardy, Y. Roquin, C. 1998. Derive des continents, Paléoclimats et altérations tropicales. Èditions BRGM. Orléans. 473 p.

Tematio, P., Songmene, S.M., Leumbe, O.L., Nouazi, M.M., Yemefack, M., Fouateu, R.Y. 2015. Mapping bauxite indices using Landsat ETM+ imageries constrained with environmental factors in Foumban area (West Cameroon). J. African Earth Sci. 109, 47-54. https://doi.org/10.1016/jafrearsci.2015.05.010.

Thurmond, A.K., Abdelsalam, M.G., Thurmond, J.B. 2006. Optical-radar-DEM remote sensing data integration for geological mapping in the Afar Depression, Ethiopia. J. African Earth Sci. 44, 119-134. https://doi.org/10.1016/j.afrearsci.2005.10.006.

Tomlin, C.D. 1994. Map algebra: one perspective. Landscape and Urban Planning. 30, 3-12.

Traore, M., Takodjou Wambo, J.D., Ndepete, C. P., Tekine, S., Pour, A.B., Muslim, A.M. 2020. Lithological and alteration mineral mapping for alluvial gold exploration in the south east of Birao area, Central African Republic using Landsat-8 Operational Land Imager (OLI) data. Journal of African Earth Sciences. 170. 10.1016/j.jafrearsci.2020.103933.

Treitz, P., Rogan, J. 2004. Remote sensing for mapping and monitoring land-cover and land-use change—an introduction. Progress in Planning. 61, 269–279.

Trescases, J.J. 1992. Chemical weathering. In: Butt C. R. M. & Zeegers H. eds. Regolith Exploration Geochemistry in Tropical and Subtropical Terrains. Handbook of Exploration Geochemistry 4. Elsevier, Amsterdam. 25–39.

Valeriano, C.M., Pimentel, M.M., Heilbron, M., Almeida, J.C.H., Trouw, R. 2008. Tectonic evolution of the Brasília Belt, Central Brazil, and early assembly of Gondwana. Geological Society of London Special Publication. 294, 197–210.

Van der Werff, H.M.A., van der Meer, F.D. 2016. Sentinel-2A MSI and Landsat 8 OLI provide data continuity for geological remote sensing. Remote Sensing. 8, 883. https://doi.org/10.3390/rs8110883.

Vicente, L.E., Souza Filho, C.R. de. 2011. Identification of Mineral Components in Tropical Soils Using Reflectance Spectroscopy and Advanced Spaceborne Thermal Emission and Reflection Radiometer (ASTER) Data. Remote Sensing of Environment. 115, 1824–1836.

Viera, A.J., Garrett, J.M. 2005. Understanding interobserver agreement: the kappa statistic. Family Medicine. 37 (5), 360-363.

Voll, E., Silva, A.M., Pedrosa-Soares, A.C. 2020. Tracking iron-rich rocks beneath Cenozoic tablelands: An integration of geological, airborne geophysical and remote sensing data from northern Minas Gerais State, SE Brazil. J. South Am. Earth Sci. 101, 102604. https://doi.org/10.1016/j.jsames.2020.102604.

Watson, K., Fitterman, D., Saltus, R.W., McCafferty, A., Swayze, G., Church, S., Smith, K., Goldhaber, M., Robson, S., McMahon, P. 2001. Application of geophysical techniques to minerals-related environmental problems. U.S. Geological Survey. Open-File Report 01-458. 46 p.

White, K., Walden, J., Drake, N., Eckardt, F., Settle, J. 1997. Mapping the iron oxide content of dune sands, Namib Sand Sea, Namibia, using Landsat Thematic Mapper data. Remote Sensing of Environment, 62, 30-39.

Wilford, J., Minty, B. 2007. The use of airborne gamma-ray imagery for mapping soils and understanding landscape processes. In: Developments in Soil Science – Volume 31: Digital Soil Mapping – An Introductory Perspectve. Edited by P. Lagacherie, A.B. McBratney and M. Voltz. Elsevier.

Wilford, J.R. 1992. Regolith mapping using integrated Landsat TM imagery and high-resolution gamma-ray spectrometric imagery – Cape York Peninsula. Bureau of Mineral Resources Record 1992/78: 35 pp.

Wilford, J.R. 2012. A weathering intensity index for the Australian continent using airborne gamma-ray spectrometry and digital terrain analysis. Geoderma. 183–184, 124–142.

Wilford, J.R. 1995. Airborne gamma-ray spectrometry as a tool for assessing relative landscape activity and weathering development of regolith, including soils. Australian Geological Survey Organisation Research Newsletter. 22, 12–14.

Wilford, J.R., Bierwirth, P.N., Craig, M.A. 1997. Application of airborne gamma-ray spectrometry in soil/regolith mapping and applied geomorphology. AGSO Journal of Australian Geology and Geophysics 17 (2), 201–216.

WRB, 2015. World reference base for soil resources 2014, update 2015. International soil classification system for naming soils and creating legends for soil maps. World Soil Resources Reports No. 106. FAO, Rome.

Yang, Y., Liu S., Jin Z. 2009. Laterization and its control to gold occurrence in Laowanchang gold deposit, Guizhou Province, Southwest of China. J. Geochem. Explor. 100, 67–74. http://doi.org/10.1016/j.gexplo.2008.04.004

Zadeh, L.A., 1965. Fuzzy Sets. Information and Control. 8(3), 338–353.

Zimmermann, H.J. 1985. Fuzzy Set Theory and Its Applications. Kluwer Academic, Dordrecht.